FOSSIL ENERGY

DOE/BC/14851-1
(OSTI ID: 6738)

PREDICTION OF GAS INJECTION PERFORMANCE FOR HETEROGENEOUS RESERVOIRS

Annual Report
September 1997 – September 1998

By
Martin J. Blunt
Franklin M. Orr, Jr.

Date Published: May 1999

Work Performed Under Contract No. DE-FG22-96BC14851

Stanford University
Stanford, California

National Petroleum Technology Office
U. S. DEPARTMENT OF ENERGY
Tulsa, Oklahoma

DOE/BC/14851-1
Distribution Category UC-122

Prediction of Gas Injection Performance for Heterogeneous Reservoirs

By
Martin J. Blunt
Franklin M. Orr, Jr.

May 1999

Work Performed Under Contract DE-FG22-96BC14851

Prepared for
U.S. Department of Energy
Assistant Secretary for Fossil Energy

Purna Halder, Project Manager
National Petroleum Technology Office
P.O. Box 3628
Tulsa, OK 74101

Prepared by
Stanford University
Petroleum Engineering Department
651 Serra Street, Room 260
Stanford, CA 94305-2220

DISCLAIMER

Portions of this document may be illegible in electronic image products. Images are produced from the best available original document.

Contents

List of Tables v

List of Figures vii

Acknowledgements xi

1. Introduction 1

2. Measurement of Three Phase Relative Permeability during Gravity Drainage using CT Scanning 3

2.1 Introduction 3
2.1.1 Gravity Drainage Experiments 4
2.1.2 Calculating Three Phase Relative Permeability 4
2.2 Our Approach to the Three Phase Flow Problem 5
2.2.1 Three Phase Gravity Drainage 5
2.2.2 Analysis of Gravity Drainage Experiments 5
2.3 Dual Energy CT scanning and Experimental Design 8
2.3.1 Experimental Procedure 9
2.3.2 Analog Experiments 10
2.3.3 Measuring the Spreading Coefficient 11
2.3.4 In-situ Saturation Measurements from Scanned Images 12
2.4 Three Phase Gravity Drainage Experiments 15
2.5 Results and Discussions 15
2.6 Summary and Conclusions 17
2.7 Nomenclature 17
2.8 Appendix A 20
2.8.1 Three Phase Saturation Calculation 20
2.8.2 Calculating Porosity 21
2.8.3 Error Analysis 21

3. The Effect of Wettability on Three-Phase Relative Permeability 23

3.1 Introduction 23
3.2 Materials and Methods 24
3.2.1 Oil and Water Relative Permeabilities 25
3.2.2 Gas Permeability 26
3.3 Results 27
3.4 Pore Scale Explanation 31
3.5 Discussion 35
3.6 Conclusions 36
3.7 Nomenclature 36

4. Calculation of Minimum Miscibility Pressure **39**
4.1 Abstract 39
4.2 Introduction 39
4.3 Mathematical Approach 41
4.4 Examples of MMP Calculations 43
4.4.1 Four-component System: $CH_4/CO_2/C_4/C_{10}$ 43
4.4.2 Crude Oil Systems 45
4.5 Discussion 46
4.6 Conclusions 47
4.7 Nomenclature 47
4.8 Appendix 47
4.9 SI Metric Conversion Factors 48

5. A Streamline-Based 3D Field-Scale Compositional Reservoir Simulator **59**
5.1 Introduction 59
5.2 Compositional Displacements 61
5.3 The Streamline Formation 62
5.4 One-Dimensional Compositional Solver 63
5.5 Two-Dimensional Solutions 64
5.5.1 Three Component Condensing Gas Drive 65
5.5.2 Four Component Condensing-Vaporizing Gas Drive 66
5.5.3 Sensitivity on Injected Composition 67
5.6 Three Dimensional Solution 68
5.7 Timing and Scaling 68
5.8 Conclusions 69
5.9 Nomenclature 70

References **79**

List of Tables

2.1 Three Phase Gravity Drainage Experiments. S_{oi} is the initial oil saturation averaged over the whole core. S_{of} is the final oil saturation at the end of the experiment averaged over the top half of the column (top 45 cm). S_{wf} is the final average water saturation in the top half of the column. The * indicates waterflood residual oil (S_{or}).....6
2.2 Fluid Properties 9
2.3 Interfacial tensions and spreading coefficient 12

3.1 Interfacial tensions 24
3.2 Experiments.....27

List of Figures

2.1 Calibration and porosity measurements from the CT Scanner 8
2.2 Results of sieve analysis for the sand used in this study 9
2.3 In-situ saturation measurements at different locations along the length of the core after 2.50 hours of drainage 12
2.4 Water and air saturation profiles as a function of time and distance along the length of the core 13
2.5 Water relative permeability as a function of water saturation. The straight line is a best fit through the data on the doubly logarithmic axes 13
2.6 Saturation path and oil saturation profile for experiment 1 14
2.7 Water and air saturation profiles as a function of time and distance for experiment 1 14
2.8 Water relative permeability as a function of water saturation. The straight line in the top figure is a best fit through the data. Notice that the results of the three experiments lie on a single curve, which is similar to the two phase results in Fig. 2.5 16
2.9 Measured oil relative permeabilities. The straight lines are best fits to the data at low oil saturation. Notice that all the curves show an approximately quadratic form for the oil relative permeability at low oil saturations, except for the non-spreading decane system 18
2.10 Oil relative permeability for Naylor *et. al.*[25] 19
2.11 Oil relative permeability from Grader and O'Meara[28] 19
2.12 Fluid distribution in the corner of a pore space 19

3.1 Oil and water saturation profiles versus time during gravity drainage. The sand was water-wet and the initial condition was connate water saturation S_{wc}. Oil and water permeabilities can be calculated directly from the measured distributions 26
3.2 Measured oil and water relative permeabilities with n-octane as the oil for water-wet ($f = 0$), fractionally-wet ($f = 0.5$), and oil-wet ($f = 1$) sand during three-phase gravity drainage. Open symbols are drainages which started from residual oil saturation (S_{or}), and closed symbols are drainages which started from connate water saturation (S_{wc}). The solid lines are fits to the data at high saturations 28
3.3 Measured oil and water relative permeabilities with hexane, octane, and decane as the oil in water-wet ($f = 0$) sand and with octane in water-wet sandstone during three-phase gravity drainage 29
3.4 Measured water relative permeabilities for a) the two-phase (gas/water) system and for b) the three-phase (gas/oil/water) system from gravity drainages in water-wet ($f = 0$) sand 30
3.5 Measured gas relative permeabilities for a) the two-phase gas/water system for media of varying wettability ($f = 0$, 0.5, 1) and the two-phase gas/oil system for oil-wet media ($f = 1$), and for b) the three-phase gas/oil/water system for water-wet ($f = 0$) and oil-wet ($f = 1$) media. The gas relative permeability in oil-wet sand is roughly a factor of two smaller than that for identical water-wet sand when water is the other phase 31
3.6 Configuration of fluids on: a) a flat water-wet surface, b) a flat oil-wet surface 33

3.7 Possible configuration of fluids in a pore space corner of half-angle ß: a) water-wet surfaces, b) oil-wet surfaces. Note that configuration b) is not allowed as $\theta_{gw} > 90°$ 33
3.8 Comparision of relative permeabilities. a) A spreading system ($\theta_{go} \approx 0$) : Octane in water-wet sand. b) A non-spreading system : Decane in water-wet sand. c) A non-wetting system: Water in oil-wet sand 34

4.1 Key tie lines intersect each other for a displacement of oil *o* by gas *g* 51
4.2 Comparison of MMPs calculated by forward contacts in a single mixing cell and by the tie line intersection method 51
4.3 Composition paths and crossover tie line surface for the displacement of oil *O* (40% CH_4, 5% CO_2, 20% C_4 and 35% C_{10}) by I_1 to I_4 at 1600 psia and 160F 52
4.4 Compositional simulation results for the displacement of 40% CH_4, 5% CO_2, 20% C_4 and 35% C_{10} by 50% CO_2 and 50% CH_4 at 160F. The calculated MMP is 2500 psia 52
4.5 Convergence of reverse contacts to the injection gas tie line and forward contacts to the initial oil tie line (symbols indicate the phase compositions obtained by a negative flash) 53
4.6 Tie lie lengths for rich gas displacement of an eight-component oil (Hearn and Whitson [78]) at 212F. The calculated MMP is 3279 psia 53
4.7 Tie line lengths for lean gas displacement of an eight-component oil (Hearn and Whitson [78]) at 212F. The calculated MMP is 5582 psia 54
4.8 Tie line lengths for rich gas displacement of a 15-component oil (Hearn and Whitson [78]) at 212F. The calculated MMP is 3115 psia 54
4.9 Tie line lengths for lean gas displacement of a 15-component oil (Hearn and Whitson [78]) at 212F. The calculated MMP is 5253 psia 55
4.10 Tie line lengths for displacement of oil A (Zick [67]) by solvent A 185F. The calculated MMP is 2169 psia 55
4.11 Tie line lengths for displacement of oil A (Zick [67]) by 20% CH_4 and 80% solvent A at 185F. The calculated MMP is 3013 psia 56
4.12 Tie line lengths for displacement of oil A (Zick [67]) by 23% CH_4 and 77% solvent A at 185F. The calculated MMP is 3283 psia 56
4.13 Comparison between analytically calculated MMPs with slim tube test results 57

5.1 One-dimensional, TVD solutions at $t_D = 0.5$ with 100 grid blocks using UTCOMP (v.3.2 w / automatic time stepping) and the 1D compositional simulator (CFL=0.5) used in this work for pure CO_2 injection into a 30/70 mixture of CH_4 and C_{10} at 1600 psia and 160° F 64
5.2 One-dimensional mobility ratio profile for the three component condensing problem of Fig. 5.1 at $t_D = 0.5$ 65
5.3 Permeability field (62 x 25) and spatial distribution of CO_2 3DSL and UTCOMP at $t_D = 0.5$ 71
5.4 Cumulative recoveries of CH_4 plus C_{10} for 3DSL and UTCOMP 72
5.5 Spatial distribution of CO_2 for 3DSL at $t_D = 0.5$ for grids 124 x 50 and 248 x 100 compare to the UTCOMP solution for grid 124 x 50 73

5.6 One-dimensional, TVD solution with 100 gridblocks using UTCOMP (v.3.2 w / automatic time stepping) and TVD solutions with 100 and 500 gridblocks using 3DSL (CFL=0.25) for CH_4/C_3 (65/35) injection into a 20/40/40 mixture of $CH_4/C_6/C_{16}$ at 2000 psia and 160^{circ}F 74
5.7 Saturations maps at $t_D = 0.4$ for the displacement of a 20/40/40 mixture of $CH_4/C_6/C_{16}$ at 2000 psia and 160°F by a 65/35 mixture of CH_4/C_3 through a heterogeneous cross-section with 125 x 50 gridblocks 75
5.8 Sensitivity of the displacement of a 20/40/40 mixture of $CH_4/C_6/C_{16}$ at 2000 psia and 160^{circ}F on the enrichment level of the injected mixture of CH_4/C_3. The permeability field has 5 orders of magnitude difference in permeability. The maps show spatial distribution of C_3. Recoveries are C_6 plus C_{16} 76
5.9 3D solutions with 180 x 180 x 16 = 518,400 gridblocks and with 60 x 60 x 8 = 28,800 gridblocks for the 4C problem of Fig. 5.6 77
5.10 Scaling of compositional solution 78

Acknowledgements

We would like to thank the many students, post-docs and research associates who contributed to this work. David DiCarlo is the research associate in charge of our experimental program. He has been with us just over a year now and has already made important contributions to our work. Chapter 3, on the effects of wettability on three-phase relative permeabilities, describes his recent research. He was also responsible for preparing this report. Akshay Sahni, whose work is described in Chapter 2 received his PhD earlier this year and is now working for Chevron in La Habra, California. The work in Chapter 4, on the calculation of mininum miscibility pressure, was performed by Yun Wang, who received his PhD in July this year and is now with Arco in Texas. Acting Assistant Professor Marco Thiele and post-doc Rod Batycky collaborated on the streamline work in chapter 5 and are now working for their own start-up company, StreamSim Technologies, developing further the ideas desribed in this report in a commercial domain.

Our present group also includes research associate Charles Schaefer, post-doc Yann Gautier, PhD students Richard Hughes and Jichun Zhu, and MS students Rajiv Lulla, Mun Hong Hui, Stephanie Bertels and Mathieu Prevost. Their research will be described in later reports.

We would also like to thank Yolanda Williams who performs an excellent job of running the adminstration of our research group and making sure that our reports are on time!

We gratefully acknowledge the support of the Department of Energy under Grant No. DE-FG22-96BC14851. We thank Jerry Casteel and his colleagues for their continued interest and encouragement. We also are grateful for funding from the ten members of the SUPRI-C Gas Injection Affiliates Group: Arco, British Petroleum Exploration, Chevron, Elf, Exxon, Japan National Oil Corporation, Mobil, Norsk Hydro, Saga Petroleum, and Statoil. Without this generous support this work would not have been possible.

Martin Blunt
Lynn Orr
Stanford
October 1998

1. Introduction

This report describes research carried out in the Department of Petroleum Engineering at Stanford University from September 1997 - September 1998 under the second year of a three-year grant from the Department of Energy on the "Prediction of Gas Injection Performance for Heterogeneous Reservoirs." The research effort is an integrated study of the factors affecting gas injection, from the pore scale to the field scale, and involves theoretical analysis, laboratory experiments and numerical simulation. The original proposal described research in four main areas: (1) Pore scale modeling of three phase flow in porous media; (2) Laboratory experiments and analysis of factors influencing gas injection performance at the core scale with an emphasis on the fundamentals of three phase flow; (3) Benchmark simulations of gas injection at the field scale; (4) Development of streamline-based reservoir simulator. Each stage of the research is planned to provide input and insight into the next stage, such that at the end we should have an integrated understanding of the key factors affecting field scale displacements. The chapters that follow give a detailed account of our progress in these areas.

Chapters 2 and 3 describe our work using CT scanning to measure three phase relative permeabilities. This work represents a significant fraction of the research proposed in the original grant and almost completes our experimental program. Chapter 2 provides a detailed description of the method we use to find three phase relative permeabilities. The CT scanner is used to image the saturation distribution as a function of distance and time along a core during a gravity drainage displacement. From this the relative peremabilities may be found by direct application of Darcy's law and the conservation of mass, with no end effects or experimental artifacts. Relative permeabilities are measured that span more than six orders of magnitude, down to oil saturations as low as $S_o = 0.01$. An extensive study is performed on sand-packs and a Berea sandstone to study gravity drainage in water-wet media. The effects of initial oil saturation and the oil spreading coefficient are discussed. The results of the experiments are explained and interpreted in terms of the arrangement of fluids at the pore scale.

In Chapter 3 the experimental work is extended to study the effect of wettability in three phase flow. Sand-packs with different fractions of oil-wet and water-wet grains were mixed together. Furthermore, analogue experiments are described from which the gas relative permeability is measured. Thus a comprehensive set of three phase data as a function of intial oil saturation, oil spreading coeffcient and wettabilty is obtained. All the generic features of the results can be explained in terms of fluid flow at the pore scale, thus providing a link with the pore level modeling effort that was described in the previous Annual Report. This work almost concludes our experimental effort. Next year, we will study three phase flow in mixed-wet sand-packs, using a more physically-based scenario for wettability changes.

Chapter 4 describes the culmination of 10 years of DOE sponsored research on the phase behavior of oil and gas mixtures and the estimation of minimum miscibility pressure (MMP) for gas injection projects. A semi-analytical technique is described to compute the MMP for gas injection, where the gas and oil contain arbitrary numbers of chemical components. The theory is based on method-of-characteristics solutions to the one-dimensional flow equations, coupled with the phase behavior. Injection, initial and cross-over tie-lines are constructed for a general n component system, and the tie-line that controls miscibility is identified. A general and accurate method for obtaining the MMP is thus developed and the predictions of the theory compare favorably with experimental measurements and are shown to be superior in terms of speed and accuracy to other numerical methods in the literature that use direct compositional simulation or mixing cells.

Chapter 5 represents a high point in our research effort on streamline-based simulation. The

methodology for using streamlines as an attractive alternative to conventional grid-based methods is extended to study compositional displacements. A general, compositional model is solved in one dimension along each streamline, accounting for phase behavior and volume change on mixing. The method is shown to be much faster (around 100 times or more for large problems) and more accurate than conventional simulation. The streamline method is particularly well suited to study complex gas injection projects in highly heterogeneous media, where the combination of well placement, geological variability and phase behavior poses a particular challenge to finite-difference and finite-element codes. Next year, further improvements of the streamline method for very large models using a nested grid approach are planned.

2. Measurement of Three Phase Relative Permeability during Gravity Drainage using CT Scanning

Akshay Sahni, Jon Burger, and Martin Blunt

We measured three phase relative permeabilities for gravity drainage using a dual-energy medical CT scanner modified to scan vertical cores. Independent measurements of two saturations as a function of time and distance along the length of the core were made from which relative permeabilities were found. Three phase (air/oil/water) gravity drainage experiments were performed on systems with different spreading coefficients and at different initial conditions. Experiments were run on both consolidated and unconsolidated porous media. The results were compared to measurements of three phase flow in capillary tubes, micromodels and to predictions from network modeling.

We find that at low oil saturation $k_{ro} \sim S_o^2$ for hexane and octane as the oil phase. This functional form of relative permeability is consistent with the drainage of oil layers, wedged between the water and gas in crevices of the pore space. For decane, which is non-spreading, the layer drainage regime was not observed. At higher oil saturations $k_{ro} \sim S_o^a$ with $a \approx 4$ for spreading and non-spreading systems. Within the scatter of the experimental data, oil and water relative permeability are functions only of their own saturations and independent of initial conditions.

2.1 Introduction

The simultaneous flow of three immiscible fluids in porous media is an essential component of enhanced oil recovery and aquifer remediation processes. Three phase flow may occur during solution gas drive, gas injection, surfactant flooding and thermal recovery. High oil recoveries have been observed during three phase gravity drainage when gas displaces oil downdip in the presence of water.[1, 2, 3, 4, 5] Three phase gravity drainage is of importance in many oilfields under tertiary recovery, such as Prudhoe Bay.[6, 7]

Three phase gravity drainage is also an important process in the environmental industry. Leakage of non-aqueous phase liquid (NAPL) is a major source of groundwater contamination. The displacement of NAPL in the presence of air and water is similar to the process of gravity drainage in oil reservoirs. For designing efficient subsurface cleanup processes it is essential to determine the amount of trapped NAPL and the rate at which the NAPL migrates downwards to the water table.

In recent years, experiments in micromodels[8, 9, 10, 11, 12] and capillary tubes[13, 14] have demonstrated typical three phase configurations at the pore scale, together with pore-level displacement processes and representative flow rates for oil and water in a single pore. Using this knowledge of the behavior at the pore scale, several three phase network models have been developed which have computed three phase relative permeabilities and oil recoveries.[15, 16, 17, 18, 19, 20, 21, 22]

While research at the pore scale provides a good conceptual picture of several three phase flow phenomena, carefully characterized experiments at the core scale are necessary to validate the macroscopic predictions of pore level models, and to provide a basis for predicting and interpreting three phase flow at the field scale.

[1]The material in this chapter was presented at the 1998 SPE/DOE Improved Oil Recovery Symposium in Tulsa, Oklahoma, April 19-22, 1998, and is published as SPE paper 39655 in the conference proceedings.

The following sections discuss some of the published three phase experiments and relative permeability estimation techniques. Then we give an outline of our experimental approach.

2.1.1 Gravity Drainage Experiments

Vizika and Lombard[23] studied the effects of wettability and spreading characteristics of the fluid system in three phase gravity drainage. The highest oil recoveries were obtained for spreading systems and water-wet or fractionally-wet conditions. Slow oil production after gas breakthrough was observed for spreading systems, which resulted, eventually, in low oil saturations. For non-spreading systems, oil recoveries were lower. The lowest oil recoveries were obtained in oil-wet porous media as the oil was subject to strong capillary retention. The relative permeabilities for the experiments were obtained numerically by history matching the oil production data. In water-wet and in fractionally-wet porous media the oil relative permeability was higher for spreading systems than for non-spreading systems.

Skurdal *et. al* [24] analyzed gravity drainage experiments using spreading and non-spreading systems under oil-wet, water-wet and mixed-wet conditions. The final oil saturations obtained from all the experiments varied from 3% to 8%. The results did not allow firm conclusions to be drawn regarding the effect of spreading characteristics on oil recovery. For the experiments conducted the impact of wettability on oil recovery was small.

Naylor *et. al* [25] performed gravity drainage experiments by measuring in-situ oil and brine saturations using a radioactive tracer technique. Analysis showed that the oil relative permeability was a function only of the oil saturation and had a zero asymptotic residual oil saturation. The experiments were conducted on a consolidated Clashach sandstone with a spreading oil.

Skauge *et. al*[26] summarized results from gas gravity drainage experiments at different water saturations for oil having a spreading coefficient of zero. In-situ measurements of saturation were obtained using a nuclear tracer technique. It was observed that increasing the water saturation changed the oil recovery by gravity drainage under water-wet conditions. The oil recovery was higher with connate water present than without, with the maximum recovery being at an initial water saturation of 30% .

2.1.2 Calculating Three Phase Relative Permeability

Virnovsky[27] and Grader and O'Meara[28] developed a theory to obtain three phase relative permeability by an extension of the Welge[29] and JBN[30] methods to three phases. Siddiqui *et. al*[31] verified the theory using X-ray computerized tomography to obtain in-situ saturations for three phase dynamic displacement experiments. Sarem[32] obtained three phase relative permeability by unsteady state displacement experiments assuming that relative permeability of each phase was a function of its own saturation. Oak *et. al*[33] presented a steady-state study of three phase relative permeability using fired Berea cores. Naylor *et. al*[25] obtained three phase relative permeability from gravity drainage experiments using in-situ saturation measurements and ignoring capillary pressure. Nordvedt *et. al*[34] performed displacement experiments on low-permeability chalk samples and obtained three phase relative permeability from an optimization technique using a general purpose three phase simulator. Akin and Demiral[35] obtained three phase relative permeability from unsteady state displacement experiments using an automated history matching technique.

Despite the large body of experimental three phase relative permeabilities, most numerical models of three phase flow in porous media use empirical relationships for capillary pressure and relative permeability[36, 37, 38, 39, 40, 41] that are based on extrapolation of two phase data. Baker[42], Delshad and Pope[43], Oak[33] and Fayers and Matthews[44] compared empirical models

to published experimental data and showed that in most cases the empirical models fail to match the measurements.

2.2 Our Approach to the Three Phase Flow Problem

2.2.1 Three Phase Gravity Drainage

We use CT scanning at two different X-ray energies to measure two independent saturations as a function of distance and time during a displacement experiment. From this and the capillary pressure it is possible to obtain a direct measurement of three phase relative permeability. This approach overcomes some of the limitations of previous approaches; namely ignoring capillary pressure[25, 28, 31] or using a possibly non-unique history matching process to obtain relative permeabilities.[23, 35]

While previous work has shown that three phase gravity drainage in water wet porous media leads to low oil saturations through the slow drainage of oil layers in the pore space,[1, 2, 3, 4] there are still several unresolved issues, including:

1. The typical functional form of the oil relative permeability, particularly at low saturation.
2. The effect of spreading coefficient on relative permeabilitiy. While some experiments have shown that spreading coefficient has a large effect on the recovery,[23] others have shown little variation.[1, 24]

Recent theoretical work based on consideration of three phase flow at the pore scale has lead to the following predictions which attempt to answer the points above:[13, 14, 15, 16]

1. That at low oil saturation, where flow is controlled by layer drainage, $k_{ro} \sim {S_o}^2$. At higher saturation k_{ro} is governed by the network of pores filled with oil and $k_{ro} \sim {S_o}^a$, with an exponent $a \approx 4$.
2. That layer drainage is possible for both spreading and non-spreading systems, but that the range of capillary pressures over which layers may form decreases with decreasing spreading coefficient. This means that for a non-spreading oil, the layer drainage regime may be absent. At higher saturations k_{ro} is insensitive to spreading coefficient.

We performed a series of three phase gravity drainage experiments under different spreading and initial conditions, in water-wet consolidated and unconsolidated media in order to test these theoretical predictions. To obtain different spreading conditions we use three different oils; n-hexane, n-octane and n-decane. Table 2.1 gives a list of the experiments performed.

2.2.2 Analysis of Gravity Drainage Experiments

Equations to find the relative permeability during gravity drainage can be obtained from a rearrangement of the multi-phase Darcy law, the capillary pressure equations and the conservation equation for each phase. We develop here equations needed to compute relative permeability during a three phase gravity drainage experiment.

For three phase flow we can write Darcy's law for each of the three phases as

$$u_w = -\frac{k k_{rw}}{\mu_w}\left(\frac{\partial p_w}{\partial z} - \rho_w g\right) \tag{2.1}$$

Table 2.1: Three Phase Gravity Drainage Experiments. S_{oi} is the initial oil saturation averaged over the whole core. S_{of} is the final oil saturation at the end of the experiment averaged over the top half of the column (top 45 cm). S_{wf} is the final average water saturation in the top half of the column. The $*$ indicates waterflood residual oil (S_{or})

Expt.	*Oil*	*Medium*	S_{oi}	S_{of}	S_{wf}
1	n-octane	sand	0.81	0.012	0.11
2	n-octane	sand	0.13*	0.01	0.16
3	n-octane	sand	0.15	0.021	0.16
4	n-hexane	sand	0.80	0.013	0.21
5	n-decane	sand	0.85	0.124	0.18
6	n-octane	sandstone	0.30*	0.189	0.51

$$u_o = -\frac{kk_{ro}}{\mu_o}(\frac{\partial p_o}{\partial z} - \rho_o g) \tag{2.2}$$

$$u_g = -\frac{kk_{rg}}{\mu_g}(\frac{\partial p_g}{\partial z} - \rho_g g) \tag{2.3}$$

By definition $z = 0$ is the top of the column and z increases downwards.

In our experiments, air is the gas phase, which flows very slowly. Thus to a very good approximation there is no potential gradient in the gas phase. Thus,

$$\frac{\partial p_g}{\partial z} = \rho_g g \tag{2.4}$$

or

$$p_g = \rho_g g z \tag{2.5}$$

where we define $p_g = 0$ at $z = 0$.

We can write the capillary pressure equations as

$$p_g - p_o = p_{cgo} \tag{2.6}$$

$$p_o - p_w = p_{cow} \tag{2.7}$$

Therefore

$$u_o = \frac{kk_{ro}}{\mu_o}(\frac{\partial p_{cgo}}{\partial z} + \Delta\rho_{go} g) \tag{2.8}$$

$$u_w = \frac{kk_{rw}}{\mu_w}\left(\frac{\partial p_{cow}}{\partial z} + \frac{\partial p_{cgo}}{\partial z} + \Delta\rho_{wg}g\right) \tag{2.9}$$

where

$$\Delta\rho_{go} = \rho_o - \rho_g \tag{2.10}$$

and

$$\Delta\rho_{wg} = \rho_w - \rho_g \tag{2.11}$$

Conservation of water implies

$$\phi\frac{\partial S_w}{\partial t} + \frac{\partial u_w}{\partial x} = 0 \tag{2.12}$$

Hence

$$u_w|_z = -\int_0^z \phi\frac{\partial S_w}{\partial t}dz \tag{2.13}$$

where the integration is taken from the top of the column ($z = 0$).
Conservation of oil implies

$$\phi\frac{\partial S_w}{\partial t} + \frac{\partial u_o}{\partial x} = 0 \tag{2.14}$$

Hence

$$u_o|_z = -\int_0^z \phi\frac{\partial S_o}{\partial t}dz \tag{2.15}$$

Thus the equations for the water and oil relative permeabilities are from Eqs. 2.8, 2.9, 2.13 and 2.15.

$$k_{ro} = -\frac{\mu_o\phi}{k}\frac{\int_0^z \frac{\partial S_o}{\partial t}dz}{\left(\frac{\partial p_{cgo}}{\partial z} + \Delta\rho_{go}g\right)} \tag{2.16}$$

$$k_{rw} = -\frac{\mu_w\phi}{k}\frac{\int_0^z \frac{\partial S_w}{\partial t}dz}{\left(\frac{\partial p_{cow}}{\partial z} + \frac{\partial p_{cgo}}{\partial z} + \Delta\rho_{ow}g\right)} \tag{2.17}$$

For a two phase, air/water experiment, a similar derivation gives

$$k_{rw} = -\frac{\mu_w\phi}{k}\frac{\int_0^z \frac{\partial S_w}{\partial t}dz}{\left(\frac{\partial p_{cgw}}{\partial z} + \Delta\rho_{gw}g\right)} \tag{2.18}$$

To calculate the relative permeabilities, we need in-situ saturation measurements as a function of time and distance along the core. We also have to measure the capillary pressure.

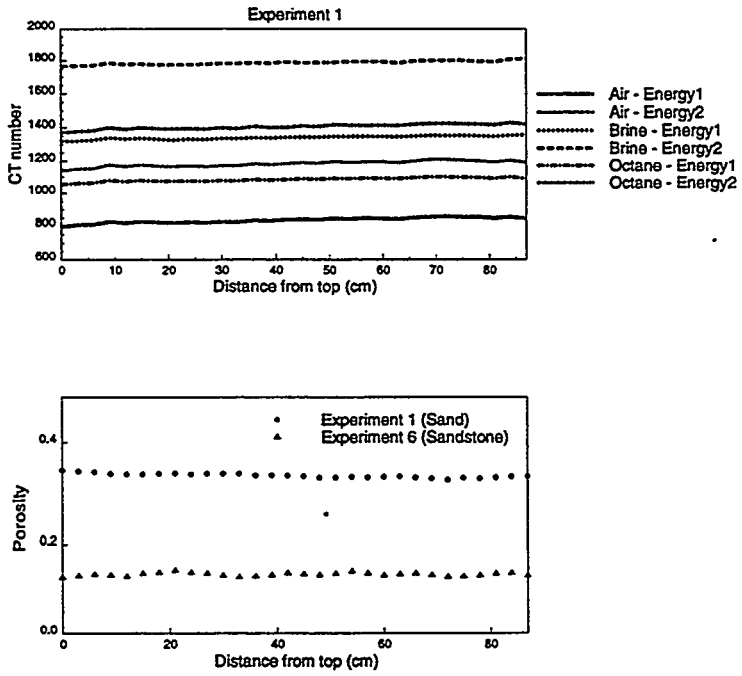

Figure 2.1: Calibration and porosity measurements from the CT Scanner.

2.3 Dual Energy CT scanning and Experimental Design

CT scanning is a widely used tool in the petroleum industry[45, 46, 47] and has successfully measured saturation distributions in porous media. There are three methods that have been used to monitor three phase flow experiments in porous media using CT scanning. The first technique assumes that one of the three phases is immobile, and the calculations are the same as the two phase calculations. MacAllister *et. al*[48] used this method to obtain quantitative estimates of oil, water and gas saturation distributions, assuming the oil phase to be immobile. The oil saturation was estimated by an independent measurement. The authors used two phase CT scans to determine residual oil saturations, in presence of water and gas.

Another way of analyzing three phase flow experiments using CT scanning involves matching the CT numbers of two fluids and treating them as a single phase. Siddiqui *et. al*[31] used this method to analyze three phase flow experiments. Water, benzyl alcohol and decane were used as the three immiscible phases in the experiment. Water and decane were tagged with iodine to match their CT response, and this allowed the determination of benzyl alcohol saturation with a single high energy scan. However, using this technique it is not possible to separate the water and decane saturations.

The third approach, which we used, is to scan at two different energies to obtain three phase saturations. We used a Picker 1200X fourth generation medical CT scanner with 1200 stationary detectors. The CT scanner was modified to rotate a complete 90 degrees to scan both horizontal and vertical experiments. A remotely operated vertical positioning system mounted on the scanner allowed the vertical movement of the object in the scan frame to an accuracy of 1/100th of a mm.

At the same location two scans were taken at two different energy levels. The lower energy scan was at 80 kV and the higher energy scan was at 140 kV. We scanned the core dry, fully saturated with brine (water phase) and fully saturated with oil at the two energy levels. The brine was a 10% by weight solution of sodium bromide. Table 2.3 shows the properties of the fluids used. From the dry core scans and 100% brine saturated scans, we obtained the porosity along the length of the core using Eq. 2.33.

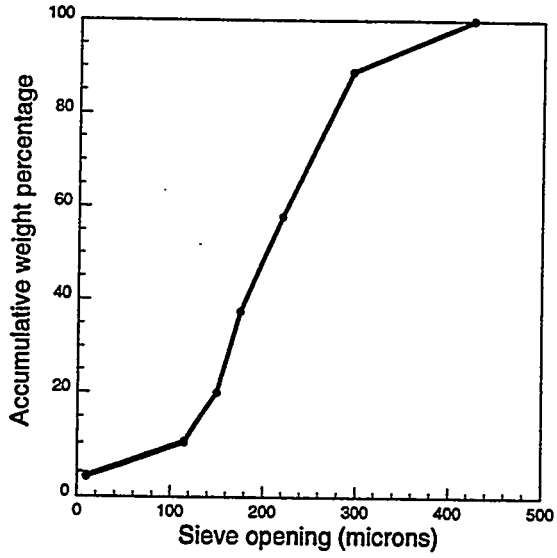

Figure 2.2: Results of sieve analysis for the sand used in this study.

Table 2.2: Fluid Properties

Fluid	*Density* $grams/cc$	*Viscosity* cp
n-hexane	0.659	0.30
n-octane	0.703	0.51
n-decane	0.730	0.84
brine	1.010	1.00

We performed experiments on a uniform sandpack and a consolidated and layered Berea sandstone. Fig. 2.1 shows the calibration scans for the sand and porosity measurements for the sand and Berea. Fig. 2.2 shows the results of sieve analysis on the sand. The sand had a permeability of 12 D and a porosity (obtained from CT scanning) of 33.8% averaged over four packs. The Berea had a permeability of 79 mD and an average porosity of 13.4%.

For our experiments, 7.62 cm in diameter and 90 cm long cores were used. The coreholders were standard Hassler-type with overburden fluid and rubber sleeve. The coreholders were hung from the vertical positioning system mounted above the scanner. The barrel was a PVC pipe (4 inch, Schedule 80) with polypropylene distribution plate endplugs. The overburden fluid was controlled through the endplugs and had a pressure of 50 psi.

2.3.1 Experimental Procedure

All experiments were performed at laboratory temperature and pressure conditions. An outline of the experimental procedure is given below.

1. After the dry scans, carbon dioxide was injected to drive out the air.

2. Five pore volumes of brine were injected from the bottom of the core at 5cc/min untill the core was fully saturated. The core was scanned.

3. Isopropyl alcohol was injected from the top of the column. Isopropyl alcohol is a solvent which dissolves both water and oil.

4. Oil was injected from the top until the core was fully saturated with oil. The core was scanned.

5. The core was cleaned with isopropyl alcohol.

6. Brine was injected to make the core water-wet. All experiments are performed under water-wet conditions.

7. Oil was injected until connate water saturation was reached. This was the initial condition in experiments 1, 4 and 5. In experiments 2, 3 and 6, brine was then injected to establish initial conditions.

8. The core drained freely under gravity by allowing air to enter from the top. To reduce the vaporization of the fluids in the porous medium, the air entering the core was passed through oil and water, kept in separate containers.

9. The core was scanned during the gravity drainage to obtain in-situ measurements of phase saturations as a function of time and distance along the length of the core. At a given time, the core was scanned every 3 cm along its length.

2.3.2 Analog Experiments

Precise measurements of capillary pressure were obtained from analog experiments performed on the same sand and with the same fluids, in glass columns approximately 1 meter in length and 2 cm in diameter. The procedure for the analog experiments is similar to that for the CT experiments. These experiments could not be performed on Berea. How we obtained capillary pressure from Berea is described at the end of this section.

1. After weighing the pack, carbon dioxide was injected to drive out the air.

2. This was followed by injecting brine as in the CT experiments.

3. The column and stand were weighed again. The average porosity of the sandpack was obtained from the volume of brine in the column. The average porosity value for the sand column was 34.2%. This is close to the porosity obtained from CT scanning (33.8%).

4. Oil was injected from the top of the column at 2 cc/min till no further brine was eluted. Three analog experiments were performed with hexane, octane and decane as the oil phase. A two phase experiment was performed with brine as the liquid phase.

5. The sand column was let to drain freely under gravity by letting in air from the top. After 7 weeks, when we assumed that the fluids were no longer flowing, sand was taken out in 3 cm intervals along the length of the column. The extracted sand and fluids were washed with 50 cm^3 of iso-proponal, a solvent that dissolves both oil and water.

6. The samples were run through a gas chromatograph (HP 5880A series machine) which was calibrated by known volumes of fluids mixed in the solvent.

7. We assume that the sand column had a uniform porosity. Thus we can estimate the total pore volumes of each sample of sand. From the gas chromatograph we obtained the saturation of each phase.

8. At equilibrium the pressure in the fluids was the gravitational head, and capillary pressures were obtained as follows:

$$p_{cow}(s_w) = -(\rho_w - \rho_o)gz + constant \tag{2.19}$$

and

$$p_{cgo}(s_o + s_w) = -(\rho_o - \rho_g)gz + constant \tag{2.20}$$

We tabulated the results to find p_{cgo} and p_{cow} for any value of s_o and $(s_o + s_w)$.

$$\frac{\partial p_{cow}}{\partial z} = \frac{p_{cow}(s_w|_z) - p_{cow}(s_w|_{z+})}{\Delta z} \tag{2.21}$$

where $z+$ is the distance to the next scan location and $\Delta z = 3$ cm, is the distance between two scan locations.

Similarly we can find $\frac{\partial p_{cgo}}{\partial z}$ and use the partial derivatives of capillary pressures in Eqs. 2.16 and 2.17 to obtain k_{ro} and k_{rw}.

In a two phase air/water experiment we find

$$\frac{\partial p_{cgw}}{\partial z} = \frac{p_{cgw}(s_w|_z) - p_{cgw}(s_w|_{z+})}{\Delta z} \tag{2.22}$$

And this is used in Eq. 2.18 to find k_{rw}.

This procedure cannot be used for consolidated rock. In this case the capillary pressure was obtained from the saturation distribution measured by CT scanning, at the end of the experiment, after 1600 hours of drainage. We assumed that after 1600 hours (9.5 weeks) the fluids were no longer flowing.

2.3.3 Measuring the Spreading Coefficient

The spreading coefficient is defined as:

$$C_s = \gamma_{gw} - \gamma_{ow} - \gamma_{go} \tag{2.23}$$

We measured the interfacial tensions γ_{gw}, γ_{ow}, γ_{go} by the Drop Weight Method.[49] The fluids used were the same as those in the experiments. Strictly speaking we measure the initial spreading coefficient - that is the value before the three fluids obtain thermodynamic equilibrium. If $C_s > 0$, the oil will spread on a flat water surface, while for $C_s < 0$ it will not. However, the configuration of three phases at the pore scale is governed by the equilibrium spreading coefficient, $C_s{}^e$, where γ_{gw} may be lowered due to the presence of a molecular oil film ($C_s{}^e \leq 0$).[5, 16, 49]

The oil/brine and oil/air interfacial tensions are given in Table 2.3. The measured brine/air interfacial tension is 72 mNm^{-1}. The spreading coefficient is computed using Equation 2.23.

Table 2.3: Interfacial tensions and spreading coefficient

Fluid	γ_{ow} (mNm^{-1})	γ_{go} (mNm^{-1})	C_s (mNm^{-1})
n-hexane	50.5	18.0	3.5
n-octane	51.2	21.1	-0.3
n-decane	51.4	23.7	-3.1

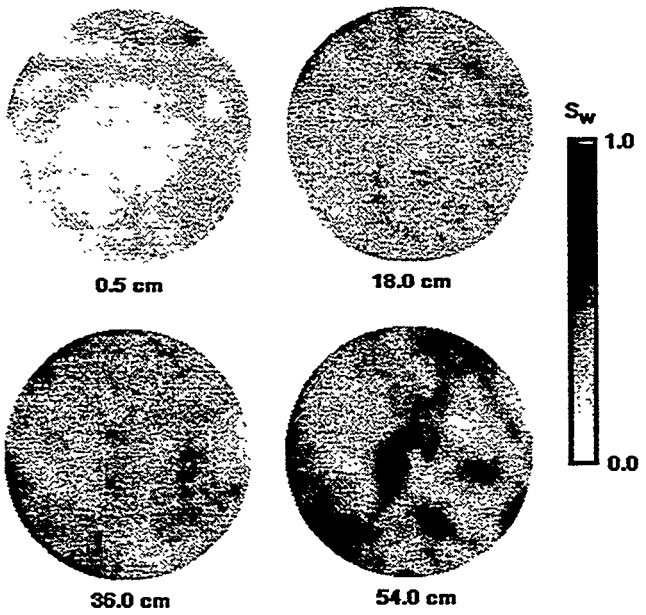

Figure 2.3: In-situ saturation measurements at different locations along the length of the core after 2.50 hours of drainage.

2.3.4 In-situ Saturation Measurements from Scanned Images

In this section we show how saturation measurements were obtained by example of a two phase air-water gravity drainage experiment. A fully water saturated sandpack drained freely under gravity and was scanned for a period of 117 hours. The drainage rates were higher at the beginning, so the sandpack was scanned frequently at the start of drainage. CT images of the saturation distribution for different slices along the length of the sand column after 2.5 hours of drainage are shown in Fig. 2.3. The appendix shows how the saturations were obtained from the CT numbers and provides an error analysis.

The water and air saturation profiles were obtained by averaging the saturations at each scan location. Averaging saturation over each slice in Fig. 2.3 gave one data point for the saturation profile. The water and air saturation profiles as a function of time and distance along the length of the core are given in Fig. 2.4. The air/water capillary pressure was obtained by an analog two phase air-water gravity drainage experiment. The relative permeability was found from Eq. 2.18 and is shown in Fig. 2.5. Each saturation measurement gave one relative permeability data point in Fig. 2.5. The three phase relative permeability was obtained in a similar way.

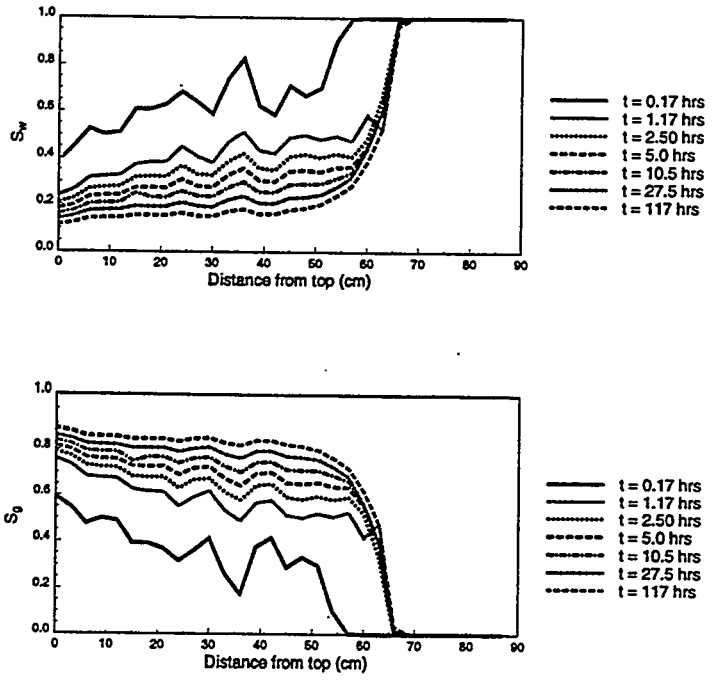

Figure 2.4: Water and air saturation profiles as a function of time and distance along the length of the core.

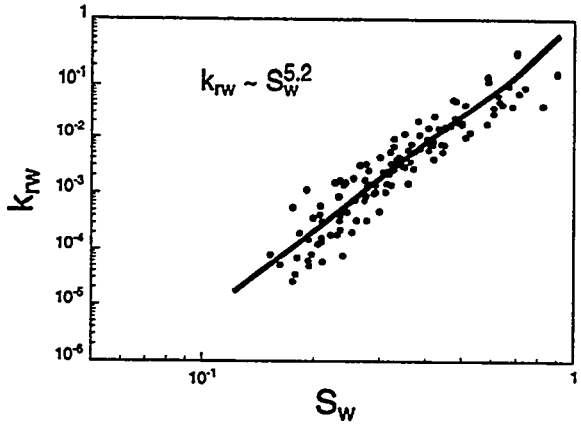

Figure 2.5: Water relative permeability as a function of water saturation. The straight line is a best fit through the data on the doubly logarithmic axes.

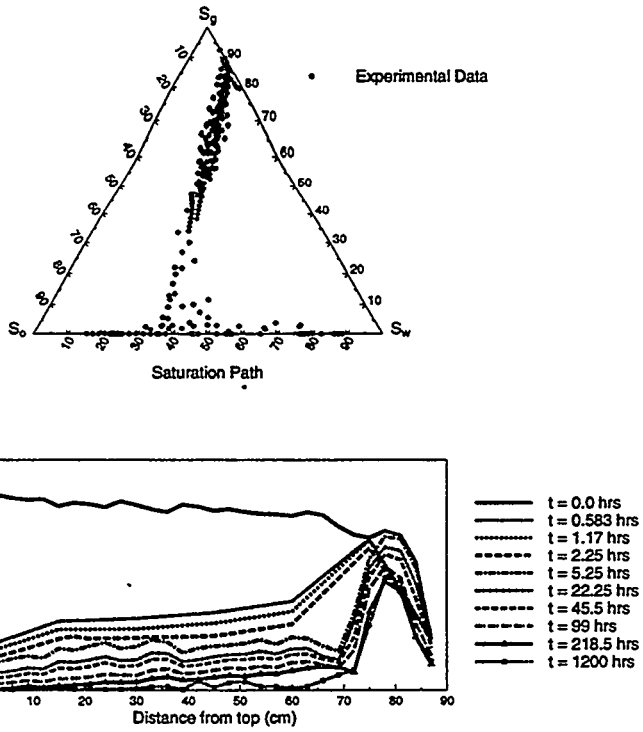

Figure 2.6: Saturation path and oil saturation profile for experiment 1.

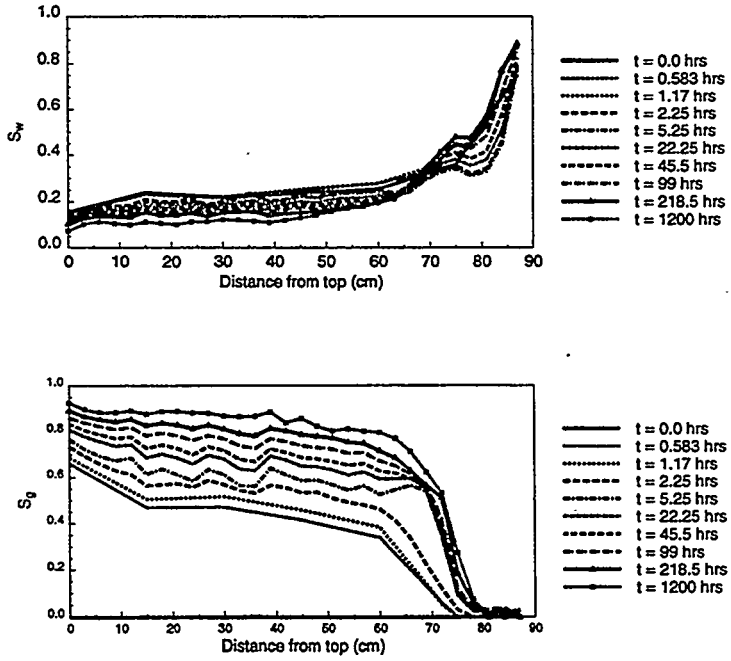

Figure 2.7: Water and air saturation profiles as a function of time and distance for experiment 1.

2.4 Three Phase Gravity Drainage Experiments

Table 2.1 shows the initial and final oil saturations for the experiments performed. Figures 2.6 and 2.7 show the saturation path and saturation profiles for experiment 1 where the oil was octane and $S_{oi} = 0.81$. Experiment 2 was similar except that the initial oil saturation represents waterflood residual oil. Three phase gravity drainage displaced almost all of the waterflood residual oil. Experiment 3 used octane with $S_{oi} = 0.15$. Experiment 4 used hexane while experiment 5 used decane.

Experiment 6 was performed on a consolidated Berea sandstone with octane as the oil phase. After the calibration scans the core was flooded with water and this was followed by injection of oil. The core was then waterflooded till the oil saturation reached 30%. Air was then injected slowly at the rate of 0.16cc/min from the top and fluids were allowed to drain from the bottom. Air injection was used in this experiment to speed up the drainage process. However, the injection rate was chosen to be sufficiently low that the pressure gradient in the air phase was small and the analysis to find k_{ro} and k_{rw} was still valid. The average oil saturation in the top half of the core after 1600 hours of drainage was 18.9%.

From these experiments we obtained the saturations as a function of time and distance along the length of the core. The capillary pressures were obtained from analog experiments and were used along with the saturation measurements in Eqs. 2.16 and 2.17 to obtain three phase relative permeabilities.

2.5 Results and Discussion

Fig. 2.8 shows the water relative permeabilities for experiments performed on sand with octane as the oil phase. Water relative permeabilities were not obtained for experiments 4 and 5 since the initial water saturations here were low and there was very little displacement of water. For experiment 6, only data from the top half of the core was used to obtain the relative permeability. The initial water saturation in the lower half of the core was not uniform and this lead to a large scatter in the computed k_{rw}.

Fig. 2.9 gives the oil relative permeabilities for all six experiments.

A study of Figs. 2.8 and 2.9 reveal the following features:

1. To within experimental error k_{rw} is independent of initial condition. Other work[33] on three phase flow has also shown that k_{rw} is a function only of its own saturation, and is independent of S_{oi}. k_{rw} falls very steeply with S_w, and $k_{rw} \sim {S_w}^a$, with $a \approx 5$. To within experimental error, k_{rw} is the same for the two phase and three phase experiments performed on sand.

2. k_{ro} is independent of S_{oi}. (Compare k_{ro} for experiments 1, 2 and 3).

3. At high oil saturations, $S_o > S_{or}$, k_{ro} is independent of spreading coefficient. $k_{ro} \sim {S_o}^a$, with $a \approx 4$. (Compare k_{ro} for experiments 1, 4 and 5).

4. At low oil saturations, $S_o < S_{or}$, k_{ro} is sensitive to spreading coefficient. k_{ro} is slightly higher for hexane than octane, while for decane, S_o never falls below 0.09. (Compare k_{ro} for experiments 1, 4 and 5).

5. For $S_o < S_{or}$, with the exception of decane, we see $k_{ro} \sim S_o^a$, with $a \approx 2$.

Observation 5 is perhaps the most remarkable and suggests a very simple universal form for k_{ro} at low saturation for water-wet media. In confirmation of this hypothesis, Fig. 2.10 shows the oil relative permeability in a Clashach sandstone.[25] Fig. 2.11 shows the k_{ro} for three phase flow

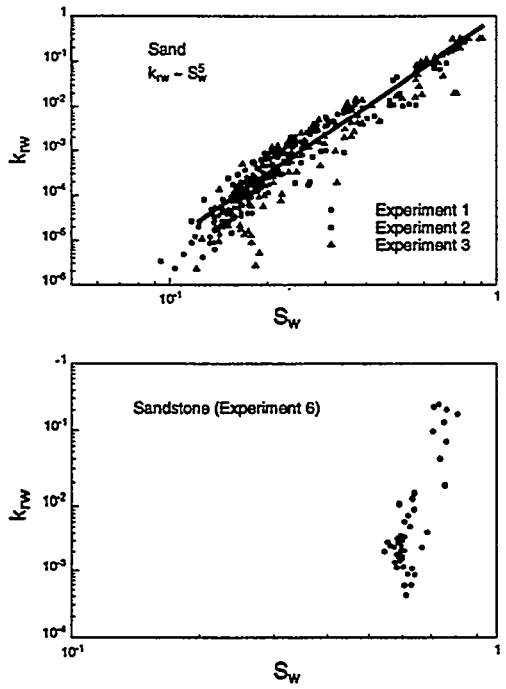

Figure 2.8: Water relative permeability as a function of water saturation. The straight line in the top figure is a best fit through the data. Notice that the results of the three experiments lie on a single curve, which is similar to the two phase results in Fig. 2.5.

in bead packs with analog fluids.[28] In both cases we see $k_{ro} \sim S_o^2$ at low oil saturation. Similar results were obtained by Goodyear and Jones.[50]

The quadratic form for k_{ro} is a direct consequence of layer drainage at the pore scale.[16] Fig. 2.12 shows an idealized corner in a pore space. The essential features are that the rock is water-wet and that there are roughness, grooves or crevices that act as conduits for wetting fluid, even when the center of the pore is filled with gas. Oil may reside in a layer of order of microns in thickness, wedged between the water and gas, as shown. At low S_o, gas occupies most of the pore space, while oil is primarily confined to layers. The oil saturation is proportional to the cross-sectional area of the layer. Simple analysis can show that the layer conductance and hence relative permeability is proportional to oil area squared. Hence, macroscopically, $k_{ro} \sim S_o^2$. At higher S_o, k_{ro} is governed by the arrangement of pores filled with oil and layer drainage no longer dominates the flow. In this regime, pore network modeling can successfully predict the $k_{ro} \sim S_o^4$ seen in these experiments. Since it is layer drainage that accounts for the displacement of waterflood residual oil during inert gas injection, we postulate that the layer drainage regime is observed for $S_o < S_{or}$. This is consistent with the experimental results.

Layer drainage was observed for both hexane and for octane, whose initial spreading coefficient was slightly negative. Both hexane and octane may be loosely considered spreading oils in the sense that their equilibrium spreading coefficients are probably close to zero and they readily form oil layers in the pore space. Note, however, that octane does not spread on a flat brine surface ($C_s < 0$), but does show the layer drainage regime with a very low final oil saturation.

While n-decane may form layers in the pore space in micromodel experiments,[8, 14] the range of capillary pressures for which these layers are stable decreases with decreasing spreading coefficient and network modeling has shown that the layer drainage regime may not be observed for a decane system.[16] Experiment 5 confirms this: there is an apparent $S_{or} \approx 0.1$ and no layer

drainage regime. This implies that for n-decane there was no recovery through oil layers.

Notice that the k_{rw} curves do not display a layer drainage regime ($k_{rw} \sim S_w^2$), but that k_{rw} falls very sharply with S_w. This is because even at low S_w, the water being the most wetting phase, completely fills some small pores and crevices which may be poorly connected. This makes k_{rw} sensitive to the exact arrangement of water-filled regions of the pore space, similar to the k_{ro} regime for $S_o > S_{or}$.

2.6 Summary and Conclusions

1. Dual-energy scanning using a modified CT scanner was used to obtain independent measurements of two saturations as a function of time and distance along the length of the core. Capillary pressure was obtained from analog experiments.
2. In six gravity drainage experiments on water-wet porous media, hexane, octane and decane were used as the oil phases to study the effect of spreading coefficient on relative permeability.
3. Very low oil saturations are observed during three phase gravity drainage experiments for octane and hexane.
4. For the spreading systems (hexane and octane), the oil relative permeability, $k_{ro} \sim {S_o}^4$ for $S_o > S_{or}$ and then exhibited a crossover to $k_{ro} \sim {S_o}^2$ for lower oil saturations.
5. This quadratic form of the relative permeability was seen down to oil saturations as low as 1.5%. This is consistent with layer drainage at the pore scale.
6. In the non-spreading system (decane), this layer drainage regime was not observed

2.7 Nomenclature

C_s = spreading coefficient
k = absolute permeability
k_{rp} = relative permeability to phase p
p_p = pressure of phase p
p_{cgo} = gas oil capillary pressure
p_{cow} = oil water capillary pressure
S_p = saturation (p = o, g, w)
S_{or} = waterflood residual oil saturation
S_{oi} = initial oil saturation
u_p = flow velocity of phase p

Greek Letters

γ = interfacial tension
ν = x-ray attenuation of material
ϕ = porosity
ρ_p = density of phase p

Subscripts

1 = first energy level
2 = second energy level
i = initial condition
g = gas
o = oil
p = phase
r = rock
w = water (brine)

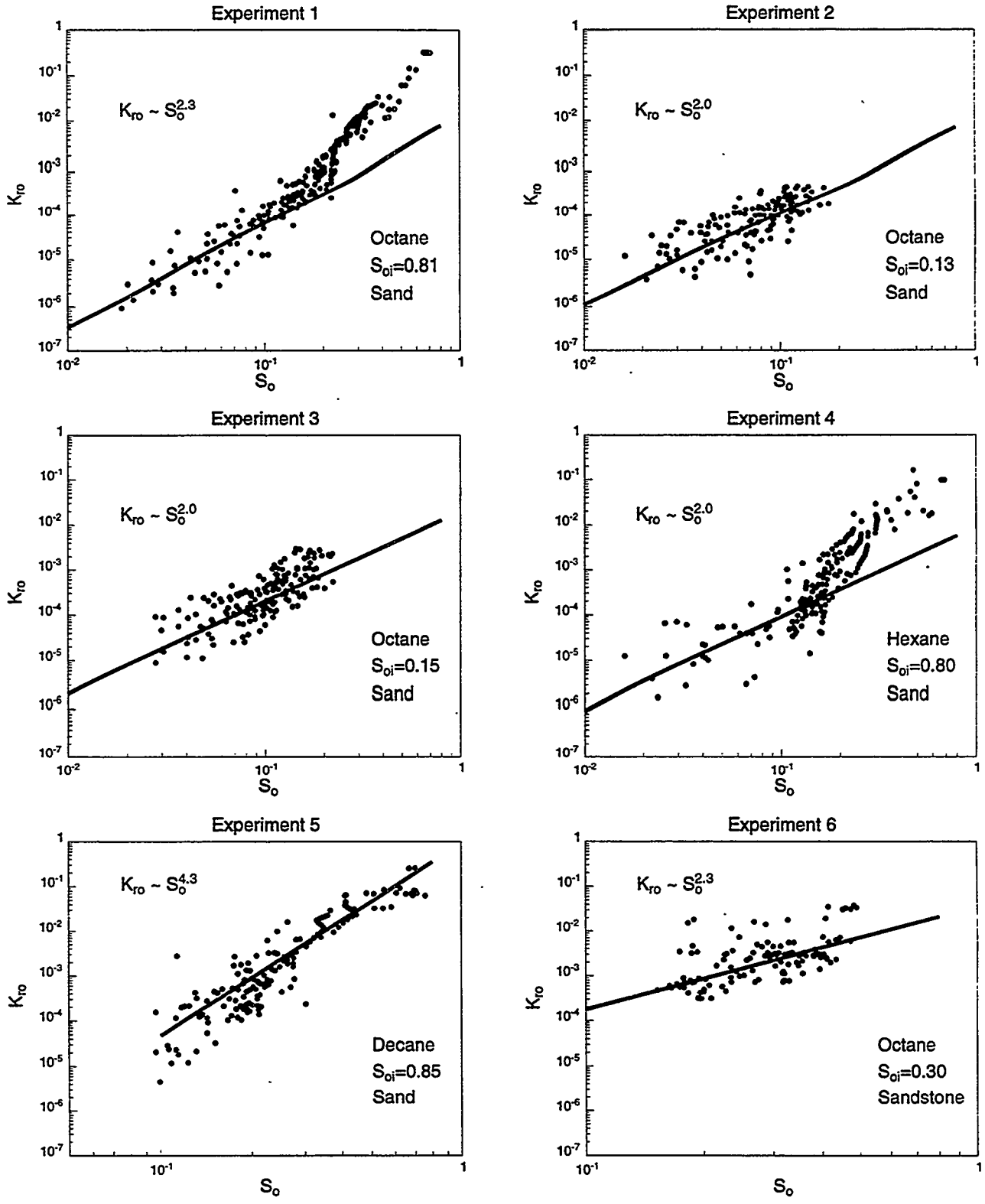

Figure 2.9: Measured oil relative permeabilities. The straight lines are best fits to the data at low oil saturation. Notice that all the curves show an approximately quadratic form for the oil relative permeability at low oil saturations, except for the non-spreading decane system.

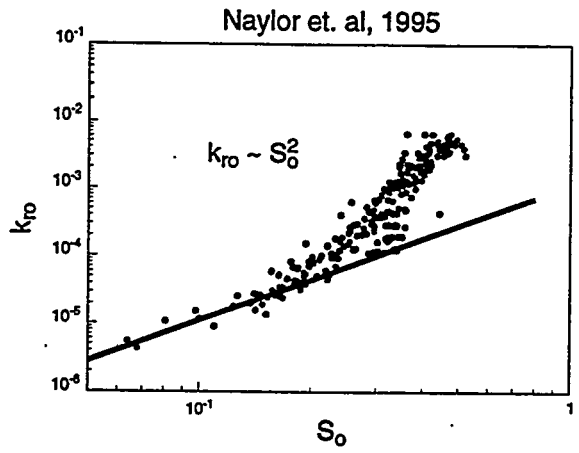

Figure 2.10: Oil relative permeability from Naylor *et. al.*[25]

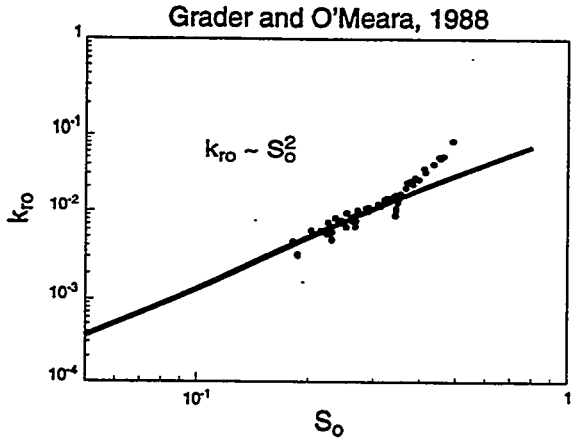

Figure 2.11: Oil relative permeability from Grader and O'Meara.[28]

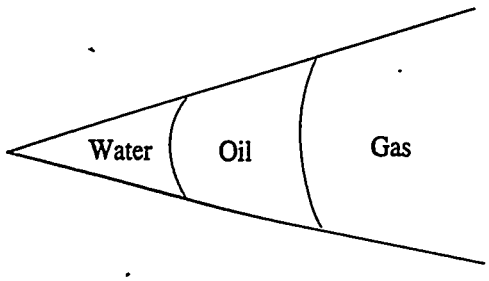

Figure 2.12: Fluid distribution in the corner of a pore space.

2.8 Appendix A

2.8.1 Three Phase Saturation Calculation

The equations for three phase saturation calculations using dual-energy CT scanning are derived in the following section. For each energy level, the CT numbers of a core containing three fluids at energy levels 1 and 2 are given by the equations:

$$CT_1 = (1-\phi)\nu_{r1} + \phi s_g \nu_{g1} + \phi s_o \nu_{o1} + \phi s_w \nu_{w1} \tag{2.24}$$

$$CT_2 = (1-\phi)\nu_{r2} + \phi s_g \nu_{g2} + \phi s_o \nu_{o2} + \phi s_w \nu_{w2} \tag{2.25}$$

where ν is the xray attenuation coefficient of the material.
Also

$$S_g = 1 - S_o - S_w \tag{2.26}$$

This gives us three equations with three unknowns.
The CT numbers for the dry scans are

$$CT_{gr1} = (1-\phi)\nu_{r1} + \phi\nu_{g1} \tag{2.27}$$

and

$$CT_{gr2} = (1-\phi)\nu_{r2} + \phi\nu_{g2} \tag{2.28}$$

This gives

$$S_o = \frac{[CT_1 - CT_{gr1}](\phi\nu_{w2} - \phi\nu_{g2}) - [CT_2 - CT_{gr2}](\phi\nu_{w1} - \phi\nu_{g1})}{(\phi\nu_{o1} - \phi\nu_{g1})(\phi\nu_{w2} - \phi\nu_{g2}) - (\phi\nu_{o2} - \phi\nu_{g2})(\phi\nu_{w1} - \phi\nu_{g1})} \tag{2.29}$$

$$S_w = \frac{[CT_2 - CT_{gr2}](\phi\nu_{o1} - \phi\nu_{g1}) - [CT_1 - CT_{gr1}](\phi\nu_{o2} - \phi\nu_{g2})}{(\phi\nu_{o1} - \phi\nu_{g1})(\phi\nu_{w2} - \phi\nu_{g2}) - (\phi\nu_{o2} - \phi\nu_{g2})(\phi\nu_{w1} - \phi\nu_{g1})} \tag{2.30}$$

To account for the influence of the rock, add and subtract $(1-\phi)(\nu_{ri})$ for i = 1 and 2 into each parentheses.
The equations now become

$$S_o = \frac{[CT_1 - CT_{gr1}](CT_{wr2} - CT_{gr2})[CT_2 - CT_{gr2}](CT_{wr1} - CT_{gr1})}{(CT_{or1} - CT_{gr1})(CT_{wr2} - CT_{gr2}) - (CT_{or2} - CT_{gr2})(CT_{wr1} - CT_{gr1})} \tag{2.31}$$

$$S_w = \frac{[CT_2 - CT_{gr2}](CT_{or1} - CT_{gr1})[CT_1 - CT_{gr1}](CT_{or2} - CT_{gr2})}{(CT_{or1} - CT_{gr1})(CT_{wr2} - CT_{gr2}) - (CT_{or2} - CT_{gr2})(CT_{wr1} - CT_{gr1})} \tag{2.32}$$

2.8.2 Calculating Porosity

The porosity of the core can be obtained by scanning the core dry and then scanning it fully saturated with water(brine).

$$\phi = \frac{CT_{wr} - CT_{gr}}{CT_w - CT_g} \tag{2.33}$$

where CT_w and CT_g are the pure fluid CT numbers for water and gas respectively. They are obtained by scanning the pure fluids inside the coreholder in place of the core. This helps in eliminating beam hardening effects due to the coreholder material and artifacts that effect the fluid CT number. CT_{wr} and CT_{gr} are the CT numbers of the core fully saturated with water and air respectively.

2.8.3 Error Analysis

All CT measurements have errors associated with them. Error is defined as the standard deviation in CT number on a pixel by pixel basis of a 2" diameter fused quartz sample in the same setup as the experiments. A fused quartz sample was placed in the coreholder and scanned at the two energy levels. The error in CT number for energy level 1 is 2.6 and for energy level 2 is 5.6.

From this we find that the error in the oil and water saturations calculated from Eqs. 2.31 and 2.32 is 4.3% and 9.3% respectively. The error in the gas saturation is 13.6%. In our calculations for relative permeability, we average the saturation over a slice (approximately 27500 pixels). If we assume the error to be independent and random, then the average error in the oil saturation over the slice is 0.026% The average errors in the water and gas saturations are 0.056% and 0.082% respectively. These errors are tiny and result in very little scatter in computed relative permeability. Thus the observed scatter in the measurements is attributed to the local inhomogeneities in the permeability and porosity of the porous media, together with non-uniform initial conditions. Smoothing the saturation profiles would give us less scatter in the relative permeability curves.

3. The Effect of Wettability on Three-Phase Relative Permeability

David A. DiCarlo, Akshay Sahni, and Martin Blunt

We study three-phase flow in water-wet, oil-wet, and fractionally-wet sandpacks. We use CT scanning to measure directly the oil and water relative permeabilites for three-phase gravity drainage. In an analogue experiment, we measure pressure gradients in the gas phase to determine the gas relative permeability. Thus we find all three relative permeabilities as a function of saturation. We find that the gas relative permeability is approximately half as much in a oil-wet system than in an water-wet system at the same gas saturation. The water relative permeability in the water-wet pack and the oil relative permeability in the oil-wet pack are similar. In the water-wet medium the oil relative permeability scales as $k_{ro} \sim S_o^4$ for $S_o > S_{or}$, where S_{or} is the waterflood residual oil saturation. With octane as the oil phase, $k_{ro} \sim S_o^2$ for $S_o < S_{or}$, while with decane as the oil phase, k_{ro} falls sharply for $S_o < S_{or}$. The water relative permeability in the oil-wet medium resembles the oil relative permeability in the water-wet medium for a non-spreading oil such as decane. These observations can be explained in terms of wetting, spreading, and the pore scale configurations of fluid.

3.1 Introduction

Understanding the dynamics of three-phase (water, oil, and gas) flow in porous media is essential for optimizing enhanced oil recovery and vadose zone remediation of oil spills. For enhanced oil recovery, three-phase flow will occur during gas injection, gas cap expansion, and surfactant flooding among other processes. Three-phase flow is also important in contaminant migration and clean up. For instance, oil or other non-aqueous phase liquid (NAPL) spilled on the ground will migrate through the unsaturated zone under three-phase conditions until it penetrates the water table. In either case, the ultimate recovery of oil and other NAPLs depends on the residual saturations and relative permeabilites of each of the phases.

Three-phase flow has unique and important features that are not found in two-phase flow. In two-phase flow, one phase will wet the porous media more than the other phase. This wetting phase occupies the smaller pores, crevices, and corners while the non-wetting phase occupies the larger pores with the exact mix determined by the capillary pressure. Regardless of which pair of fluids are used (gas/water, oil/water, gas/oil) the positioning of the fluids will be somewhat identical at identical saturations. In contrast, for three-phase flow the third phase exists as in intermediate phase which will be positioned uniquely in the porous media, leading to a whole new regime of flow paths. These variations in pore scale positioning of each fluid directly affect the important macroscopic properties of relative permeability and residual saturation.

Many papers [1, 2, 4] have shown that low oil saturations can be reached during three-phase displacements. In addition, a variety of experiments have also measured three-phase relative permeabilities although most of these experiments have been performed on uniformly water-wet media (see Baker et al. [42] for a review of the literature). Oak et al. [33] studied three-phase relative permeabilities in an intermediate-wet Berea sandstone. Vizika et al. [23] studied three-phase drainage in porous media of varying wettability, although they obtained permeabilities only from the outflow data. Lombard and Lenormand [53] obtained two-phase relative permeabilities in fractionally-wet sand, using a steady-state technique. However, despite this growing body of

Table 3.1: Fluid densities (kg/m^3) [$\rho_w = 1025$ kg/m^3], interfacial tensions (mN/m) and oil spreading coefficients (mN/m).

Oil	ρ_0	γ_{ow}	γ_{go}	γ_{gw}	C_{so}
n-hexane	659	50.5	18.0	72.0	3.5
n-octane	703	51.2	21.1	72.0	-0.3
n-decane	730	51.4	23.7	72.0	-3.1

literature on three-phase flow [33, 6] we still lack a simple physical understanding of three-phase relative permeability that is grounded on direct experimental measurement.

In this chapter we measure three-phase relative permeabilities during the gravity driven displacement of oil and water by gas, which is called gravity drainage. This is an important three-phase process that occurs during gas cap expansion in an oil reservoir and when NAPLs migrate through an unsaturated soil. Gravity drainage is also relatively easy to study experimentally and its analysis avoids consideration of hysteresis effects, which can be very significant in three-phase flow [26, 16].

Using CT scanning to measure saturations during gravity drainage, Sahni et al. [54] measured oil and water relative permeability in water-wet media and studied the effect of spreading coefficient. Zhou et al. [58] performed three-phase gravity drainage in sandpacks that were mixtures of oil-wet and water-wet grains. They measured the saturation distribution at the end of drainage and interpreted the results in terms of the pore scale arrangement of fluid.

We extend Sahni et al.'s (1998) measurements to oil-wet and fractionally-wet (a 50-50 mix of oil-wet and water-wet) media. In addition we measure the gas relative permeability using an analogue experiment in which we directly measure the gas saturation and pressure gradient. Thus we obtain all three permeabilities for three-phase gravity drainage, in water-wet, oil-wet and fractionally-wet sandpacks. We find that the results can be readily explained in terms of the pore scale fluid configurations, in turn allowing us to understand which three-phase properties are expected to be universal.

3.2 Materials and Methods

We chose sandpacks as our porous media as they are easy to characterize and they are easily sectionable for destructive saturation measurements. We used clean industrial sand (no. 60, Corona Industrial Sand Co., Corona, CA) which was initially water-wet. The sand was sieved with a size 120 sieve to remove any fine particles. We made 15 kg of the sand oil-wet by soaking it in a mixture of 20 % crude oil (Thums Inc., Long Beach, CA) and 80 % iso-octane for 24 hours [51]. This oil-wet sand was then rinsed with iso-octane and air-dried. The fractionally-wet sand was a 50-50 mixture of the oil and water-wet sands. We define f as the fraction of water-wet sand, thus the water-wet, fractionally-wet, and oil-wet sand have $f = 0, 0.5, 1$, respectively.

For our fluids, we chose n-hexane, n-octane, or n-decane for the oil phase, 10 % NaBr by weight brine for the water phase, and air for the gas phase. Interfacial tensions were measured using the pendant drop technique [49]. Table 3.1 shows the fluid properties.

3.2.1 Oil and Water Relative Permeabilities

Before and during gravity drainage, we used a dual energy CT scanner to obtain in-situ measurements of the water and oil saturations. This CT method and the calculation of permeabilities from the data are described in greater detail in Sahni et al. [54]. The core holders were standard Hassler-type with an overburden fluid (water at 50 psi) and a rubber sleeve. The sand was packed into the rubber sleeve of diameter 7.6 cm and length 67 cm (87 cm sleeves were used for water-wet sand). The experiment was then calibrated by scanning the core when it was dry, when it was saturated with brine, and when it was saturated with oil. Scans were taken every 2 cm and at energy levels of 80 kV and 140 kV. Using this calibration and a standard linear interpolation of CT number with density, the water, oil, and air saturations could be obtained during a three-phase experiment. The saturations were averaged over each slice to give the average water, oil, and air saturation every 2 cm along the core.

Before drainage each core was set to connate water S_{wc} or residual oil S_{or} saturation as described below. The core was saturated with the most wetting fluid (water for water-wet, oil for oil-wet) and then displaced with 5 pore volumes of the intermediate wetting fluid (oil or water). This produced an initial condition of S_{wc} for the water-wet pack and S_{or} for the oil-wet pack. Separate experiments were performed after an additional flooding of 5 pore volumes of the most wetting fluid to produce an inital condition of S_{or} for the water-wet pack and S_{wc} for the oil-wet pack. For the fractionally-wet pack there is no most-wetting fluid, so an initial condition of S_{or} was achieved by flooding a 100% oil-saturated pack with water, and S_{wc} was achieved by flooding a 100% water-saturated pack with oil. Once the desired initial condition was reached, gas (air) was allowed to enter the top of the system, while water and oil drained out of the bottom under gravity. Before entering the column the air passed through a bubbler filled with water and a bubbler filled with oil to saturate the air with water and oil vapor. The bubblers also provided a one-way pathway for the air such that no oil and water vapor could leave the column through the top port.

The pack was periodically scanned over a period of several weeks to record the saturation distribution versus time. Figure 3.1 shows the saturation profile of octane and water at various times for a water-wet column that was initially at S_{wc}.

We can directly compute the oil and water relative permeabilities at each measured position along the column and for each time from the known evolution of the saturation profile over time $S(z,t)$. We begin with Darcy's law for each phase i in a 1-dimensional vertical displacement,

$$q_i = -\frac{kk_{ri}}{\mu_i}\left(\frac{\partial P_i}{\partial z} - \rho_i g\right), \tag{3.1}$$

where q is the flux, k is the permeability, k_r is the relative permeability, μ is the viscosity, P is the fluid pressure, z is the vertical distance taken to be positive downward, ρ is the density and g is the gravitional constant. We calculate the flux past position z by from integrating the change in the saturation of each phase between scans at time t_1 and t_2

$$q_i = -\frac{(\int S_i(t_2)dz - \int S_i(t_1)dz)}{t_2 - t_1} \tag{3.2}$$

As we are on the drainage curve for each fluid, we assume a unique relationship between the fluid's pressure and saturation (the pressure-saturation curve), which also relates the pressure gradient to the measured saturation gradient.

$$\frac{\partial P_i}{\partial z} = \frac{\partial P_i}{\partial S_i}\frac{\partial S_i}{\partial z} \tag{3.3}$$

Thus, if we also know the capillary pressure - saturation curve, the relative permeabilities k_{rw} and k_{ro} can be calculated directly from Eqs. 1-3. A more detailed formulation is given in Sahni et al. [54].

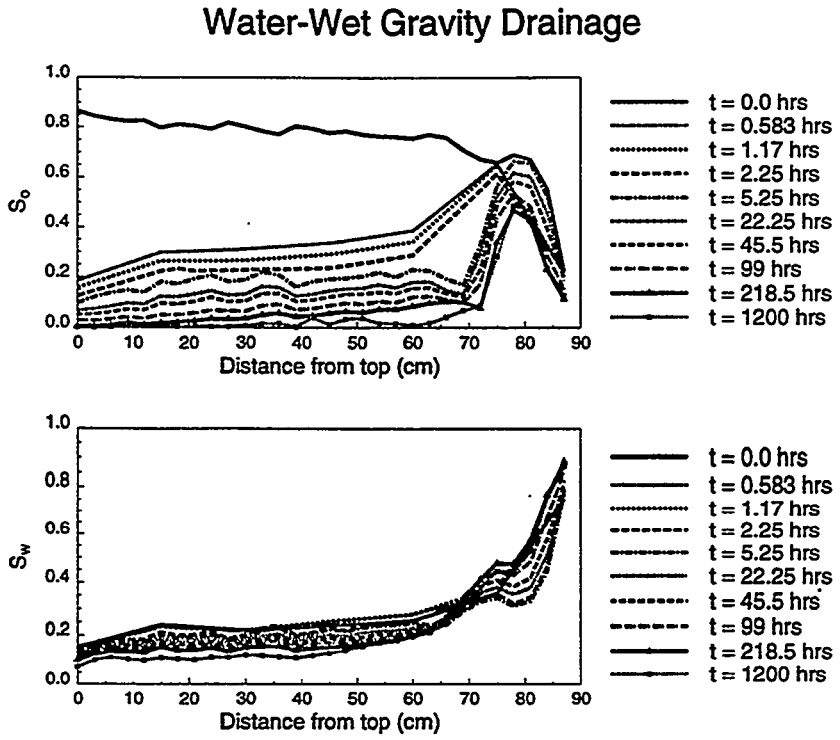

Figure 3.1: Oil and water saturation profiles versus time during gravity drainage. The sand was water-wet and the initial condition was connate water saturation S_{wc}. Oil and water permeabilities can be calculated directly from the measured distributions.

We obtained these capillary pressure-saturation curves from analog experiments performed on exactly the same type of packing with the same fluids. The fluids are left to drain for at least three weeks until capillary/gravity equilibrium is reached. Then the sand is removed from the pack in 3 cm increments and the pore fluids are dissolved in isoproponal and run through a gas chromatograph (GC). The GC provides an exceptionally accurate and sensitive measurement of saturation. From the measured saturation distribution, the oil/water, gas/oil and gas/water capillary pressures can be inferred [54], and the relative permeabilities obtained.

In practice this method has difficulties for column positions near and below the capillary fringe as the quantity dS_i/dz is large, and the capillary pressure gradient is very close to the gravational gradient, thus any small errors in saturation measurement correspond to large errors in the measured permeability. Near the top of the column the saturation is roughly constant with position, so $dS_i/dz \approx 0$ and the capillary pressure term can be ignored for positions over a region were the saturation data satisfies the above condition (between 20 and 50 cm in Fig. 3.1). This was done for the oil-wet and fractionally-wet cases where only data between 10 and 30 cm from the top of the chamber was used in the calculation. In essence, the CT allows us to avoid capillary end effects in the determination of relative permeability, as we can choose a section over which the capillary pressure gradients are negligible compared to gravity. For the water-wet case, the results were analyzed with and without capillary pressure data with similar results [55]. The water-wet data we show includes the capillary pressure correction.

3.2.2 Gas Permeability

We have developed a procedure to measure directly the gas relative permeability in the sand packs. The sand is packed into a 60 cm column made out of 20 separate 3 cm long sections of polycarbonate plastic tubing (2.54 cm diameter) which are held together with shrink tubing. Nine of the plastic sections in the column contain a small port through which the pressure of the

Table 3.2: Drainage experiments from which oil and water relative permeabilities were obtained. The figure column shows where the data is displayed. The initial condition before drainage was either waterflood residual (S_{or}) or connate water (S_{wc}).

Expt. Number	Figure(s)	Oil Phase	Porous Medium	Initial Condition
1	1,2,3,8	octane	water-wet sand	S_{wc}
2	2	octane	water-wet sand	S_{or}
4	3	hexane	water-wet sand	S_{wc}
5	3,8	decane	water-wet sand	S_{wc}
6	3	octane	water-wet sandstone	S_{or}
7	2,8	octane	oil-wet sand	S_{or}
8	2	octane	oil-wet sand	S_{wc}
9	2	octane	fractionally-wet sand	S_{or}
10	2	octane	fractionally-wet sand	S_{wc}

gas phase can be measured. Thus we can measure eight separate pressure drops along the column during gas flow.

We first measure the single phase gas permeability by flowing known rates of CO_2 through the column and measuring the pressure drops across each section using a manometer. For two-phase measurements, the column is then filled with de-gassed water from below and the water is circulated until all of the original CO_2 is displaced or dissolved. The column is then allowed to drain under gravity for about 1 hour, after which gas is injected at a known rate at the top of the column, displacing additional water out the bottom. This injection is continued for several hours until the pressures have stabilized and the gas and water phases are in equilibrium. Due to capillary effects, the distribution of water varies along the sand pack, with a high water saturation (and low gas saturation) near the outlet and a low water saturation (and high gas saturation) near the inlet. The pressure drop is measured between each section, which in turn gives the gas relative permeability. The column is sectioned and the water and gas saturations are obtained gravimetrically.

For three-phase measurments a nearly identical procedure is used. The only differences are 1) the column is first filled with the most-wetting fluid, and then brought to connate water saturation (S_{wc}) by displacing the water with oil before the gas is allowed to enter; and 2) the oil, water, and gas saturations are measured using the GC rather than gravimetrically.

3.3 Results

We performed experiments with media of different wettabilities and different oils (hexane, octame, decane) which differ in spreading coefficient. Table 3.2 lists all the experiments and the figures which display the data. Figure 3.2 shows the measured relative permeabilities for oil and water for the water-wet ($f = 0$), fractionally-wet ($f = 0.5$), and oil-wet ($f = 1$) sandpacks with octane as the oil. The open symbols are from the initial condition of S_{or} while the closed symbols are from drainages that started from initial condition S_{wc}. Note that we can measure saturations as low as $S = 0.01$, with relative permeabilities spanning over six orders of magnitude. The observed scatter in the data is related more to to the uncertainty in the capillary pressure rather than the uncertainty in the measured saturations.

Figure 3.3 shows the measured oil relative permeability for hexane, octane, and decane in water-wet sand, and for octane in a water-wet consolidated sandstone.

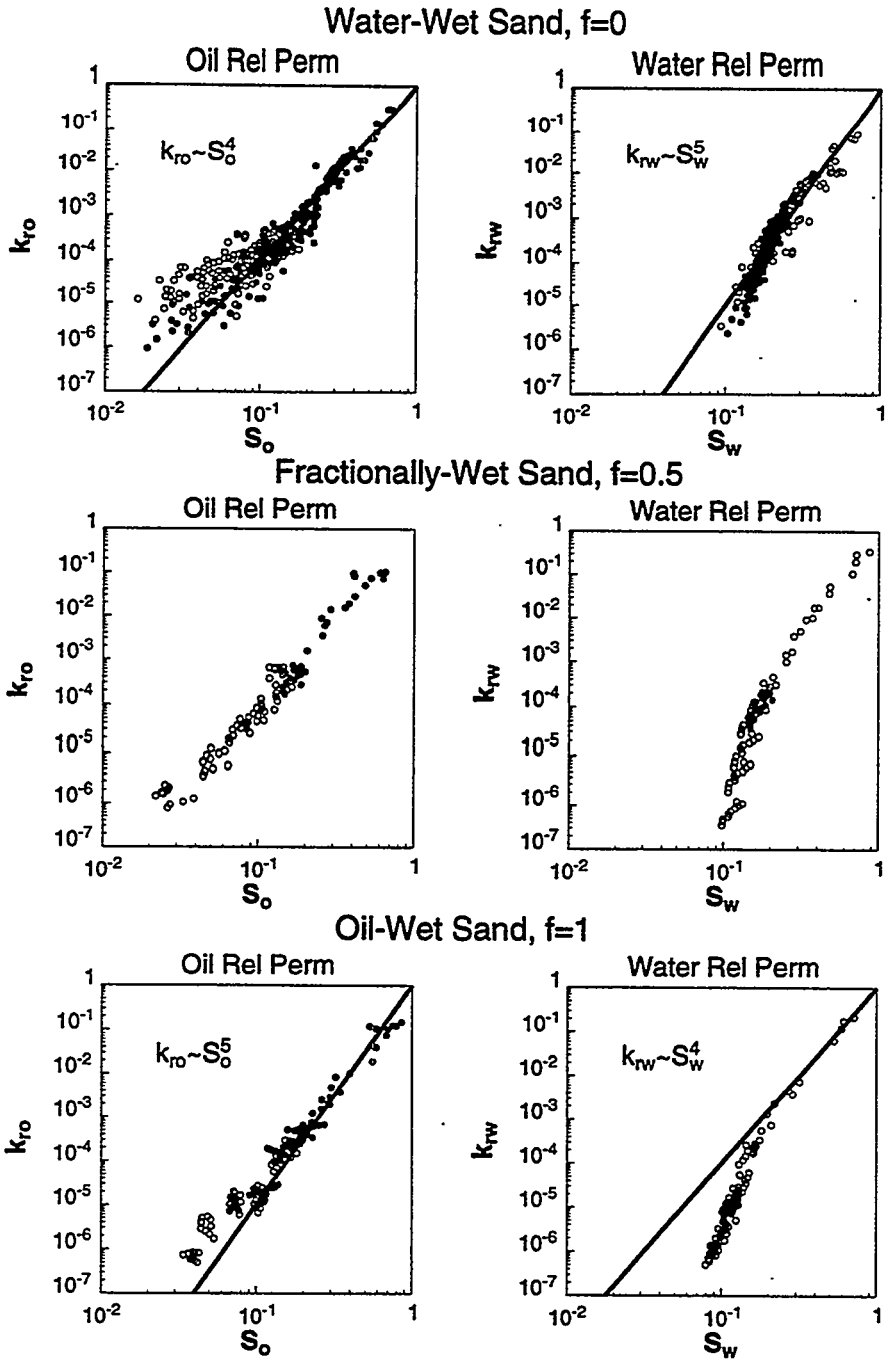

Figure 3.2: Measured oil and water relative permeabilities with n-octane as the oil for water-wet ($f = 0$), fractionally-wet ($f = 0.5$), and oil-wet ($f = 1$) sand during three-phase gravity drainage. Open symbols are drainages which started from residual oil saturation (S_{or}), and closed symbols are drainages which started from connate water saturation (S_{wc}). The solid lines are fits to the data at high saturations.

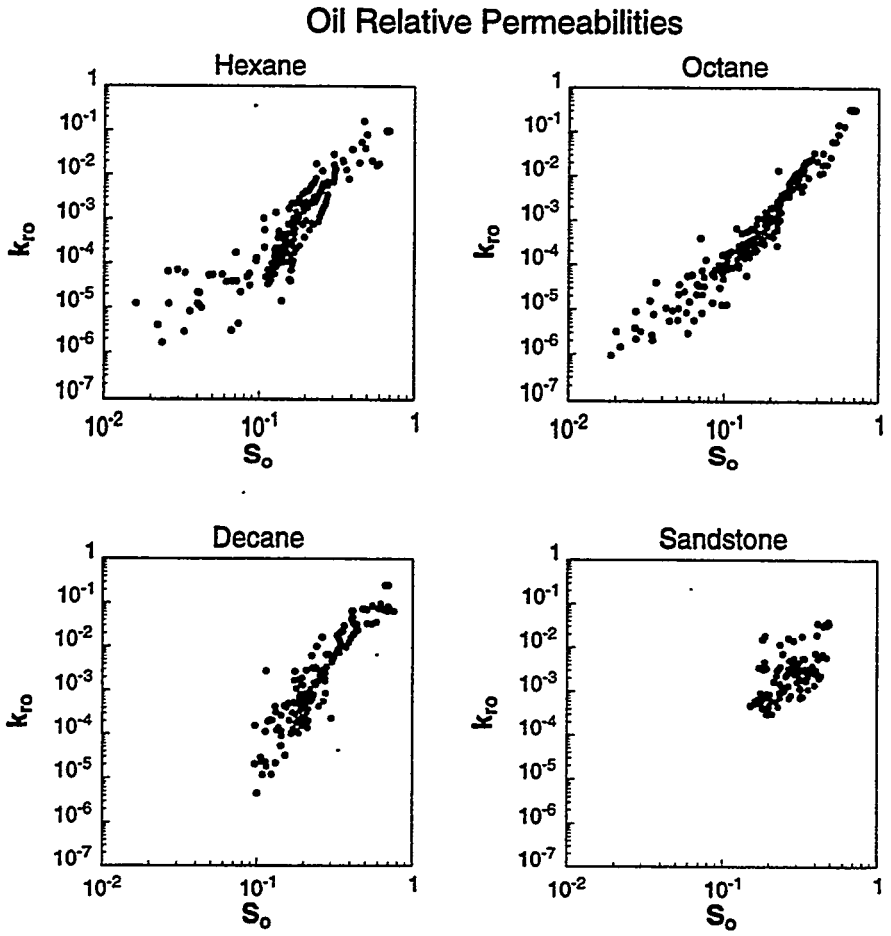

Figure 3.3: Measured oil and water relative permeabilities with hexane, octane, and decane as the oil in water-wet ($f = 0$) sand and with octane in water-wet sandstone during three-phase gravity drainage.

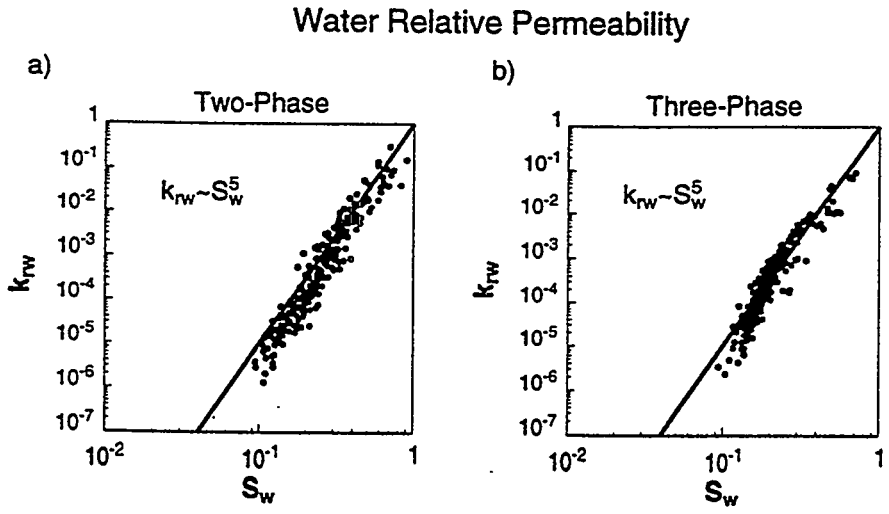

Figure 3.4: Measured water relative permeabilities for a) the two-phase (gas/water) system and for b) the three-phase (gas/oil/water) system from gravity drainages in water-wet ($f = 0$) sand.

Figure 3.4 shows the measured water relative permeability for two-phase (gas/water) and three-phase drainages in water-wet sand.

Figure 3.5 shows the measured gas relative permeabilities for a) the two-phase gas/water system for different wettabilities and the two-phase gas/oil system for oil-wet media, and for b) the three-phase system for water-wet and oil-wet media. Notice that for the gas permeability the plots are on linear axes.

The following features are observed in the measured relative permeabilities:

1. To within experimental error, the oil and water relative permeabilities during three-phase drainage are independent of initial condition.

2. The three-phase relative permeabilties of the most wetting fluid (water in water-wet media, oil in oil-wet media) and the two-phase water relative permeability in water-wet media are similar for the whole saturation range. All can be well described by a simple power law $k_r \sim S^\alpha$, where $\alpha \approx 5$. For the most wetting fluid the permeability is the same for two and three phase displacements. However, a lower saturation is reached in the oil-wet medium than in the water-wet medium.

3. At high saturations, $S > S_{or}$ (S_{wc}), the permeabilities of oil in water-wet media and water in oil-wet media are similar. Both can be well described by a simple power law $k_r \sim S^\alpha$, where $\alpha \approx 4$.

4. At low saturations, $S < S_{or}$ (S_{wc}), the permeabilities of oil in water-wet media and water in oil-wet media are very different. For hexane and octane, the oil relative permeability remains finite at low saturations with a power law of $k_r \sim S^\alpha$, where $\alpha \approx 2$. The water relative permeability drops off quickly, tending to zero at water saturations of $S_w \approx 0.1$.

5. When water is the main liquid phase, the gas relative permeability for the oil-wet medium is roughly a factor of two smaller than that for an identical water-wet medium. When oil is the main liquid phase, the gas relative permeability is independent of the wettability.

6. For the fractionally-wet sand, the oil, water and gas relative permeabilities are between the oil, water and gas relative permeabilities in the water-wet and oil-wet sands.

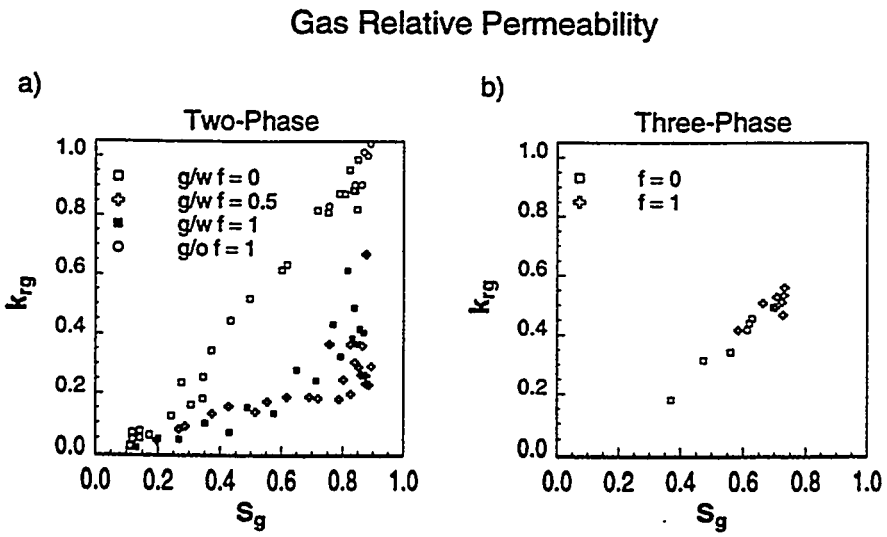

Figure 3.5: Measured gas relative permeabilities for a) the two-phase gas/water system for media of varying wettability ($f = 0, 0.5, 1$) and the two-phase gas/oil system for oil-wet media ($f = 1$), and for b) the three-phase gas/oil/water system for water-wet ($f = 0$) and oil-wet ($f = 1$) media. The gas relative permeability in oil-wet sand is roughly a factor of two smaller than that for identical water-wet sand when water is the other phase.

Although exact functional forms of relative permeabilites are very dependent on the specific porous media, we believe that many of the above features are universal for three-phase displacements. We attempt to discern this by considering the effects of pore scale configuration on the relative permeabilities.

3.4 Pore Scale Explanation

All the features listed above can be understood qualitatively by considering the pore scale configuration of fluids. We discuss each observation in turn.

1. The oil and water relative permeabilities are independent of initial condition during three-phase drainage.

In water-wet media, the water occupies the smallest pores, regardless of the saturations of oil and gas. Thus in a drainage-type experiment with the water saturation decreasing, it is expected that the relative pemreability of water is insensitve to initial condition. This behavior has been seen by other researchers [42, 44]. Oil, however, occupies the intermediate sized pores, and its pore occupancy does depend on the saturations of both water and gas: in a gas/oil displacement, oil occupies the smaller pores, whereas for an oil/water displacement, oil occupies the larger pores. Reviews of the literature have shown that the oil relative permeability is slightly sensitive to initial condition [42, 44]. We do not see this, and the oil relative permeability appears to be a function only of its own saturation. This could be due to the narrow pore size distribution of the sandpacks, and is consistent with other results in uniform media [28, 42]. Similarly, for water in oil-wet media, we see no sensitivity to inital condition, although the water is no longer the wetting phase.

2. Similarity of the relative permeability of the most wetting phase in water-wet and oil-wet media.

The most wetting phase occupies the smallest pores, and corners, grooves, and crevices in the wider pores. If we compare strongly and uniformally water-wet and oil-wet media, we would expect the configuration of the most wetting fluid to be similar for both systems at the same saturation. The exact functional form of the relative permeability depends on the porous medium and is not universal. The only general feature is that k_r should asymptote to a zero connate saturation, indicating that the wetting phase remains connected, albeit poorly, through wetting layers in crevices of the medium down to very low saturation.

In the experiments, the lowest wetting phase saturation observed depends on the largest capillary pressure reached – it takes an infinite capillary pressure to reach zero saturation. In the water-wet medium, the gas/water capillary pressure at the top of the column at the end of the experiment is

$$P_{cgw} = (\rho_w - \rho_g)gh, \tag{3.4}$$

where h is the height of the column (67 cm for our column), assuming capillary/gravity equilibrium, and $P_{cgw} = 0$ at the bottom of the pack.

From the Young-Laplace equation

$$P_{cgw} = \frac{2\gamma_{gw}}{r_{gw}}, \tag{3.5}$$

where r_{gw} is the mean radius of curvature of the gas/water interface. Hence

$$r_{gw} = \frac{2\gamma_{gw}}{(\rho_w - \rho_g)gh} \approx 21\mu\text{m} \tag{3.6}$$

for our experiments.

Using the same argument for the oil-wet case, the largest gas/oil (octane) capillary pressure gives

$$r_{go} = \frac{2\gamma_{go}}{(\rho_o - \rho_g)gh} \approx 9\mu\text{m}, \tag{3.7}$$

and

$$\frac{r_{gw}}{r_{go}} = \frac{\gamma_{gw}(\rho_o - \rho_g)}{\gamma_{go}(\rho_w - \rho_g)} \approx 2.3. \tag{3.8}$$

The wetting phase resides in regions of the pore space with a mean entry curvature smaller than r_{gw} or r_{go}. That r_{gw} is over two times larger than r_{go} explains why in our experiments the lowest water saturation reached in the water-wet pack ($S_w \approx 0.1$) is higher than that reached in the oil-wet pack ($S_o \approx 0.04$) – see Fig. 1.

3. Similarity of k_{ro} in the water-wet pack to k_{rw} in the oil-wet pack for high saturation.

Network modeling studies indicate that the relative permeability of a phase at high saturation is controlled by the connectivity of pores filled with that phase [16]. In the water-wet systems, oil is not the most wetting phase and is displaced by gas. Similarly in oil-wet systems, water is not the most wetting phase and is also displaced by gas. Thus the arrangement of oil-filled pores in a water-wet medium, and of water-filled pores in a oil-wet medium are, to a good approximation, similar. However, the CT experiments are not sufficiently sensitive to compare the oil and water relative permeabilities accurately at high oil and water saturations.

The actual functional form observed – $k_r \sim S^4$ – is a function of the pore size distribution and would be different for different media. However, it is noteworthy that the use of a quartic form to describe k_{ro} in three-phase flow was first proposed by Corey et al. [41] and is also consistent with the results from three-phase network models [16].

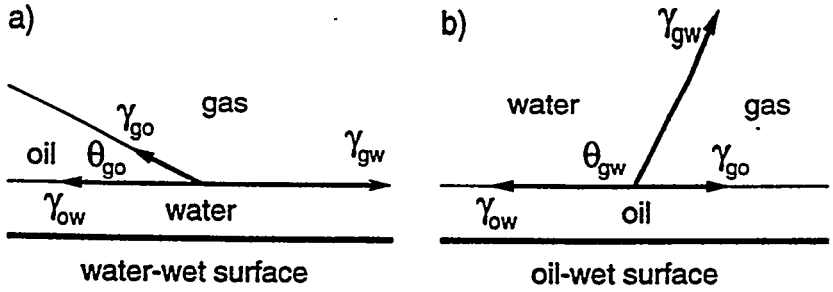

Figure 3.6: Configuration of fluids on : a) a flat water-wet surface, b) a flat oil-wet surface.

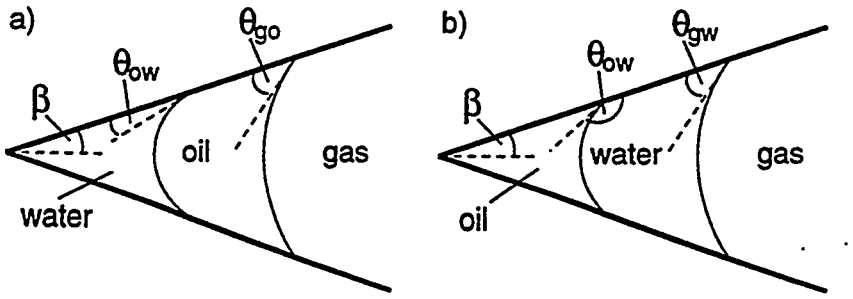

Figure 3.7: Possible configuration of fluids in a pore space corner of half-angle β: a) water-wet surfaces, b) oil-wet surfaces. Note that configuration b) is not allowed as $\theta_{gw} > 90°$.

4. Very different forms for k_{ro} in water-wet media and k_{rw} in oil-wet media at low saturation.

At low saturation phases may remain connected through wetting layers in crevices in the pore space. It is this connectivity which controls k_r at low saturation. The pore scale configuration and connectivity of oil and water is very different for water-wet and oil-wet media. Consider first flat water-wet and oil-wet surfaces as shown in Figure 3.6.

The most wetting fluid coats the surface. The contact angle between oil or water and gas, which will control the position of the phase in the pore space, is given by the balance of interfacial tensions, assuming that the solid is coated with a thick wetting film.

For oil in water-wet media, (Fig. 3.6a)

$$\cos\theta_{go} = \frac{\gamma_{gw} - \gamma_{ow}}{\gamma_{go}} = 1 + \frac{C_{so}}{\gamma_{go}}, \tag{3.9}$$

where

$$C_{so} = \gamma_{gw} - \gamma_{ow} - \gamma_{go} \tag{3.10}$$

is the spreading coefficient for oil. In thermodynamic equilibrium $C_{so} \leq 0$ [49]. Using our data for octane we find $C_{so} = -0.3$ mN/m and $\theta_{go} \approx 10°$.

Now imagine the three fluids in a corner of the pore space as shown in Fig. 3.7a. If $\theta_{ow} + \beta < 90°$ and $\theta_{go} + \beta < 90°$, where β is the half-angle of the corner, then a layer of oil may be present [16, 12]. These layers are on the order of micrometers thick and have been observed in micromodel experiments [10, 9, 8]. Drainage through oil layers is the mechanism by which very

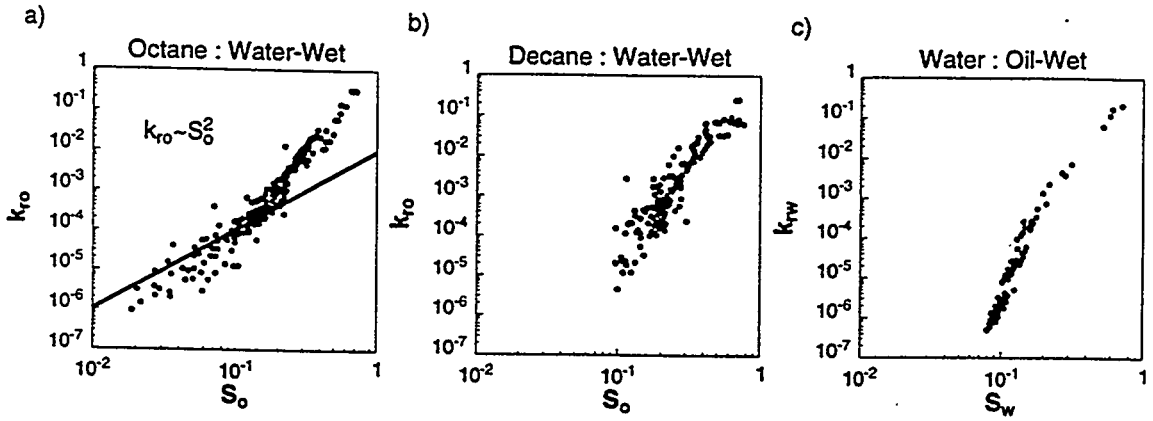

Figure 3.8: Comparison of relative permeabilities. a) A spreading system ($\theta_{go} \approx 0$) : Octane in water-wet sand. b) A non-spreading system : Decane in water-wet sand. c) A non-wetting system : Water in oil-wet sand.

low oil saturations are reached during gas displacement in water-wet media [1, 2, 4]. Final oil saturations as low as $S_o = 0.001$ have been reached [4]. For a system with $\theta_{ow} = \theta_{go} = 0$, the oil layers can drain to infinitesimal thickness at a *finite* gas/oil capillary pressure, meaning that in theory, $S_o = 0$ can be achieved through gravity drainage [5, 4]. In our experiments the lowest saturation obtained is $S_o \approx 0.01$ after 7 weeks of drainage.

Displacement of oil below the waterflood residual oil saturation, S_{or}, requires layer drainage. In our experiments, and others on bead packs, sandpacks and consolidated sandstones a characteristic layer drainage regime with $k_{ro} \sim S_o^2$ has been observed for $S_o < S_{or}$ (see Fig 3.3 and Fig. 3.8a) [54, 25, 28]. This is readily explained by examining the flow in a single angular pore (see Fig. 3.7a). S_o is proportional to the area of the oil in the layer. The oil conductance for Poiseuille type flow is proportional to the area squared, leading to $k_{ro} \sim S_o^2$ [16, 13]. This may seem a simple argument, but it is confirmed by more detailed analysis of layer flow that has been verified against numerical solutions of the Navier Stokes equation and experiments in square capillary tubes [13].

We observe layer drainage for a spreading system – loosely defined as one with $C_{so} \approx 0$, or $\theta_{go} \approx 0$. However, the situation is different for oils with a large and negative spreading coefficient.

For decane in water-wet media, our measurements of interfacial tension result in $\theta_{go} \approx 30°$. Decane layers have been seen in micromodels [8]. However, decane layers cannot form in oblique wedges ($\beta > 60°$), and are present for a more restricted range of capillary pressures than for octane [16]. If oil layers are not present, oil can be trapped, leaving a residual saturation at the end of drainage. In our experiments we do not observe a layer drainage regime, as shown in Fig. 3.8b.

For water in oil-wet media, (Fig. 3.6b)

$$\cos\theta_{gw} = \frac{\gamma_{go} - \gamma_{ow}}{\gamma_{gw}} = 1 + \frac{C_{sw}}{\gamma_{gw}}, \tag{3.11}$$

where

$$C_{sw} = \gamma_{go} - \gamma_{ow} - \gamma_{gw} \tag{3.12}$$

is the spreading coefficient for water. Using Table 3.1 we find $C_{sw} = -102.1$ mN/m and $\theta_{gw} \approx 115°$. Since $\theta_{gw} > 90°$, water is less wetting than gas. In Fig. 3.7b, water layers can occur for $\theta_{gw} + \beta < 90°$, and gas layers can occur for $90° + \beta < \theta_{gw}$, neither of which are possible except for gas in

exceptionally sharp crevices. The absence of a layer drainage regime is evident in Fig. 3.8c. Note that k_{ro} for decane in a water-wet system is similar to k_{rw} in an oil-wet system. Both represent cases where the intermediate-wet fluid is non-spreading and there is no layer drainage regime.

Note that we do not observe the same layer drainage regime for the most wetting phase – instead of $k_r \sim S^2$, we observe $k_r \sim S^5$. The most wetting phase occupies the small pores and all the narrow nooks and crannies, which may be poorly connected. In contrast, oil layers in spreading systems reside over the water, and by construction therefore, are well connected throughout the porous medium.

5. When water is the main liquid phase, k_{rg} is lower in an oil-wet medium than in a water-wet medium.

For the two-phase gas/water system in water-wet media, the water phase will occupy the smallest pores and crevices while the gas phase occupies the large pore spaces. In oil-wet media, the contact angle is such that neither the water phase nor the gas phase wets the pore surfaces and thus the water and gas phases compete for the largest pores. Thus at equivalent gas saturations, in the oil-wet system the gas is in smaller pathways leading to a lower permeability.

For the three-phase gas/oil/water system in water-wet media, the gas is non-wetting to both oil and water, and so k_{rg} is expected to be a function only of gas saturation. In oil-wet media, gas is non-wetting to oil, but is not strongly non-wetting to water. Thus it is expected that in this case k_{rg} depends on both the oil and water saturations. From Fig. 3.5b we see that the three-phase k_{rg} in the oil-wet system is between the two-phase gas/water k_{rg} and gas/oil k_{rg}. Most three-phase models [57, 44, 42] assume that gas is always the non-wetting phase and is a function of gas saturation only.

We also see that the three-phase k_{rg} in the water-wet system is lower than the water-wet gas/water k_{rg} and gas/oil k_{rg}, while as gas is the most non-wetting phase we expect the gas relative permeabilities to be similar. The cause of this decrease is currently unknown.

6. The fractionally-wet sand has behavior intermediate between oil-wet and water-wet sand.

This last observation seems intuitively obvious. However, there are three important points to make. First, the oil in a spreading system is always connected regardless of f, since it can reside in corners as the most wetting phase or in layers as the intermediate wetting phase. Consistent with this is the observation that k_{ro} asymptotes to zero residual oil saturation, for *any* f, as shown in Fig. 3.2. However, unless $f = 0$, an infinite capillary pressure is required to achieve this. Second, note that the trapped water saturation for $f = 0.5$ is slightly *higher* than for $f = 1$. This is because for $f = 0.5$, the oil-wet regions are poorly connected in the pack leading to significant trapping of water. This percolation-type argument has been explored in more detail by Zhou et al. [58]. Third, the gas relative permeability for $f = 0.5$ is very close to the oil-wet case. This shows that the gas mobility is significantly affected even if a fraction of the pores are oil-wet.

3.5 Discussion

We have performed a series of conceptually simple three-phase experiments, which we can interpret by analyzing the fluid arrangement at the pore scale. However, the full range of behavior of three-phase flow has not been studied. In particular, in our experiments the gas saturation increased while the oil and water saturations decreased. We did not study water injection, or WAG cycles of water and gas flooding. For these cases the relative permeabilities are very likely to be significantly different [56, 52, 16]. Furthermore, we studied media with idealized wettability

variations. We did not study more realistic situations where the wettability changes are induced by the contact of oil with the solid after primary drainage. Nor did we consider geologically complex media with varying minearologies and microporosity. Nevertheless, the ability to interpret simple cases is reassuring, and gives a basis for the fundamental understanding of three-phase flow in more realistic reservoir and vadose zone settings.

3.6 Conclusions

We have used CT scanning and analogue experiments to measure directly oil, water and gas relative permeabilities during three-phase gravity drainage. Experiments were performed on oil-wet, water-wet, and fractionally-wet sandpacks, achieving data down to saturations as low as $S_o = 0.01$ and relative permeabilities that span six orders of magnitude. An analysis of the data leads to the following general conclusions for three-phase gravity displacements:

1. At low oil saturations ($S_o < S_{or}$) in water-wet media, spreading systems show a characteristic form of the oil relative permeability, $k_{ro} \sim {S_o}^2$. This is consistent with a theoretical interpretation of oil layer drainage at the pore scale. For a non-spreading decane system, the layer drainage regime was not observed.

2. In oil-wet media, the oil relative permeability behaves similarly to the water relative permeability in water-wet systems.

3. In oil-wet media, the water has a large and negative spreading coefficient, meaning that water layers do not form in the pore space. The water relative pemeability k_{rw} for an oil-wet medium is similar to k_{ro} for a water-wet medium and a non-spreading oil.

4. In oil-wet media, the gas relative permeability is roughly a factor of two smaller than that for identical water-wet media. This is consistent with the gas and water phases competing for the largest pores in oil-wet media, and the gas not necessarily being the non-wetting phase. This has implications in the creation of three-phase relative permeability models.

The data for all our experiments is available on our web site:
http://ekofisk.stanford.edu/supric.html/ .

3.7 Nomenclature

C_{so} = spreading coefficient of oil
C_{sw} = spreading coefficient of water
f = fraction of oil-wet sand
g = gravitational constant
k_{ri} = relative permeability to phase i
r_{gw} = radius of curvature of the gas/water interface
r_{go} = radius of curvature of the gas/oil interface
P_i = pressure of phase i
P_{cgw} = gas/water capillary pressure
S_i = saturation of phase i
S_{or} = waterflood residual oil saturation
S_{wc} = connate water saturation

Greek Letters

α = power law exponent
β = half angle of pore corner
γ_{ow} = oil/water interfacial tension
γ_{go} = gas/oil interfacial tension
γ_{gw} = gas/water interfacial tension
ρ_i = density of fluid i
θ_{ow} = oil/water contact angle
θ_{go} = gas/oil contact angle
θ_{gw} = gas/water contact angle

Subscripts

i = phase
g = gas
o = oil
w = water (brine)

4. Calculation of Minimum Miscibility Pressure

Yun Wang and Franklin M. Orr, Jr.

4.1 Abstract

We describe and test a method for calculation of minimum miscibility pressure (MMP) that makes use of an analytical theory for one-dimensional, dispersion-free flow of multicomponent mixtures. The theory shows that in a displacement of an oil by a gas with n_c components, the behavior of the displacement is controlled by a sequence of $n_c - 1$ key tie lines. Besides the tie lines that extend through the initial oil and injection gas compositions, there are $n_c - 3$ tie lines, known as *crossover tie lines*, that can be found from a set of conditions that requires the extensions of the appropriate tie lines to intersect each other. The MMP is calculated as the pressure at which one of the key tie lines becomes a critical tie line (a tie line of zero length that is tangent to the critical locus). We describe the numerical approach for solving the tie line intersection equations, and we use slim tube test and compositional simulation data reported in the literature to show that the proposed approach can be used to calculate MMP accurately for displacements with an arbitrary number of components present.

4.2 Introduction

Design of a multicontact miscible gas injection project requires knowledge of the minimum miscibility pressure (or minimum gas enrichment), the pressure (or enrichment) above which high pressure gas displaces nearly 100% of oil in the swept zone. In this chapter we examine methods for calculating the MMP from an equation-of-state based representation of phase behavior for mixtures of the oil displaced with the injected gas.

The earliest attempts to calculate MMPs were based on ternary theory for multicontact miscible displacement ([59]). For example Benham [60] constructed approximate ternary diagrams and used extensions of critical tie lines to estimate minimum enrichments for condensing gas drive systems. Metcalfe *et al.* [61] described a method for condensing gas drives based on multiple equilibrium mixing cells. In that method, a sort of simplified finite difference compositional simulation, gas was mixed with oil in the first cell and flashed. Liquid and vapor in excess of the cell volume were moved downstream to the next cell, and the process repeated. The MMP was determined as the pressure required to produce near-critical mixtures in downstream cells. Kuo [62] used a single cell version of the mixing cell approach, again for condensing gas drives. In his method, gas was mixed with oil and flashed. The resulting vapor was removed and fresh injection gas added to the liquid in the cell (sometimes called reverse contacts), and the flash calculation was repeated. The mixing process was then repeated until the liquid phase composition converged. If it converged to a critical mixture (vapor and liquid identical), the system was taken to be miscible. If not the pressure was incremented and the process repeated to find the MMP. Luks *et al.* [63] used a similar technique for both condensing and vaporizing drives. For vaporizing gas drives, vapor from each flash was mixed with fresh oil (forward contacts). Both forward and reverse contacts were performed, and the MMP was taken to be the lower of the pressures required to produce a critical mixture by repeated contacts.

[2]The material in this chapter was presented at the 1998 SPE/DOE Improved Oil Recovery Symposium in Tulsa, Oklahoma, April 19-22, 1998, and is published as SPE paper 39683 in the conference proceedings.

Nouar and Flock [64] used the properties of ternary systems in a different way. They calculated critical compositions and tie line slopes directly (for ternary systems only) and used them to estimate MMP for vaporizing gas drive systems. The MMP was taken to be the pressure at which the oil composition was intersected by the extension of the critical tie line. Systems with more than three components were handled by correlating calculated ternary MMPs with variable molecular weight for the intermediate and heavy hydrocarbon components.

Thus, the behavior of ternary systems is well understood. The MMP can be determined by finding the pressure at which the oil composition (for a vaporizing gas drive), or the injected gas composition (for a condensing gas drive), is located on the extension of a critical tie line. That tie line can be found directly by one of the mixing cell methods or by performing negative flash calculations (Whitson and Michelsen [65], Wang and Orr [66]).

It is now known, however, that extension of these ideas to systems with more than three components requires additional understanding. Zick [67] showed that multicomponent displacements can display features of both condensing and vaporizing drives. He also showed that the MMP could be estimated by one-dimensional compositional simulation, provided sufficient care was taken to account for the effects of numerical dispersion. A subsequent paper by Stalkup [68] confirmed Zick's results and outlined a procedure for extrapolation of the number of grid blocks to eliminate effects of numerical dispersion. The papers by Zick and Stalkup demonstrate clearly that the MMP can always be found by compositional simulation, though fine grids and repeated simulations at multiple pressures will mean that significant computation times will be required.

Jensen and Michelsen [69] continued the investigation of the ideas of critical tie lines from ternary systems. They showed that for systems with more than three components, the pressures required to force critical tie lines to extend through the injection gas composition or the oil composition do not necessarily indicate the correct MMP. They advocated use of a mixing cell approach instead. (We will show below that the single cell technique can also lead to inaccurate MMPs for that system.) Given the speed and simplicity of single cell methods, investigations of their properties have continued ([70]), and multicell methods have also been examined ([71]).

The reason for the inaccuracies encountered in the critical tie line and single cell methods became apparent when analytical solutions were obtained for one-dimensional, dispersion-free flow of four-component mixtures. Monroe *et al.* [72] showed that three key tie lines control displacement behavior in four-component systems: the tie line that extends through injection gas composition, the tie line that extends through the oil composition, and a third tie line called "the crossover tie line". Orr *et al.* [73] then showed that multicontact miscibility develops if any of the three key tie lines is a critical tie line. In many displacements, it is the crossover tie line that approaches the critical locus at the lowest pressure, and in such cases that tie line determines the MMP. Johns *et al.* [74] then showed that the condensing/vaporizing mechanism described by Zick [67] arises when a crossover tie line controls development of miscibility. Hence, methods that identify only the critical tie lines associated with the injection gas or the initial oil are doomed to failure for condensing/vaporizing systems.

The analytical approach was used by Dindoruk *et al.* [75] to study MMP behavior of N_2 systems, and the application to systems with more than four components was considered by Johns and Orr [76]. In systems with n_c components, there are n_c - 3 crossover tie lines, and the initial oil and injection gas tie lines are also still important. (In certain special cases, a degenerate solution can occur when two key tie lines coincide and the system is described by n_c - 2 key tie lines. We give an example below.) Johns and Orr considered only a single-component injection gas (CO_2). They made use of the fact that in many cases, the crossover tie lines can be found from a geometric construction that arises from the properties of shocks in the analytical solutions ([74]) (when two tie lines are connected by a shock, their extensions must intersect). For example, Fig. 4.1 shows a four component system (methane carbon dioxide, butane and decane) in which all key tie lines

are connected by shocks. The crossover tie line is the only tie line in the interior of the quaternary diagram that (when extended at both ends) intersects the extensions of the tie lines that extend through injection gas and initial oil compositions. Wang and Orr [66] showed how to solve the tie-line intersection equations efficiently for a single-component injection gas displacing an oil with an arbitrary number of components. They also considered displacement by a two-component gas, but only for four-component systems.

In this chapter we extend the work of Johns and Orr [76] and Wang and Orr [66] to systems with an arbitrary number of components in either the initial oil or the injection gas. We begin with a description of the tie line intersection approach and then we report results of a series of tests of the accuracy of the technique.

4.3 Mathematical Approach

Johns *et al.* [74] showed, based on their analytical solutions, that if any two tie lines are connected by a shock, the extensions of the tie lines must intersect (see Wang and Orr [66] for a discussion of self-sharpening composition variations that produce shocks and spreading composition variations, sometimes called rarefactions, that do not). For displacements in which all the tie lines are connected by shocks, then, the $n_c - 1$ key tie lines can be found rigorously as follows. The initial oil and injection gas tie lines are found using the negative flash of Whitson and Michelsen [65] or the modified negative flash of Wang and Orr [66]. The $n_c - 3$ crossover tie lines are then found from the conditions that each crossover tie line intersects the tie line just upstream and the tie line just downstream. Once the key tie lines have been found at a given pressure, the MMP can be determined by increasing the pressure in increments until one of the key tie lines becomes a critical tie line. This approach is completely rigorous if the displacement system is fully self-sharpening (see Wang and Orr [66] for a discussion of how self-sharpening behavior is detected). If the displacement path contains one or more continuous variations between tie lines (rarefactions) then the tie lines obtained by the intersection method are an approximation to the actual key tie lines, but all evidence obtained to date indicates that the approximation is a very good one (see Wang and Orr [66]). Thus, the tie line intersection method can be used to estimate MMPs, whether or not the displacement system is fully self-sharpening, and the calculated MMPs will be accurate if the characterization of the gas/oil system gives an accurate representation of phase behavior in the neighborhood of the critical locus.

Any pair of tie lines that intersect must satisfy

$$x_j^n \left[1 + (K_j^n - 1)V_n^n\right] = x_j^{n+1} \left[1 + (K_j^{n+1} - 1)V_n^{n+1}\right], \tag{4.1}$$

where $n = 1, n_c - 2; j = 1, n_c - 1$.

In Eqs. 4.1, x_j^n is the liquid phase mole fraction for component j on tie line n, K_j^n is the equilibrium K-value for component j on tie line n , V_n^n is the vapor phase mole fraction on tie line n of the intersection point between tie line n and tie line $n+1$ and V_n^{n+1} is the vapor phase mole fraction on tie line $n+1$ of the intersection point between tie line n and tie line $n+1$. In Eqs. 4.1, the initial oil tie line and the injection gas tie lines are known. They can be obtained by performing negative flashes for the initial oil and injection gas compositions. Elimination of vapor phase mole fractions from Eqs. 4.1 leaves liquid phase compositions as unknowns. If there is no component missing across two intersecting tie lines, the vapor phase mole fractions in Eqs. 4.1 are

$$V_n^n = \frac{a_1^n - a_2^n}{b_1 - b_2}, \tag{4.2}$$

and

$$V_n^{n+1} = \frac{a_1^{n+1} - a_2^{n+1}}{b_1 - b_2}, \tag{4.3}$$

where

$$a_1^n = (x_1^{n+1} - x_1^n)x_2^{n+1}(K_2^{n+1} - 1), \tag{4.4}$$

$$a_1^{n+1} = (x_1^{n+1} - x_1^n)x_2^n(K_2^n - 1), \tag{4.5}$$

$$a_2^n = (x_2^{n+1} - x_2^n)x_1^{n+1}(K_1^{n+1} - 1), \tag{4.6}$$

$$a_2^{n+1} = (x_2^{n+1} - x_2^n)x_1^n(K_1^n - 1), \tag{4.7}$$

$$b_1 = x_2^{n+1}x_1^n(K_2^{n+1} - 1)(K_1^n - 1), \tag{4.8}$$

and

$$b_2 = x_1^{n+1}x_2^n(K_1^{n+1} - 1)(K_2^n - 1). \tag{4.9}$$

If there is one component missing on one of the two intersecting tie lines, the vapor mole fractions in Eqs. 4.1 are

$$V_n^n = \frac{1}{1 - K_{n+1}^n} \tag{4.10}$$

and

$$V_n^{n+1} = \frac{1}{K_1^{n+1} - 1}\left[\frac{x_1^n}{x_1^{n+1}}\left(\frac{K_1^n - K_{n+1}^n}{1 - K_{n+1}^n}\right) - 1\right] \tag{4.11}$$

Substitution of vapor mole fractions given by Eqs. 4.2 and 4.3 or by Eqs. 4.10 and 4.11 into Eqs. 4.1, along with the constraint that liquid and vapor phase mole fractions must sum to one,

$$\sum_{i=1}^{n_c-1}(K_i^n - K_{n_c}^n)x_i^n = (1 - K_{n_c}^n) \tag{4.12}$$

gives a system of nonlinear equations that can be solved to find the intersecting tie lines.

The tie lines obtained by solution of the intersection equations can then be tested for closeness to the critical locus. In particular, the length of a tie line goes to zero as it approaches the critical locus with increasing pressure, for example. The line length, for a particular tie line n is defined as

$$L_n = \sqrt{\sum_{i=1}^{n_c}(y_i^n - x_i^n)^2} \tag{4.13}$$

where y_i^n is the vapor phase mole fraction for component i on tie line n.

The algorithm used to solve the intersection equations at each pressure is:

1. For a given set of K-values, solve Eqs. 4.1 by Newton-Raphson iteration to obtain a set of intersecting tie lines in terms of the liquid phase mole fractions along each key tie lines.

2. Update K-values using one step of the accelerated successive substitution scheme of Mehra *et al.* [77].

3. Repeat steps 1-2 to convergence.

The algorithm for calculating the MMP is:

1. Begin with a relatively low pressure. Perform a negative flash to find the initial and injection tie lines at the low pressure.

2. Find the tie line intersection solution for the low pressure using the steps outlined in the Appendix.

3. Increase the pressure slightly and use the solution obtained in step 2 as the initial guess to solve the tie line intersection equations.

4. Repeat step 3 until one of the key tie lines shrinks to a point. The pressure at which some key tie line has zero length is the MMP.

This approach to solving for the key tie lines can be applied to systems with an arbitrary number of components in the oil or gas. If convergent solutions can be found for the intersection equations, the resulting MMP will be rigorously accurate if all the tie lines that make up the solution to the conservation equations are connected by shocks (Johns and Orr [76], Wang and Orr [66]). Even if rarefactions (continuous variations between key tie lines) are present, the error induced by the assumption of tie line intersections appears to be quite small (Wang and Orr [66]).

4.4 Examples of MMP Calculations

4.4.1 Four-component System: $CH_4/CO_2/C_4/C_{10}$

We begin the evaluation of accuracy of the tie line intersection method with a calculation of MMPs for the $CH_4/CO_2/C_4/C_{10}$ system considered by Jensen and Michelsen [69]. The oil mixture contains 40% CH_4, 5% CO_2, 20% C_4 and 35% C_{10}, and the displacement temperature is 71°C (160°F). Fig. 4.2 compares MMPs calculated by the tie line intersection approach to those reported by Jensen and Michelsen for mixtures of CH_4 and CO_2. Jensen and Michelsen used the Soave-Redlich-Kwong (SRK) equation of state and hence we do as well for the results shown in Fig. 4.2 only. In other examples described below, the Peng-Robinson equation (PREOS) was used.

Jensen and Michelsen demonstrated that the MMP estimated as the pressure at which the initial oil tie line became a critical tie line was not appropriate. They also showed that a single-cell mixing cell calculation based on forward contacts generated critical tie lines at pressures close to the pressure required for first-contact miscibility. However, for CO_2 mole fractions exceeding 6.6% in the injection gas, the single-cell estimate is 200-350 psia higher than the MMP calculated here. Fig. 4.3 illustrates why (Fig. 4.3 was generated with the PREOS, but the patterns are exactly the same with the SRK equation). Consider first what would happen if no CO_2 were present in the initial oil and pure methane were injected. In that ternary system the MMP would be the pressure at which the oil mixture lies on the extension of the critical tie line in the $CH_4/C_4/C_{10}$ face. Thus in that system, the initial oil tie line does determine the MMP.

Now consider the initial oil mixture of Jensen and Michelsen, which contains 5% CO_2. Fig. 4.3 shows the key tie lines for pure CH_4 injection. In this case, the initial oil tie line moves into the

interior of the quaternary diagram, but the crossover tie line remains in the $CH_4/C_4/C_{10}$ face. As the pressure is increased, the two-phase region shrinks, and the initial oil tie line approaches the critical locus first as the pressure increases. Thus, the initial oil tie line still determines the MMP for pure CH_4 injection.

Next, consider what happens as CO_2 is added to the injection gas. As the amount of CO_2 in the injection gas increases, the crossover tie line moves up the vertical surface shown in Fig. 4.3 . When the injection gas contains 6.6% CO_2, the crossover tie line coincides with the initial oil tie line. (This is an example of a degenerate case in which there are only two key tie lines.) For injection gas mixtures containing less than 6.6% CO_2, the initial oil tie line still controls development of miscibility, and the MMP remains unchanged (see Fig. 4.2). When the CO_2 fraction is larger than 6.6%, however, the situation changes. Now the crossover tie line lies above the initial tie line on the vertical surface shown in Fig. 4.3. The crossover tie line now approaches the critical locus at a lower pressure than does the oil tie line, and the crossover tie line determines miscibility. (These crossover tie lines are determined entirely by shocks, so the tie line intersection method is rigorously correct when the CO_2 fraction in the injection gas exceeds 6.6%). As the CO_2 fraction increases, the crossover tie line moves closer to the critical locus because the two-phase region is smaller at higher CO_2 fractions. Hence, the pressure increase required to move the critical locus to reach the crossover tie line decreases. The result is lower MMPs with increasing CO_2 fraction in the injection gas. Thus, the MMP is independent of CO_2 fraction at low CO_2 fraction (less than 6.6%) in the injection gas and relatively sensitive to CO_2 fraction at higher CO_2 fractions. Similar behavior was described by Dindoruk *et al.* ([75]) for injection of N_2/CH_4 mixtures.

To confirm the MMP calculated by the tie line intersection method, the MMP was also estimated by compositional simulation for 50% CO_2 in the injection gas. Fig. 4.4 shows the results of simulations with 100, 200, and 500 grid blocks, along with extrapolated recoveries at 1.2 pore volumes injected. The simulation estimate of 2500 psia obtained by extrapolation as described by Stalkup [68] agrees well with the analytical value of 2557 psia (using PREOS).

So why does the single cell calculation technique fail to produce the correct MMP over the full range of injection gas compositions? Fig. 4.5 shows the composition path of mixtures obtained by (1) mixing 80% injection gas with 20% oil and then (2) mixing the vapor from each contact with 20% fresh oil. The calculations were performed at the MMP of 2557 psia obtained by the tie line intersection calculation. The sequence of tie lines converges to the tie line that extends through the initial oil composition. Similarly, reverse contacts (fresh injection gas mixed with equilibrium liquid at each stage) converge to the tie line that extends through the injection gas composition. Thus, the single cell contacts do identify two of the $n_c - 1$ key tie lines. However, neither forward nor reverse contacts identify the crossover tie line, which is the tie line that becomes a critical tie line in this condensing/vaporizing gas drive. If the pressure is increased substantially above the actual MMP, it is possible for the forward contact procedure to generate tie lines close to the critical locus, as Jensen and Michelsen [69] showed, but that pressure is not an accurate estimate of the MMP. Fig. 4.2 shows that the MMPs calculated by forward contacts are higher (200-350 psia) than the MMPs calculated by the tie line intersection method in the region where the crossover tie line controls miscibility. Apparently, the first few forward contacts enrich the vapor phase enough in intermediate components that subsequent mixtures pass close to the critical locus. For example, the values reported by Jensen and Michelsen for forward contact MMPs are close to the pressure required for first-contact miscibility with the gas, pressures that are significantly higher than the actual MMP. Thus, we conclude that calculations based on single mixing cell should not be used to estimate MMPs if there is any chance that miscibility is determined by a tie line other than the initial oil or injection gas tie lines, the situation that exists in condensing/vaporizing drives ([67][74])

Hearn and Whitson [78] state, however, that a multiple mixing cell method ([61]) can be

used for such systems and report MMPs calculated by an unpublished method attributed to Zick. Multiple cell methods have much in common with compositional simulation, which does identify the appropriate tie lines by solving the conservation equations numerically and therefore gives MMPs consistent with the tie line intersection approach, as long as care is taken to account for numerical dispersion. Hence, it is reasonable to assume that an appropriate computational technique based on multiple mixing cells could be devised to substitute for calculations based on single mixing cells.

4.4.2 Crude Oil Systems

To examine how the tie line intersection method works for crude oil displacements we consider four examples described by Hearn and Whitson [78]. They reported results of slim tube experiments performed for lean and rich gas displacements of crude oil from the Safah field, Oman at 212°F (100°C). The oil and injected gas compositions are listed in Tables 1 and 2. Two sets of EOS phase behavior characterization were reported: a 15-component characterization and an 8-component characterization. Hearn and Whitson reported compositional simulation results and MMPs calculated by Zick's technique based on multiple mixing cells in addition to slim tube data.

Results of the analytical calculations for the rich gas displacement of the 8-component oil are shown in Fig. 4.6, which reports the distribution of key tie line lengths as a function of displacement pressure. With increasing pressure, the fourth crossover tie line shrinks to a point at a pressure of 3279 psia, therefore the MMP for this system is 3279 psia.

Slim tube data reported by Hearn and Whitson are compared with various calculated MMPs in Table 3. For the rich gas drive, the pressure increment between displacements was large enough (1000 psia), that the MMP was not determined with high precision in the experiment. Hearn and Whitson apparently used compositional simulation results to estimate the slope of the plot of recovery versus pressure, arriving at an estimate of 3300±100 psig for the MMP. They also reported a calculated MMP of 3190 psig obtained for the 8-component representation. That value was obtained both by compositional simulation and by the multiple mixing cell technique. The MMP value reported here, 3279 psia, is therefore in good agreement with both experimental data and calculations reported by Hearn and Whitson.

Results of the analytical calculations for the lean gas drive test of the 8-component characterization are shown in Fig. 4.7. Again, as the displacement pressure increases, the lengths of all the key tie lines decrease as the two-phase region shrinks. The MMP obtained for the 8-component representation was 5582 psia. In this case as well, there is considerable uncertainty in the experimental MMP. Only two slim tube tests were performed, at 2500 and 4500 psia. Neither was miscible. Linear extrapolation of the recovery data to 100% recovery (at 1.2 pore volumes injected) gives an estimate of 5000 psig, the value reported in the text of paper by Hearn and Whitson. Extrapolation from the data point at 4500 psia with the slope of the recovery curve obtained from compositional simulation gives an estimate of 5200 psig, the value reported in Table 3 of the paper. The calculated value reported by Hearn and Whitson was 5865 psig for the 8-component model. That value was reported both for calculations by compositional simulation and for forward contacts in a single mixing cell.

In our calculations, it is the second crossover tie line that determines the MMP, though the first crossover tie line is also nearly critical. It is possible that the MMP (5865 psia) obtained by the forward contact mixing cell calculation reported by Hearn and Whitson is higher than that obtained here because the mixing cell method finds the initial tie line, which requires a higher pressure to become a critical tie line. In our implementation of the Peng-Robison EOS, however, that pressure is 6163 psia. It is less clear why the compositional simulation result is exactly the same as the mixing cell result, though small uncertainties in the extrapolation to zero dispersion may be responsible. In any case, the calculated values are reasonably consistent with the experimental

observations, though it appears that the fluid characterization chosen by Hearn and Whitson gives an MMP that is a bit higher than the experimental result, whatever calculation method is used.

Fig. 4.8 and Fig. 4.9 are the results for the rich and lean gas drive tests respectively, using the 15-component characterization reported by Hearn and Whitson. Fig. 4.8 shows that the calculated MMP for the rich gas drive is 3115 psia. It is now the 8th crossover tie line that controls miscibility. Although the MMP is slightly lower than the calculated value using the 8-component characterization, it is still in good agreement with the slim tube result of 3300 psig. Fig. 4.9 shows the MMP for the lean gas drive is 5253 psia. In this example, the 15-component characterization resulted in better agreement of the calculated and experimental MMPs. Compared to 5582 psia of the 8-component estimate, the calculated MMP of 5253 psia for the 15-component characterization is closer to the slim tube MMP of 5200 psig.

Next we consider an example system described by Zick [67]. Table 4 shows the compositions of the oil and injected gas. The injection gas is a five-component mixture labeled as solvent A in Zick's paper (Gas 1 in Table 4), and the oil is reservoir fluid A (12-component Oil 1 in Table 4). The initial oil composition was obtained by flashing reservoir fluid A at 1500 psig. The resulting liquid phase was taken as the oil. The displacement calculations were performed at the reservoir temperature of 185°F. Fig. 4.10 shows the key tie line length distribution. At 2169 psia, the fourth crossover tie line becomes a critical tie line. The slim tube data showed an apparent MMP of 2200 psig. In this system as well, the agreement between calculated and experimental MMPs is good. We also calculated an MMP for a mixture of 20% methane plus 80% solvent A (Gas 2 in Table 4). In this case the initial oil was obtained by flashing reservoir fluid A at 3000 psig (Oil 2). The experimental MMP in this case was 3100 psig. Fig. 4.11 shows the resulting tie line lengths obtained in the calculation of tie line intersections. At around 2817 psia, the third and fourth crossover tie lines become parallel and the tie line intersection solution becomes singular. If large pressure steps are used, the solution sequence will step over the singularity, provided that the solution converges. If the pressure sequence is close to the MMP (and hence some tie line is near the critical locus), convergence difficulties can occur. In such cases, we used a third order extrapolation scheme to obtain a reasonably good estimate of liquid phase compositions as well as K-values for the next pressure step. As it turns out, the singularity is not uncommon, especially when the oil and gas contain a large number of components, some of which have similar K-values. For such systems, a different version of the intersection equations suggested by Jessen *et al.* [79] avoids difficulties that arise from coinciding tie lines. As the results indicate, the calculated MMP of 3013 psia is in good agreement with the slim tube result of 3100 psig. The final example reported by Zick was the injection of solvent A at the minimum enrichment level (77% solvent A). Fig. 4.12 shows the key tie line length variations with pressure (for Oil 3 and Gas 3). Again the singular situation arises near 3100 psia. Using the extrapolation technique, we obtained a calculated MMP of 3283 psia, which agrees well with the reported slim tube measurement of 3400 psig. We also performed numerical simulations to calculate the MMPs for these systems. The MMPs are: 2253 psia for Oil 1 and Gas 1; 3093 psia for Oil 2 and Gas 2; and 3256 psia for Oil 3 and Gas 3. All MMPs obtained by numerical simulations agree well with both the analytical MMPs and the slim tube test results. Table 3 and Fig. 4.13 summerize the calculations of MMPs using different methods in comparison with the slim tube measurements of MMPs. Table 3 indicates that the analytical method for calculating MMPs is at least as accurate as the other methods.

4.5 Discussion

The MMP calculation technique described here is much faster than conventional compositional simulation. Typical computation times are less than half an hour on a DEC-alpha workstation. Run times for compositional simulation, with attention paid to extrapolation to account for

effects of numerical dispersion, are at least an order of magnitude greater. Furthermore, the MMP can be determined much more precisely because the calculation can be performed easily for small pressure increments that locate the MMP accurately. Compositional simulations, which are much lengthier, are necessarily restricted to larger pressure increments.

The technique described here can be used in several applications that call for rapid calculation of MMPs. In many gas injection processes, produced gas is reinjected, possibly after blending with gas of some other composition. The tie line intersection method could be used in conjunction with compositional analysis of the injected gas stream to determine whether the blended composition meets a particular MMP specification. Similarly, the method can be used to assess quickly the effect of design injection gas composition changes on MMP, results which will have value as optimum injection gas compositions are determined. In addition, the analytical method could be used to test rapidly whether a proposed fluid characterization gives a calculated MMP consistent with experimental observation. Thus, the proposed method will make possible direct determination of MMPs in situations where previously available calculation techniques were not practical because they were too time consuming.

4.6 Conclusions

In this chapter we have proposed an analytical approach to calculate MMPs for displacements involving an arbitrary number of components in either the gas or the oil: The approach is based on the analytical theory of one-dimensional two-phase multicomponent flow. Calculations performed with the tie line intersection technique lead to the following conclusions:

1. Forward and reverse contact calculations with a single mixing cell do not give accurate MMP estimates when development of miscibility is controlled by a tie line other than the tie line that extends through the initial oil (forward contacts) or the injection gas (reverse contacts).
2. MMPs calculated by the tie line intersection technique agree well with experimental observations and with MMPs calculated by compositional simulation. The accuracy of the calculated MMP is determined primarily by the accuracy of the fluid characterization.
3. The MMP calculation technique presented here can be used to test how accurately a fluid characterization reproduces slim tube MMP observations.

4.7 Nomenclature

x= liquid phase composition (mole fraction)
y= vapor phase composition (mole fraction)
V= vapor phase mole fraction
K= equilibrium ratio (K-value)
L= tie line length

4.8 Appendix

The analytical method for calculating MMPs presented in this chapter relies on the solution of the tie line intersection equations (Eqs. 4.1) for a sequence of increasing pressures. The construction of tie line intersection solutions at a low pressure is a critical first step.

The tie line intersection method requires the solution of a system with $n_c(2n_g - 3) - \Sigma_{i=1}^{n_g-2} i$ unknowns (n_c is the total number of components in the system and n_g is the number of components

present in the injection gas). For a realistic phase behavior characterization in which oil and gas are represented by a substantial number of components, the number of unknowns is large. Making a random guess of so many unknowns does not lead to converged solutions, and a more systematic approach is required.

Here we propose a different approach. Instead of trying to make a good initial guess for a particular system at a low pressure, we actually construct the exact solution at the low pressure by starting from a simple system whose solution is easy to construct. The solution for a single-component gas injection system is well established in Johns and Orr[76] and Wang and Orr[66]. We use that approach to find a solution for the actual initial oil but with an injection gas that contains only one component. We found that choosing the component with the highest K-value works well. We then make use of the fact that the solution to a general system is continuous with respect to changes in the pressure and the compositions in oil and gas (Johns *et al.* [74]), we add a small amount of the component with the second highest K-value to the injection gas and construct the solution for the new system whose injection gas now contains two components. The process of addition of one component continues until the composition of the first component matches that of the actual injection gas. Then we add a small amount of the component with the third highest K-value and construct the solution with three-component injection gas by using the similar solution with a two-component injection gas. The whole process is repeated until the compositions of all components in the gas match those of the actual injection gas. The initial solution is therefore obtained as the exact solution for the actual system we intend to solve at a relatively low pressure far from the MMP.

4.9 SI Metric Conversion Factors

psi × 6.894 757 E+00 = kPa
° F × 0.555 556 E+00 = ° K - 255.372

Component	Oil and Gas Compositions (Mole Fraction) (8-comp)		
	Reservoir Oil	Lean Gas	Rich Gas
$C_1 + N_2$	0.341	0.848	0.646
$C_2 + CO_2$	0.056	0.105	0.124
C_3	0.055	0.036	0.103
C_4	0.059	0.011	0.089
$C_5 + C_6$	0.092	-	0.038
$C_{7+}(1-2)$	0.195	-	-
$C_{7+}(3-4)$	0.155	-	-
$C_{7+}(5)$	0.047	-	-

Table 1. Oil and gas compositions (8-component characterization) from Hearn and Whitson ([78]). T=212°F.

Component	Oil and Gas Compositions (Mole Fraction) (15-comp)		
	Reservoir Oil	Lean Gas	Rich Gas
N_2	0.007	0.008	0.007
CO_2	0.006	0.015	0.013
C_1	0.334	0.840	0.639
C_2	0.050	0.091	0.111
C_3	0.055	0.036	0.103
IC_4	0.021	0.006	0.036
C_4	0.039	0.005	0.053
IC_5	0.020	-	0.017
C_5	0.028	-	0.014
C_6	0.044	-	0.006
$C_{7+}(1)$	0.096	-	-
$C_{7+}(2)$	0.099	-	-
$C_{7+}(3)$	0.087	-	-
$C_{7+}(4)$	0.068	-	-
$C_{7+}(5)$	0.046	-	-

Table 2. Oil and gas compositions (15-component characterization) from Hearn and Whitson ([78]). T=212°F

Method	Minimum Miscibility Pressure (psia)						
	Lean(8)	Lean(15)	Rich(8)	Rich(15)	Zick1	Zick2	Zick3
Single Cell [20]	5880	5860	4520	4540	-	-	-
Multiple Cell [20]	-	-	3205	3325	-	-	-
Num. Simul. [20]	5880	5860	3205	3325	-	-	-
Negative Flash	6163		6163		7452		
Analytical	5582	5253	3279	3115	2169	3013	3283
Slim Tube Test [20][9]	5215(±200)	5215(±200)	3315(±100)	3315(±100)	2215	3115	3415

Table 3. Comparison of MMPs calculated by different methods.

Component	Oil and Gas Compositions (Mole Fraction)					
	Oil(Case1)	Gas(Case1)	Oil(Case2)	Gas(Case2)	Oil(Case3)	Gas(Case3)
CO_2	0.0492	0.2218	0.0659	0.17744	0.06779	0.17079
CH_4	0.2164	0.2349	0.3644	0.38792	0.38740	0.41087
C_2	0.0470	0.2350	0.0531	0.18800	0.05352	0.18095
C_3	0.0403	0.2745	0.0373	0.21960	0.03668	0.21136
C_4	0.0318	0.0338	0.0262	0.02704	0.02541	0.02603
C_5	0.0243	-	0.0189	-	0.01815	-
$C_6 - C_7$	0.0616	-	0.0458	-	0.04363	-
$C_8 - C_{10}$	0.1196	-	0.0879	-	0.08339	-
$C_{11} - C_{14}$	0.1108	-	0.0812	-	0.07677	-
$C_{15} - C_{19}$	0.0984	-	0.0722	-	0.06821	-
$C_{20} - C_{29}$	0.0908	-	0.0666	-	0.06297	-
C_{30+}	0.1098	-	0.0805	-	0.07608	-

Table 3. Oil and gas compositions from Zick [67]. T=185°F. Case 1 is shown in Fig. 4.10 , Case 2 is shown in Fig. 4.11 and Case 3 is shown in Fig. 4.12.

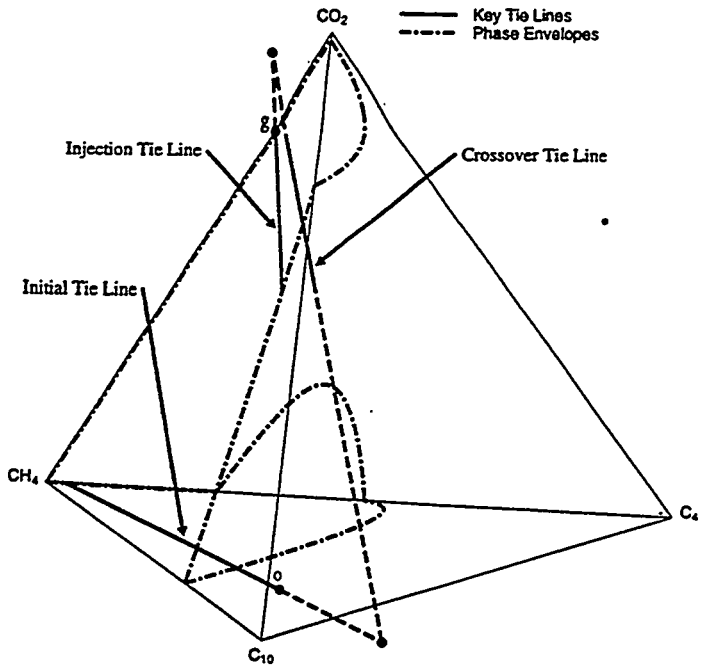

Figure 4.1: Key tie lines intersect each other for a displacement of oil o by gas g.

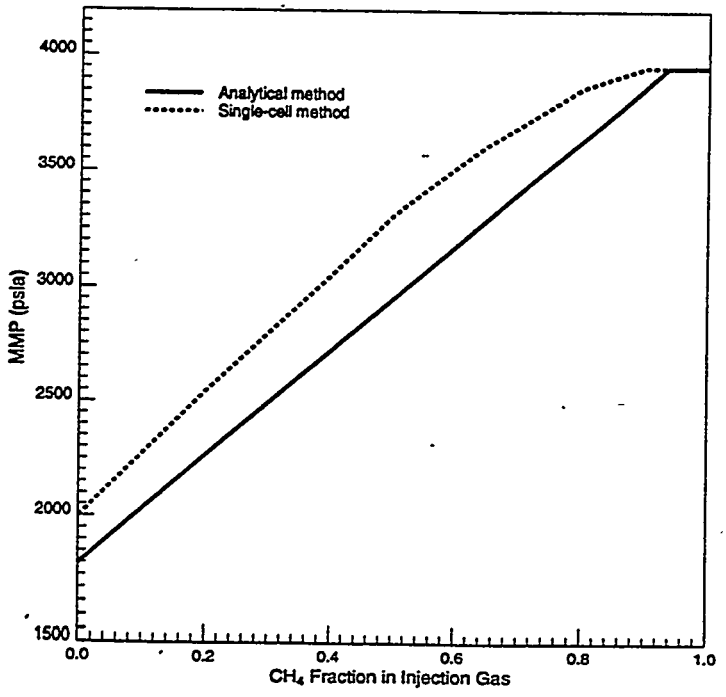

Figure 4.2: Comparison of MMPs calculated by forward contacts in a single mixing cell and by the tie line intersection method.

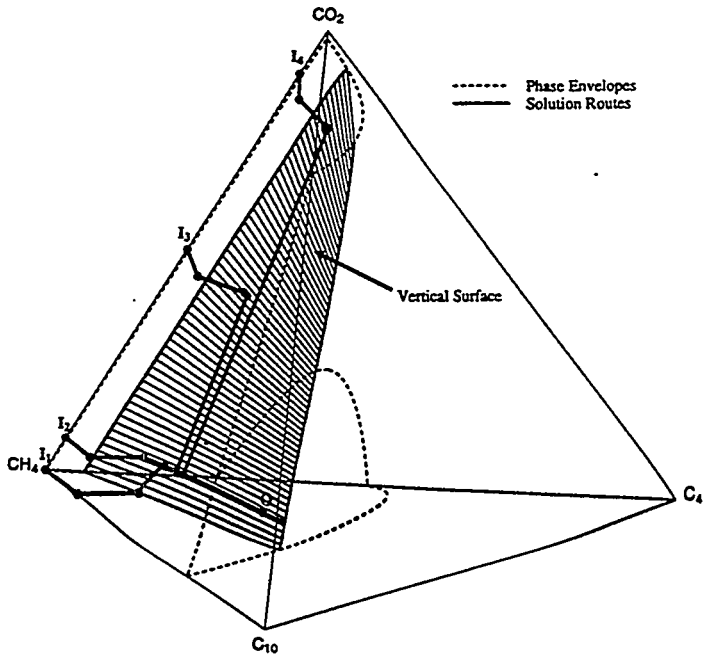

Figure 4.3: Composition paths and crossover tie line surface for the displacement of oil O (40% CH_4, 5% CO_2, 20% C_4 and 35% C_{10}) by I_1 to I_4 at 1600 psia and 160F.

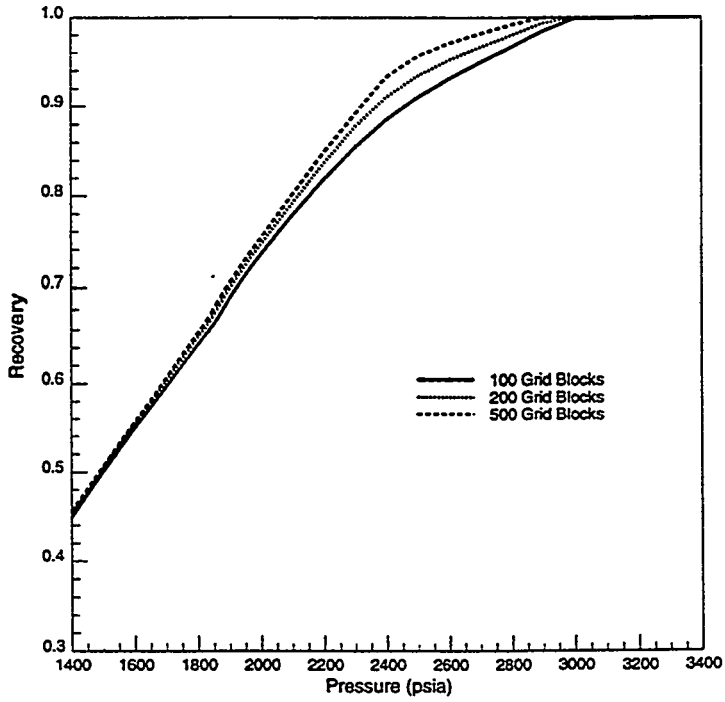

Figure 4.4: Compositional simulation results for the displacement of 40% CH_4, 5% CO_2, 20% C_4 and 35% C_{10} by 50% CO_2 and 50% CH_4 at 160F. The calculated MMP is 2500 psia.

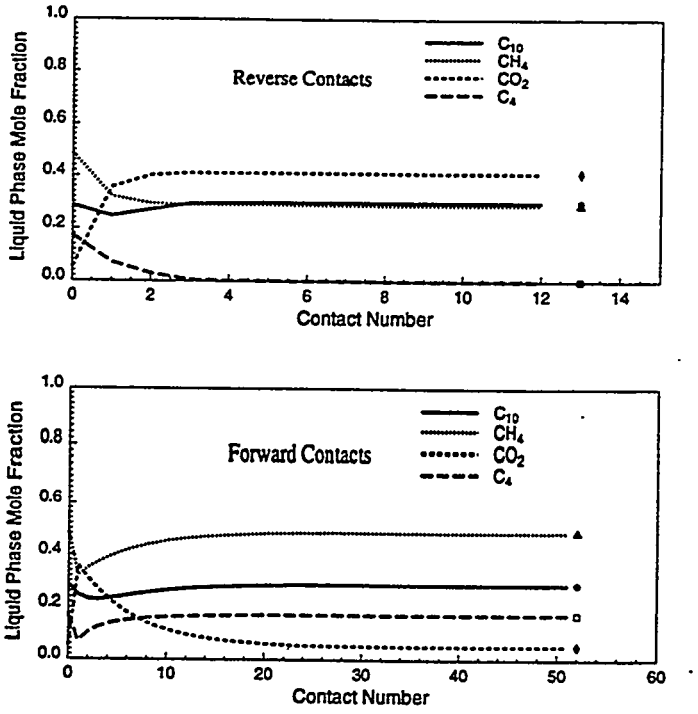

Figure 4.5: Convergence of reverse contacts to the injection gas tie line and forward contacts to the initial oil tie line (symbols indicate the phase compositions obtained by a negative flash).

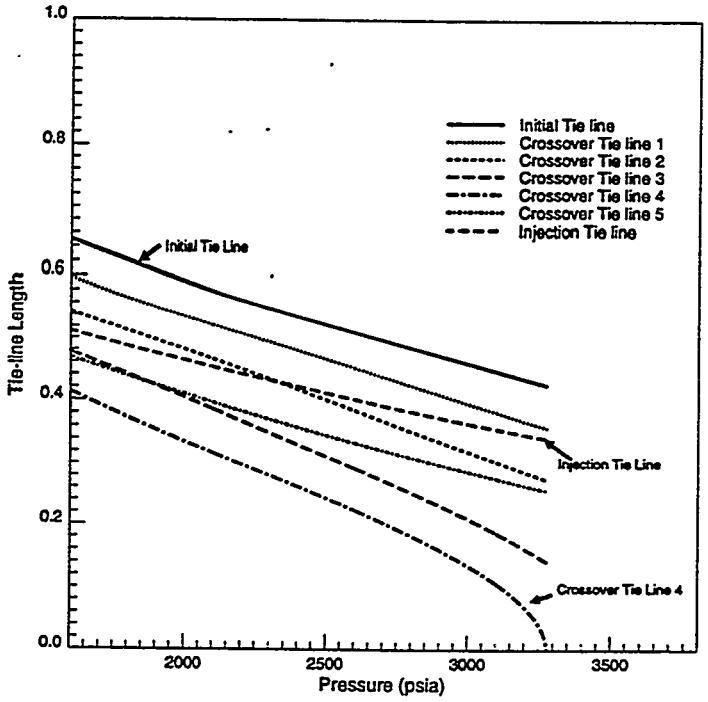

Figure 4.6: Tie line lengths for rich gas displacement of an eight-component oil (Hearn and Whitson [78]) at 212F. The calculated MMP is 3279 psia.

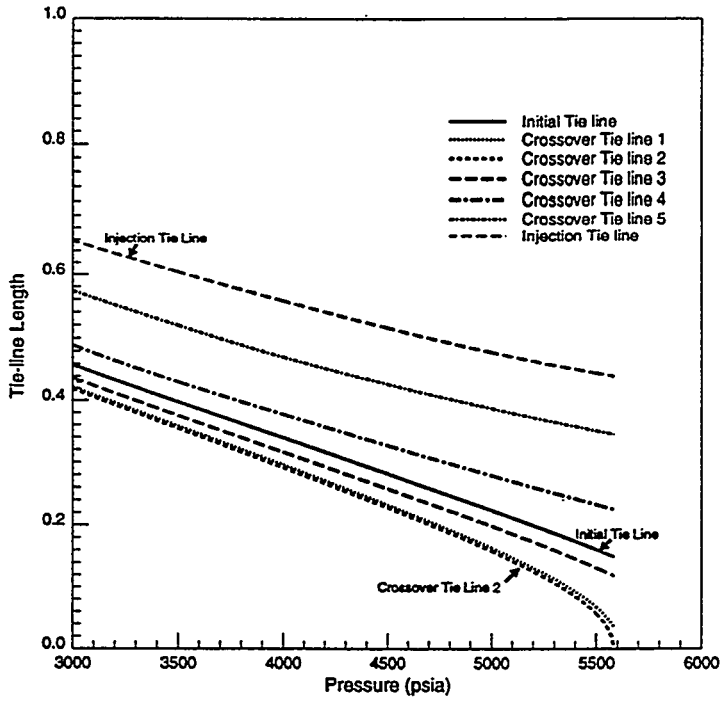

Figure 4.7: Tie line lengths for lean gas displacement of an eight-component oil (Hearn and Whitson [78]) at 212F. The calculated MMP is 5582 psia.

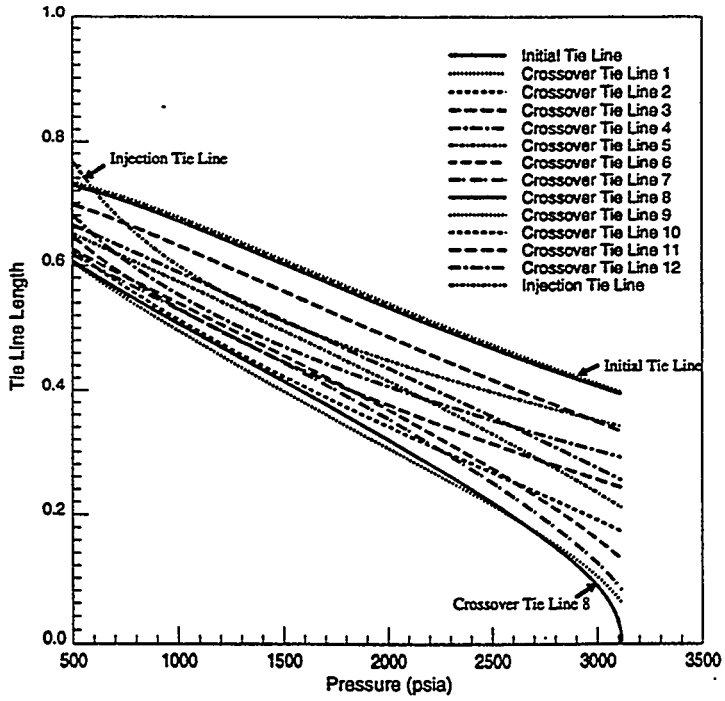

Figure 4.8: Tie line lengths for rich gas displacement of a 15-component oil (Hearn and Whitson [78]) at 212F. The calculated MMP is 3115 psia.

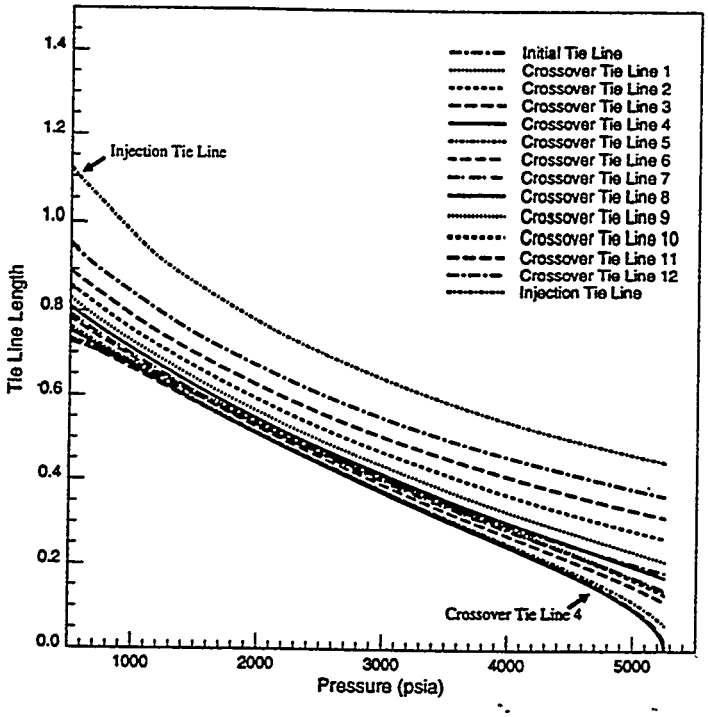

Figure 4.9: Tie line lengths for lean gas displacement of a 15-component oil (Hearn and Whitson [78]) at 212F. The calculated MMP is 5253 psia.

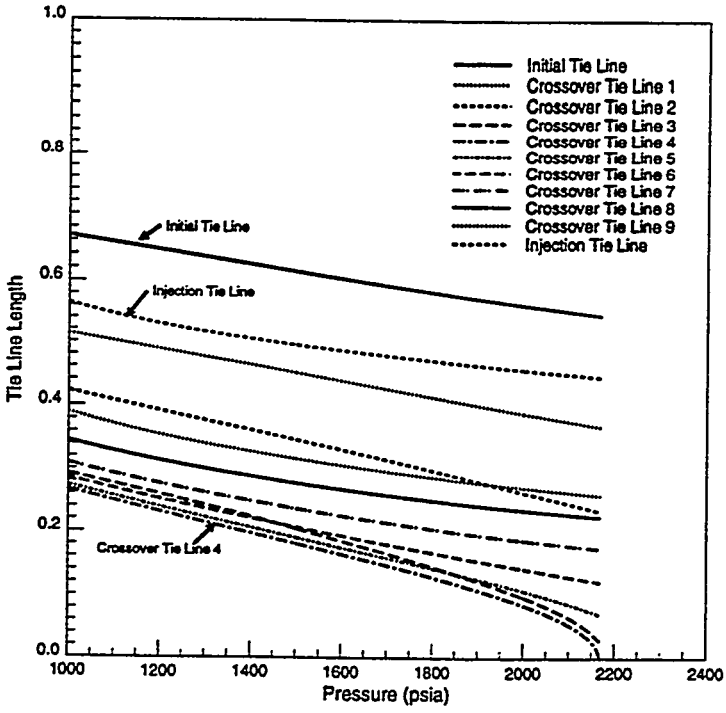

Figure 4.10: Tie line lengths for displacement of oil A (Zick [67]) by solvent A at 185F. The calculated MMP is 2169 psia.

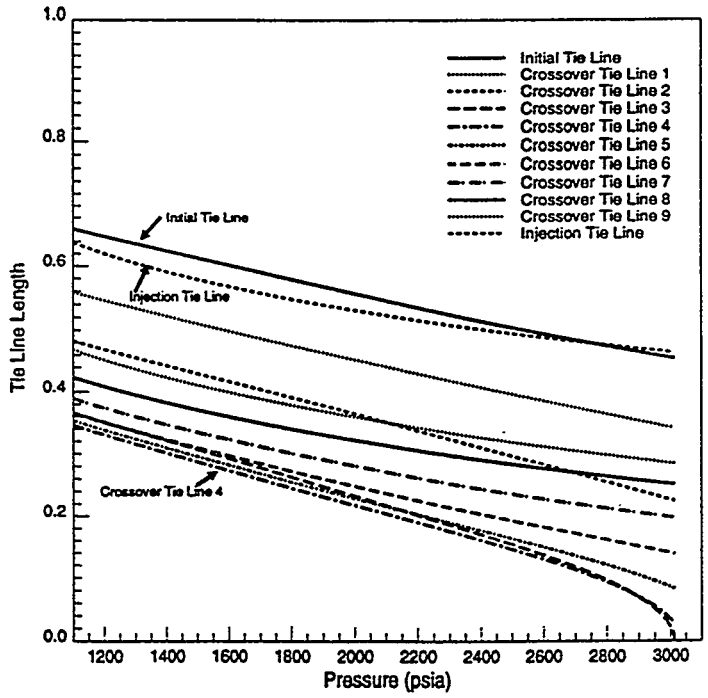

Figure 4.11: Tie line lengths for displacement of oil A (Zick [67]) by 20% CH_4 and 80% solvent A at 185F. The calculated MMP is 3013 psia.

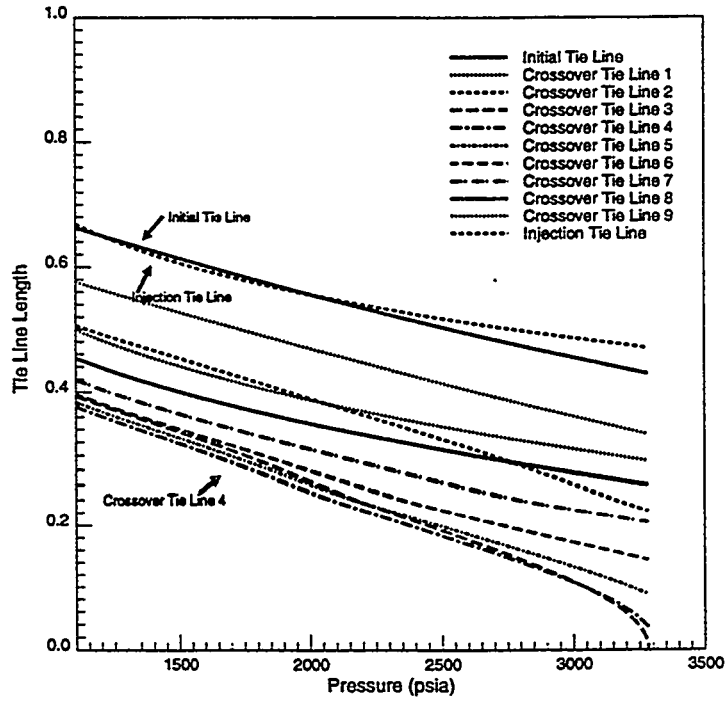

Figure 4.12: Tie line lengths for displacement of oil A (Zick [67]) by 23% CH_4 and 77% solvent A at 185F. The calculated MMP is 3283 psia.

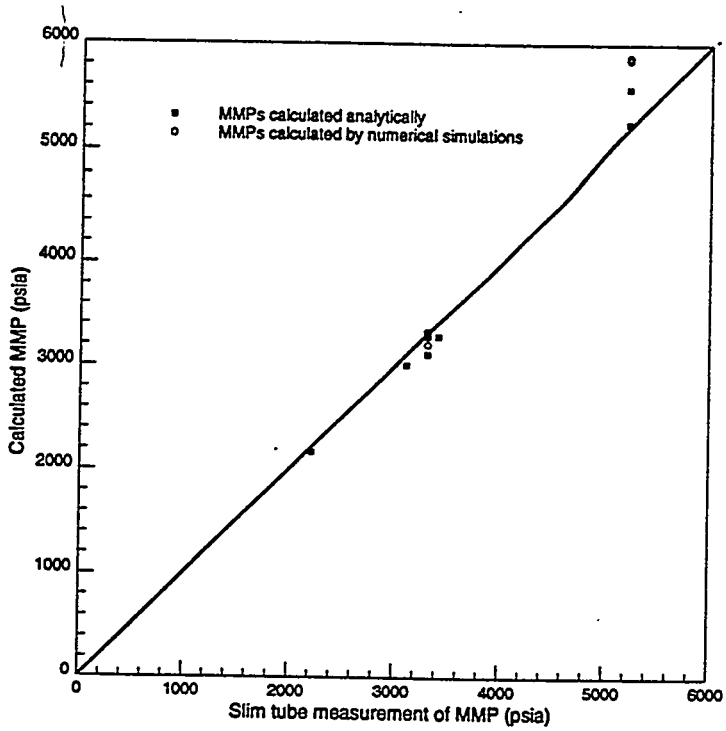

Figure 4.13: Comparison between analytically calculated MMPs with slim tube test results.

5. A Streamline-Based 3D Field-Scale Compositional Reservoir Simulator

Marco R. Thiele, Rod P. Batycky, and Martin J. Blunt

This chapter presents the extension of the streamline approach to full-field, three-dimensional (3D) compositional simulation. The streamline technique decomposes a heterogeneous 3D domain into a number of one-dimensional (1D) streamlines along which all fluid flow calculations are done. Streamlines represent a natural, dynamically changing grid for modeling fluid flow. We use a 1D compositional finite-difference simulator to move components numerically along streamlines, and then map the 1D solutions back onto an underlying Cartesian grid to obtain a full 3D compositional solution at a new time level.

Because of the natural decomposition of the 3D domain into a number of 1D problems, the streamline approach offers substantial computational efficiency and minimizes numerical diffusion compared to traditional finite-difference methods. We compare our three and four component solutions with solutions from two finite difference codes, UTCOMP and Eclipse 300 (E300). These examples show that our streamline solutions are in agreement with the finite-difference solutions, are able to minimize the impact of numerical diffusion, are faster by orders of magnitude. Numerical diffusion in finite-difference formulations can interact with reservoir heterogeneity to substantially mitigate mobility differences and lead to optimistic recovery predictions.

We demonstrate the efficiency and usefulness of the streamline-based simulator on a 518,400 gridblock, 3D, heterogeneous, 36-well problem for a condensing-vaporizing gas drive with four components. We can simulate this problem on an average-size workstation in three CPU days. It takes approximately the same amount of time to simulate the upscaled 28,800 gridblock version of the problem using finite-differences.

We conclude with a qualitative discussion explaining the near-linear scaling of the streamline approach with the number of gridblocks and the cubic and higher scaling exhibited by one of the finite-difference codes.

5.1 Introduction

The use of streamlines and streamtubes to model convective displacements in heterogeneous media has been presented repeatedly since the early work by Muskat[80, 81, 82], Fay and Prats[83], and Higgins and Leighton[84, 85, 86]. Important subsequent contributions are due to Parsons[87], Martin and Wegner[88], Bommer and Schechter[89], Lake *et al.*[90], Mathews *et al.*[91], Emanuel *et al.*[92, 93, 94], Renard[95], and Hewett and Behrens[96].

Recently, streamline methods have received renewed attention by several groups as a viable alternative to traditional finite-difference (FD) methods for large, heterogeneous, multiwell, multiphase simulations, which are particularly difficult for FD simulators to model adequately[97, 98, 99, 100, 101, 102, 103, 104, 105, 106, 107, 108, 109]. Large speed-up factors compared to traditional FD solutions, minimization of numerical diffusion and grid orientation effects, and the inherent simplicity of the approach offer unique opportunities for integration with modern reservoir characterization methods. Examples include ranking of equiprobable earth models, estimation of the uncertainty in production forecasts due to the uncertainty in the geological description, rapid assessment of

[3]The material in this chapter was presented at the 1997 SPE Annual Technical Conference and Exhibition in San Antonio, Texas, Oct 5-8, 1997, and is published as SPE paper 38889 in the conference proceedings.

production strategies such as infill drilling patterns and miscible gas injection[93, 99, 106, 111, 112]. In addition, streamlines may offer an attractive alternative to well-known problems with upscaling of absolute and pseudorelative permeabilities by allowing larger geological models and requiring upscaling across a smaller range of scales[113, 114].

Our streamline approach for reservoir simulation hinges on two important extensions to past streamline/streamtube methods: (1) the use of true 3D streamlines[110] and (2) and numerical solutions of the transport equations along periodically changing streamlines[89, 95]. With these extensions we have been able to simulate realistic fluid flow in detailed, heterogeneous, 3D reservoir models much more efficiently than FD methods[103, 106, 107, 108].

We emphasize that reservoir simulation using streamlines is not a minor modification of current FD approaches, but instead represents a significant shift in methodology. By transporting fluids along periodically changing streamlines, the streamline approach is equivalent to a dynamically adapting grid that is decoupled from the underlying, static, grid used to describe the reservoir geology. The 1D nature of a streamline is translated into a 1D transport problem that can be solved easily and efficiently. This is considerably different from FD methods that use the same grid to solve both for pressure and for saturation/composition, and are forced to move fluids only along grid directions.

The implementation of our approach uses five key ideas:

Heterogeneity and Well Locations: Streamlines represent the natural grid to capture high and low flow regions due to well placements and reservoir heterogeneity[80, 87, 88, 92, 96]. Muskat first used streamline to estimate reservoir drainage volumes resulting from well placements. The use of streamlines to capture the impact of heterogeneity is more recent and is due to the work by Lake *et al*[90] and by Emanuel and co-workers[92, 93, 94, 91, 96].

3D Streamlines: Tracing 3D streamlines using a time-of-flight (TOF) approach as presented by Pollock[110] and Datta-Gupta and King[115]. Using a TOF formulation along streamlines is significantly easier than using a volumetric formulation along streamtubes, particularly for true 3D flow. It is straightforward to show that a volumetric coordinate along a streamtube is equivalent to a TOF coordinate along a streamline[103].

1D Numerical Solutions: Moving solutions forward in time numerically along 1D streamlines as proposed by Bommer and Schechter[89]. By using a numerical FD solution along streamlines extends the approach to general initial conditions, changing boundary conditions, and any type of displacement or recovery mechanism which can be formulated in one dimension.

Updating Streamlines: Capturing the changing total velocity field due to problem nonlinearities as well as time-varying boundary conditions (wells coming online as well as shutting-in) by periodically recalculating the streamlines[116, 95, 101, 102, 103, 105, 106, 107, 108]. Because streamlines represent the natural flow grid along which fluids want to move, far fewer streamline updates (global pressure solves) are required to move the fluids forward in time compared to FD methods. This results in a significant computational efficiency. Combining numerical 1D solutions (point 3 above) with periodically updated 3D streamlines is the centerpiece of our approach. It allows to capture nonlinear flow mechanism in 3D while retaining the speed advantages that made approximate 2D streamtube methods attractive in the past.

Operator-Splitting: Using operator-splitting to capture flow mechanisms that are not aligned with the total velocity field, such as gravity[117, 98, 107]. The inability of 2D streamtube methods in the past to account for gravity effects has been a long-standing criticism. By using operator splitting and 3D streamlines it is possible to account for any mechanism that is not aligned with the total velocity field, such as transverse diffusion, capillary crossflow, and

gravity. Operator splitting is a well established mathematical concept and has been used in the past to solve convective-diffusive transport problems[118], transport problems on multiple grids[119], and transport problems with gravity[120, 98, 107].

5.2 Compositional Displacements

In this chapter we consider the extension of the streamline approach to compositional displacements. We have described the application of the method to immiscible and miscible displacements in our previous work[101, 111, 103, 104, 105, 106, 107], and the reader is referred to those publications for additional details.

Modeling mass transfer effects correctly becomes imperative when designing injection processes that will enhance the recovery of oil compared to traditional waterflooding methods. For example, under the right physical conditions gas or solvent injection can lead to very efficient recovery processes, as capillary forces that cause entrapment in immiscible displacements are reduced leading to much lower residual oil saturations. If the injected solvent is completely miscible, i.e. only a single phase is formed over the range of pressures and temperatures present in the reservoir, then the displacement is said to be first-contact-miscible (FCM) and the residual oil saturation in a swept zone is theoretically zero. In many cases however, miscibility is achieved in-situ after the solvent has contacted the oil repeatedly and mass transfer occurs between the injected solvent and the oil in place. These cases are referred to as multicontact miscibility (MCM). If miscibility is never achieved for the range of pressures and compositions in a particular displacement, then the displacement is referred to as being immiscible, although mass transfer still occurs between the flowing phases. For a general overview on the subject the reader is referred to Stalkup's monograph[121].

Although the residual oil saturations that can be achieved by gas injection processes can be very low, there is an offsetting effect caused by the injected fluids usually being significantly more mobile and of lower density than the resident oil. Higher mobility can lead to channeling and viscous fingering[122]. A significant density contrast can lead to gravity override. These effects have been observed experimentally at the core scale by several investigators[123, 124, 125, 126] and have also been confirmed numerically. Experimental work has also underscored the importance of crossflow mechanism due to capillary forces and concentration gradients, but is remains unclear to what extent these mechanisms act at the scale of typical field-scale reservoir simulation gridblock and how they affect the flow between gridblocks at that scale.

It is generally agreed though, that successful modeling of gas injection processes at the field scale must be able to capture the relevant interactions of the first-order transport mechanisms with the geological description of the reservoir. The successful study of these interactions has proven to be difficult in the specific case of compositional displacements. Problems usually encountered in traditional immiscible displacements such as numerical diffusion and upscaling of absolute and relative permeabilities[113, 114] are exasperated in compositional displacements because of the strong nonlinearities introduced by the thermodynamic equilibrium calculations[127, 128]. The impact of numerical diffusion is to mitigate the mobility and density contrasts of the fluids through mixing and underestimate bypassing and gravity override[129, 130]. Upscaling of fine-scale heterogeneities tends to modify local contact efficiencies and the multicontact miscibility process[131, 128, 132]. An additional difficulty —which is unique to compositional modeling— is the need to reduce the large number of hydrocarbon components present in a real system to a number that can still represent the phase behavior of the system and is numerically feasible[133]. Unfortunately, attempts to use finer grids with more geological detail and/or more pseudocomponents for a better representation of the phase behavior quickly lead to computational costs which are beyond current simulator capabilities, particularly for full-field development studies. As a result, most field-scale compositional simulation use grids with order 10^3 to 10^4 gridblocks.

Streamlines can offer an attractive alternative to FD methods because of the natural decomposition of a 3D, heterogeneous problem into a series of simpler 1D, homogeneous problems. The advantage comes from the fact that the 1D solutions along the streamlines are completely independent from the size of the original 3D problems as well as the magnitude of the absolute permeability. The computational requirements for large field-scale problems are thereby reduced significantly, and problems with numerical diffusion, upscaling, and equilibrium calculations are minimized leading to more accurate predictions.

5.3 The Streamline Formulation

Here we develop the streamline formulation under the special assumption that gravity, capillary, and diffusive forces are negligible. All of these effects can be included using operator splitting in the same way gravity is included in oil-water displacements[106, 98].

The multidimensional mass conservation equations for a chemical species, i, flowing under convective forces only can be written as

$$\phi \frac{\partial C_i}{\partial t} + \vec{u}_t \cdot \nabla F_i = 0 \quad , \quad i = 1, \ldots, n_c \tag{5.1}$$

where

$$C_i = \sum_{j=1}^{n_p} x_{ij} \rho_j S_j \quad , \quad j = 1, \ldots, n_p \tag{5.2}$$

are the local moles of component i and

$$F_i = u_D \sum_{j=1}^{n_p} x_{ij} \rho_j f_j \quad , \quad j = 1, \ldots, n_p \tag{5.3}$$

is the molar flux of component i. n_p is the number of phases, n_c is the number of components, x_{ij} is the mole fraction of component i in phase j, ρ_j is the density of phase j, S_j is the saturation of phase j, u_D is the total dimensionless volumetric velocity, ϕ is the porosity, and f_j is the fractional flow of phase j given by

$$f_j = \frac{k_{rj}/\mu_j}{\sum_{k=1}^{n_p} k_{rk}/\mu_k} \quad . \tag{5.4}$$

Here k_{rj} is the relative permeability of phase j and μ_j is the viscosity of phase j.

The streamline approach centers on transforming Eq. 5.1 into a 1D problem along streamlines. To do that we determine the time-of-flight[110, 115] (TOF) along a streamline, which is given by

$$\tau = \int_0^{\zeta} \frac{\phi}{u_t} ds \quad , \tag{5.5}$$

and leads to the definition

$$|u_t| \frac{\partial}{\partial s} \equiv \vec{u}_t \cdot \nabla = \phi \frac{\partial}{\partial \tau} \quad . \tag{5.6}$$

Using Eq. 5.6 it is possible to rewrite Eq. 5.1 as a one-dimensional formulation for each component

$$\frac{\partial C_i}{\partial t} + \frac{\partial F_i}{\partial \tau} = 0 \quad , \quad i = 1, \ldots, n_c \quad . \tag{5.7}$$

The total velocity field, u_t, necessary to determine the TOF using Eq. 5.5 can be determined by solving the total mass balance equation

$$\sum_{i=1}^{n_c} \left\{ \phi \frac{\partial C_i}{\partial t} + \vec{u}_t \cdot \nabla F_i = 0 \right\} \quad , \tag{5.8}$$

for pressure and then using Darcy's law to determine the local velocity field. For the work presented here, we have approximated Eq. 5.8 by

$$\nabla \cdot \vec{\vec{K}} \cdot (\lambda_t \nabla P) = 0 \ , \tag{5.9}$$

where $\vec{\vec{K}}$ is the local permeability tensor and λ_t is the total mobility given by

$$\lambda_t = \sum_{j=1}^{n_p} k_{rj}/\mu_j \ . \tag{5.10}$$

Eq. 5.9 assumes that the pressure distribution solved under the assumption of incompressibility is close the solution obtained assuming a compressible system. For systems with a small pressure drop compared to the average reservoir pressure between injectors and producers — which we consider here — this is probably not a bad assumption. We are currently pursuing the extension to a fully compressible system, in which Eq. 5.8 is used to find the total velocity field rather than Eq. 5.9. This involves only a minor modification in the tracing algorithm and is a straightforward extension.

Although Eq. 5.9 does not account for compressibility and volume-change-on-mixing, these effects are accounted for in the 1D solution, Eq. 5.7, by solving for the dimensionless total velocity, u_D, which is no longer constant. Details of this are outlined in in the following section.

5.4 One-Dimensional Compositional Solver

Rewriting Eq. 5.1 as Eq. 5.7 decouples the global 3D, heterogeneous flow problem into a series of 1D, homogeneous problems along streamlines. The original permeability distribution is now reflected by the geometry and the TOF distribution of a streamline. Using Eq. 5.7 allows to simulate any type of transport mechanism by simply using the appropriate 1D solver along streamlines. For this work we have written a 1D compositional solver for Eq. 5.7 which is described next.

We solve Eq. 5.7 for the total moles of component i using an explicit first-order in time, second-order in space TVD scheme[134]. The scheme can be improved to second-order time accuracy using a simple modification[135]. Let

$$F_i = u_D \hat{F}_i \tag{5.11}$$

then we can write the finite-difference form of Eq. 5.7 as

$$C_{i,k}^{n+1} = C_{i,k}^{n} + \frac{\Delta t}{\Delta \tau} \left(\left[u_D \hat{F}_i \right]_{k-\frac{1}{2}}^{n} - \left[u_D \hat{F}_i \right]_{k+\frac{1}{2}}^{n} \right) \ , \tag{5.12}$$

where the intercell fluxes, $\hat{F}_i$, are approximated by

$$\hat{F}_{i,k+\frac{1}{2}}^{n} = \hat{F}_{i,k}^{n} + \frac{\Phi_{i,k+\frac{1}{2}}^{n}}{2} \left(\hat{F}_{i,k+1}^{n} - \hat{F}_{i,k}^{n} \right) \left(1 - \frac{\Delta t}{\Delta \tau} \right) \ . \tag{5.13}$$

Φ is the van Leer limiter[136]

$$\Phi = \frac{r + |r|}{1 + |r|} \tag{5.14}$$

and r is a function of the ratio of adjacent flux differences

$$r_{i,k+\frac{1}{2}}^{n} = \frac{F_i^n - F_{i-1}^n}{F_{i+1}^n - F_i^n} \ . \tag{5.15}$$

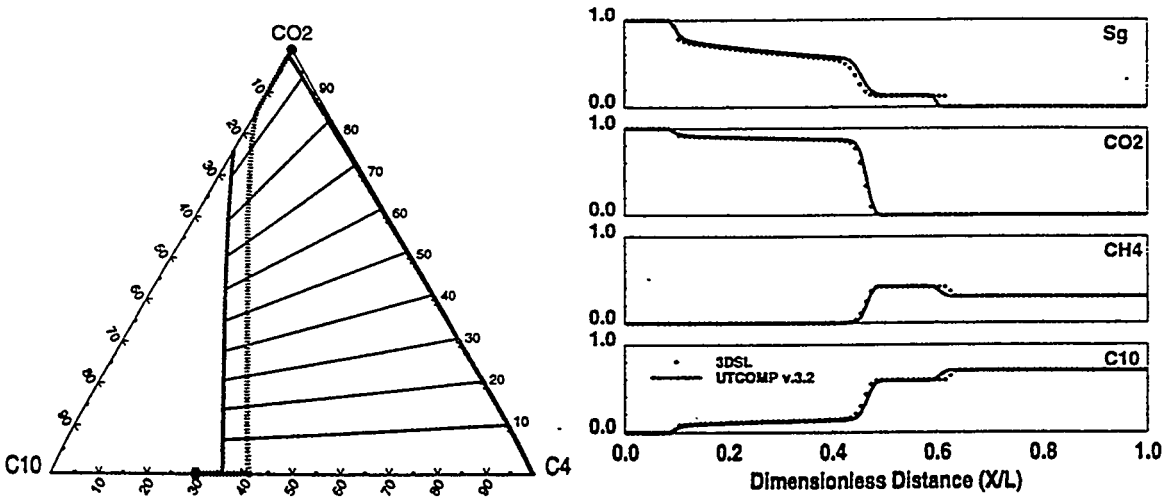

Figure 5.1: One-dimensional, TVD solutions at $t_D = 0.5$ with 100 grid blocks using UTCOMP (v.3.2 w/ automatic time stepping) and the 1D compositional simulator (CFL=0.5) used in this work for pure CO_2 injection into a 30/70 mixture of CH_4 and C_{10} at 1600 psia and 160° F.

Here k is the node counter of the discretized streamline, and n is the local time level along each streamline. We then find the total mole fractions for each component using

$$z_l = \frac{C_l}{\sum_{i=1}^{n_c} C_i} \,. \tag{5.16}$$

Compressibility effects due to volume-change-on-mixing and pressure gradients are accounted for by solving iteratively for the total dimensionless velocity, u_D, together with Eq. 5.12 using a total mass balance equation of the form[137]

$$u^n_{D,k+\frac{1}{2}} = \frac{\sum_{i=1}^{n_c} \left[\frac{\Delta\tau}{\Delta t} \left(C^n_{i,k} - C^{n+1}_{i,k} \right) + \left(u_D \hat{F}_i \right)^n_{k-\frac{1}{2}} \right]}{\sum_{i=1}^{n_c} \hat{F}_{i,k+\frac{1}{2}}} \,. \tag{5.17}$$

Phase compositions, densities, and saturations are determined from an equilibrium calculation using the Peng-Robinson equation of state[138], an accelerated successive substitution algorithm[139], and a negative flash algorithm[65]. Liquid densities are corrected using volume translation[140]. Phase viscosities are calculated using the Lohrenz-Bray-Clark correlation[141].

Fig. 5.1 shows a comparison of the one-dimensional solution obtained using 3DSL with a Courant-Friedrichs-Lewy (CFL) number of 0.5 with the solution obtained using UTCOMPciteutc93 for a 3 component displacement at 1600 psia and 160 °F . UTCOMP is an implicit-pressure, explicit-composition, isothermal, three-dimensional compositional simulator developed at the University of Texas at Austin with a third-order TVD scheme to control numerical diffusion. Except for a slight difference in the fastest front speed, the agreement is good.

5.5 Two-Dimensional Solutions

In this section we consider a three component (3C) condensing gas drive and a four component (4C) condensing-vaporizing gas drive through various heterogeneous cross sections. The aim of this

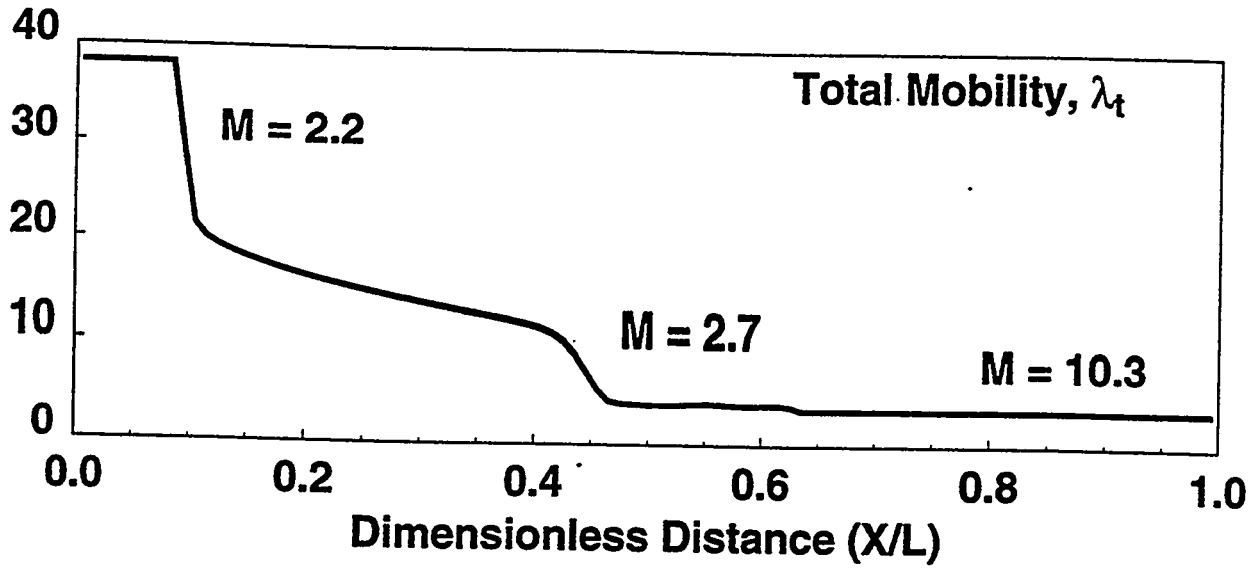

Figure 5.2: One-dimensional mobility ratio profile for the three component condensing problem of Fig. 5.1 at $t_D = 0.5$.

section is two-fold: (1) to benchmark the solutions from the streamline approach with solutions obtained from UTCOMP and (2) to highlight the ability of the streamline approach to efficiently investigate the interaction of heterogeneity, numerical resolution (number of gridblocks), phase behavior and unstable flow. The second issue has been considered by many investigators[129, 142, 126, 128, 131, 143, 144]. The recurrent difficulty faced by these studies was the limited size of the numerical problem that could be considered because of the large computational resources generally required. Stalkup[129] attempted to overcome this limitation by extrapolating his results to an infinite number of gridblocks with some success. But if one-dimensional problems are any guide to the number of gridblocks required to obtain converged solutions, it is reasonable to assume that most 2D and 3D solutions presented in the literature are probably not converged solutions – particularly for heterogeneous domains – but instead represent an intermediate solution in a sequence of refined grids. This observation is demonstrated through an example in the next section.

5.5.1 Three Component Condensing Gas Drive

The injection of pure CO_2 into a 30/70 mole percent mixture of CH_4 and C_{10} at 1600 psia and 160 °F is an example of a condensing gas drive. The corresponding 1D solution is shown in Fig. 5.1. For modeling 2D and 3D displacements, the expected nonlinearity (or instability) of the displacement can be estimated from the total mobility profile of the 1D solution. For the 3C case, Fig. 5.2 shows that the end-point mobility ratio of $M = 10.3$ is divided into a leading CO_2 front with a mobility ratio of $M = 2.7$, a rarefaction wave, and a trailing front with a mobility ratio of $M = 2.2$. Although the end-point mobility ratio is mitigated substantially by phase behavior effects alone, some nonlinearity can be expected due to the leading mobility ratio of $M = 2.7$. In addition, because the leading CO_2 shock is self-sharpening, numerical diffusion is expected to be less efficient in smearing out the mobility difference.

To investigate this displacement in 2D heterogeneous media, we considered an initial cross-section with $N_x = 62$ and $N_z = 25$ gridblocks (Fig. 5.3). Permeability varies over four orders of magnitude and has a correlation length of approximately 0.3 in the main direction of flow. A

comparison of the spatial distribution of CO_2 is shown in Fig. 5.3, and the corresponding recoveries are shown in Fig. 5.4. Both figures, Fig. 5.3 and Fig. 5.4, demonstrate that the streamline solution is in agreement with the solution given by UTCOMP. The UTCOMP solutions were found using the third-order TVD option for controlling numerical diffusion. For this problem, the streamline code (3DSL) required 0.75 hrs to generate the recovery curve up to 2 pore volumes (PV) injected, whereas UTCOMP required 18 hrs — a speed-up of approximately 24.

To further verify the 2D solution, we refined the 62×25 grid to 124×50 and to 248×100 by maintaining the same permeability distribution as the original 62×25 grid. Since the leading CO_2 shock front has an unfavorable mobility ratio and is also self-sharpening, the increased numerical resolution of the local velocity field is expected to capture the instability of the problem. Fig. 5.5 shows the comparison between UTCOMP and 3DSL for the downscaled grids. The finer 248×100 grid could not be run with UTCOMP due to prohibitively high computational costs. Three important comments can be made about the results shown in Fig. 5.5:

1. As the grid is refined, the streamline solution shows signs of instability at the leading CO_2 front due to the unfavorable mobility ratio. This demonstrates that numerical diffusion in 3DSL is minimized to the point that we are able to see the onset of a viscous-fingering like behavior at the shock front and other small scale features of the displacement.

2. The UTCOMP solution for the 124×50 also has increased resolution compared to the 62×25 solution of Fig. 5.3. But unlike the streamline solution it appears as a sharpened image of the original 62×25 grid without noticeable changes in the small scale features of the CO_2 front. This points to the problem that FD-models can require grid refinement by several powers of 2 before any noticeable change in the flow behavior can be observed. This despite higher order numerical schemes.

3. We could not simulate the 248×100 grid with UTCOMP because the computational expense was simply too high. We believe that this is not because of specific inefficiencies in UTCOMP, but rather because the underlying finite-difference scheme combined with the strong nonlinearities of the equilibrium calculations make refinement studies of the sort presented here very expensive for FD methods. In many cases studies of this sort are not possible using FD.

The speed-up of 3DSL compared to UTCOMP for the 124×50 grid was 92 (92 hrs for UTCOMP vs. 1 hr for 3DSL) to reach 2 PV injected.

5.5.2 Four Component Condensing-Vaporizing Gas Drive

The displacement of a 3C mixture of $CH_4/C_6/C_{16}$ (20/40/40) by an enriched gas mixture of CH_4/C_3 (65/35) at 2,000 psia and 200 °F exhibits a condensing behavior at the leading edge (the injected gas condenses into the resident oil) and a vaporizing behavior at the trailing edge (the injected gas volatilizes the resident oil)[74, 67]. Because the injected composition is close to the minimum enrichment composition for miscibility, the displacement can be characterized as being near-miscible[74]. Fig. 5.6 shows the 1D solution obtained using UTCOMP and 3DSL. The end-point mobility ratio for this 4C problem is $M \approx 8.4$. As a result of the near-miscible nature of the displacement, most of the mobility contrast ($M \approx 7.2$) occurs over a small region (Fig. 5.6), and thus one may expect a 2D solution to be more unstable than the 3C problem considered in the previous section. But a finer 1D solution with 500 gridblocks (Fig. 5.6) reveals that the mobility contrast of $M \approx 7.2$ in fact occurs over two rarefaction waves and a self-sharpening shock[74], with the mobility ratio across the shock being $M \approx 2$. Thus, although the two-phase region is significantly smaller than in the 3C component case, the mobility contrast is mitigate significantly

by the spreading nature of the two rarefaction waves. The instability for this displacement then is expected to be primarily due to the self-sharpening shock following the rarefaction waves.

We considered this problem in our previous work with analytical solutions along streamtubes. Because mapping analytical solutions along streamtubes overestimates the mobility contrast of a displacement, we indeed found solutions that were characterized by a very large amount of instability (long, wispy channels) as shown in Fig. 5.7. In contrast, the UTCOMP solution appeared to be characterized by a large amount of mixing resulting in a negligible mobility contrast[102].

We revisit the problem here using numerical solutions along streamlines. Fig. 5.7 shows the gas saturation maps at $t_D = 0.4$ for the three displacements. The numerical solution obtained from 3DSL is clearly different from our first solution obtained using streamtubes in that it exhibits less channeling. But the 3DSL solution is also different from the UTCOMP solution, in that there appears to be more detail in the saturation distribution and signs of some channeling, particularly due to the self-sharpening shock following the rarefaction waves. The similarity between the 3DSL and UTCOMP solutions in Fig. 5.7 shows the ability of the streamline approach to capture the compositional nature of the problem correctly. It also suggests that for this displacement, the near-miscible condition does not pose a significant problem in terms of the instability of the displacement. UTCOMP required 86 hrs to generate the saturation map shown in Fig. 5.7, whereas 3DSL required 0.6 hrs. This represents a speed-up factor of 143.

5.5.3 Sensitivity on Injected Composition.

The speed and accuracy of the streamline approach clearly offers unique opportunities to revisit outstanding problems in predicting the effectiveness of enriched gas injection in heterogeneous media as a way to enhance production of hydrocarbons. As an example, we consider the sensitivity of the 4C condensing-vaporizing displacement on the level of enrichment of the injected mixture. This is a relevant questions since increasing enrichment will lower the residual oil saturation and increase the local contact efficiency, but at the same time may cause bypassing and early breakthrough due to the unstable nature of the displacement. Finding the optimal level of enrichment, that will maximize oil recovery for a given description of the phase behavior and geological setting entails many forward simulations with sufficient geological and numerical resolution. We emphasize that the solution to such an exercise will depend strongly on the physical scale of the problem and the resulting interaction of viscous, gravity, capillary, and diffusive forces at that scale[124, 123, 125]. Since we are neglecting gravity, capillary, and diffusive mechanisms here, the results are meant primarily to demonstrate the efficiency of the streamline approach, rather than to reveal any novel physical insight.

Fig. 5.8 shows the result of the sensitivity exercise through a 128×64 permeability field with 5 orders of magnitude difference in permeability. The three injection compositions mixtures of CH_4/C_3 — (85/15), (65/35), and (45/55) mole percent — represent immiscible, MCM, and FCM displacements respectively of the initial oil composition. We also used a simple linear interpolation for the relative permeabilities to account for the fact that as the displacement goes from immiscibility to miscibility the relative permeabilities tend to straight lines and the residual saturations go to zero. For this particular example, Fig. 5.8 shows that injection of a CH_4/C_3 mixture that achieves first-contact miscibility with the resident oil will be the most efficient displacement. We believe that the primary reason for this is that in particular this case reservoir heterogeneity has a first order effect compared to displacement instabilities. It is the geology that is dictating the primary channels of the solvent. The cumulative simulation time for the three cases on a standard workstation was 16 hrs.

5.6 Three Dimensional Solution

In the previous sections we studied cross-sectional models. However, due to the decoupling of fluid transport from the underlying geological grid, the streamline method is ideally suited for large, 3D, multiwell models dominated by heterogeneity. Because of grid CFL constraints, these problems are particularly difficult for conventional FD methods.

As a result, the streamline approach offers unique opportunities to model field-scale problems with an acceptable level of geological resolution. Although upscaling will still be necessary to go from the fine-scale earth models of $\mathcal{O}(\infty/10^{-3})$ gridblocks to the reservoir simulation scale of $\mathcal{O}(\infty/10^{3-7})$, the level of upscaling required will be significantly less for simulations using streamlines.

As an example, we simulated the 4C problem discussed in the previous section on a $180 \times 180 \times 16 = 518,400$ heterogeneous Cartesian grid with a total of 36 wells for a period of 0.7 PVs injected. The average pressure gradient between injectors and producers was $\Delta P \approx 180$ psia. The simulation run required approximately 3 days on a standard workstation (DEC AlphaServer 2100 4/275 with 256MB of RAM). Although there are only 30 gridblocks between wells for this half-million gridblock example, it is a significant improvement in resolution compared to the limited number of gridblocks usually used in FD field-scale models. Fig. 5.9 shows recovery and breakthrough curves for C_3 obtained using UTCOMP and Eclipse 300[145] (E300). The upscaled $60 \times 60 \times 8$ model was generated from the fine-scale $180 \times 180 \times 16$ model using simple geometric averaging of the absolute permeabilities. More sophisticated upscaling techniques may have reduced the difference between fine-scale and coarse-scale results[113, 114]. Fig. 5.9 is a reminder that the difference in the solution due to upscaling of the geological model, pseudoization of the phase behavior, and the usually low numerical resolution between wells poses a challenging problem for traditional FD approaches for modeling field-scale compositional problems. Streamlines may offer a simple yet effective solution to increase the geological detail and resolution between wells using a fraction of the computational costs required by FD. As we show in the following section, the streamline approach may in fact allow to model problems that are beyond current hardware capabilities for FD methods. For this example, solution of the $60 \times 60 \times 8 = 28,800$ model with E300 required approximately the same CPU time as the $180 \times 180 \times 16 = 518,400$ model with 3DSL. We estimated the runtime for the $180 \times 180 \times 16$ model with Eclipse in the tens of years (Fig. 5.10).

5.7 Timing and Scaling

In our previous work[103, 106] we found speed-up factors between 10 and 500 for waterflooding and FCM displacements in 2D and 3D heterogeneous domains and under a variety of flow conditions, geological descriptions, and boundary conditions. In most cases, the speed-up resulted from the reduced number of global pressure solves and large convective steps allowed by 3DSL.

Fig. 5.10 shows scaling results we found for the 3D, 4C problem described previously. We generated Fig. 5.10 by starting with the fine-scale model of $180 \times 180 \times 16$ and then considered upscaled models $60 \times 60 \times 8$, $45 \times 45 \times 8$, and $36 \times 36 \times 8$. We could only run the later three models with E300 using our available computational resources. For comparison, we also show the scaling of 3DSL on the same 3D problem for a waterflood. Although the results in Fig. 5.10 are specific to the example we studied, they show that the streamlines solutions scale near-linearly with the number of gridblocks, N_{gb}, whereas the FD solution obtained with Eclipse 300 scales approximately as $N_{gb}^{3.4}$.

The scaling behavior of each method can be explained qualitatively by considering the expression for the total run time, T, given by

$$T = N_{ts} \times \Delta t_{ts} \ , \tag{5.18}$$

where N_{ts} is the number of timesteps and Δt_{ts} is the time required per timestep. Δt_{ts} is the sum of the time required to invert the pressure matrix, Δt_p, and the time to move the saturation/concentration forward in time, Δt_S. It is reasonable to assume that for each method, Δt_{ts}, is roughly the same and with a near linear scaling. For example, our public-domain multigrid[146] solver scales near-linearly, $\Delta t_p \propto N_{gb}^{1.3}$.

The efficiency of the streamline approach compared to FD is derived from the fact that the number of global timesteps, N_{ts}, is independent of the number of gridblocks of the system, because fluid transport is decoupled from the underlying grid. Instead, it is directly related to the nonlinearity of the problem (mobility contrast/gravity number) and the number of well-events (changing boundary conditions). A good example of this is tracer flow, where for constant boundary conditions, only a single global timestep is required, irrespective of the level of heterogeneity and the number of gridblocks. The reason that the magnitude of heterogeneity is irrelevant is because the 1D solution along the streamline is homogeneous, with all the heterogeneity buried in the TOF.

A finite-difference code, on the other hand, must take many timesteps that are directly dictated by the size of the gridblocks and the magnitude of the heterogeneity present. It is probably the changing level of heterogeneity (higher extremes of permeability with increasing grid resolution) that causes the cubic scaling exhibited by the FD code in Fig. 5.10. For homogeneous systems, the number of timesteps in FD are expected to scale linearly with N_{gb}. But as heterogeneity is added to the model, finer grids with higher permeability contrasts will cause the number of timesteps to scale with a power greater than one. Assuming a near-linear scaling for the pressure solution and the explicit timestepping, combined with a quadratic scaling of the number of timesteps would explain the $N_{gb}^{3.4}$ seen in Fig. 5.10 for the FD code.

5.8 Conclusions

We have extended the streamline approach to 2D and 3D compositional displacements by using a general 1D numerical solver along streamlines. The 1D solution accounts for compressibility and volume-change-on-mixing by solving for the total velocity. The advantages of using streamlines for two-phase immiscible as well as FCM displacements are amplified for compositional displacements:

1. By decoupling the 1D transport problem from the underlying geological grid, streamlines allow to retain the numerical accuracy required to model compositional displacements.

2. The streamline approach scales near-linearly with the number of gridblocks, which represents a considerable improvement over conventional FD methods.

3. The efficiency of the streamline approach offers a unique opportunity to revisit outstanding questions for designing field-scale enhanced-recovery processes.

4. Higher geological and numerical resolution reduces the number of scales that need to be crossed when going from the fine-scale earth model to the reservoir simulation model, thereby reducing the dependence on upscaling of absolute and relative phase permeabilities. This will lead to a significant improvement in the resolution of the transport problem and to more reliable predictions.

5. The increased numerical efficiency can be translated to a higher number of pseudocomponents for the description of the phase behavior, larger models, and better geological resolution.

5.9 Nomenclature

C_i = total moles of component i
F_i = molar flux of component i
f_j = fractional flow of phase j, dimensionless
$\vec{\vec{K}}$ = absolute permeability tensor, L^2
k = node index for finite-difference scheme
k_{rj} = relative permeability of phase j, dimensionless
M = mobility ratio, dimensionless
n_c = number of components
n_p = number of phases
N_{gb} = number of total gridblocks
N_{ts} = number of global time steps
n = time step level in finite-difference formulation
P = Pressure M/T^2L
PV = pore volumes, L^3
r = ratio of successive flux differences
S_j = saturation of phase j, dimensionless
s = spatial distance coordinate along a streamline, L
t = time, T
t_D = dimensionless time
$\vec{u}_t$ = total Darcy velocity, L/T
u_D = dimensionless total velocity
$x_{i,j}$ = mole fraction of component i in phase j, dimensionless
z_i = total mole fraction of component i, dimensionless
Δt = time step size in 1D solution, T
Δt_p = CPU time required per global pressure solution, T
Δt_S = CPU time required per global convective step, T
Δt_{ts} = CPU time required per global time step, T
Φ = van Leer limiter for TVD scheme
ϕ = porosity, dimensionless
ρ_j = density of phase j, M/L^3
ζ = local streamline coordinate, L
λ_t = total mobility, L^3T/M
τ = time of flight, T
μ_j = viscosity of phase j, M/TL

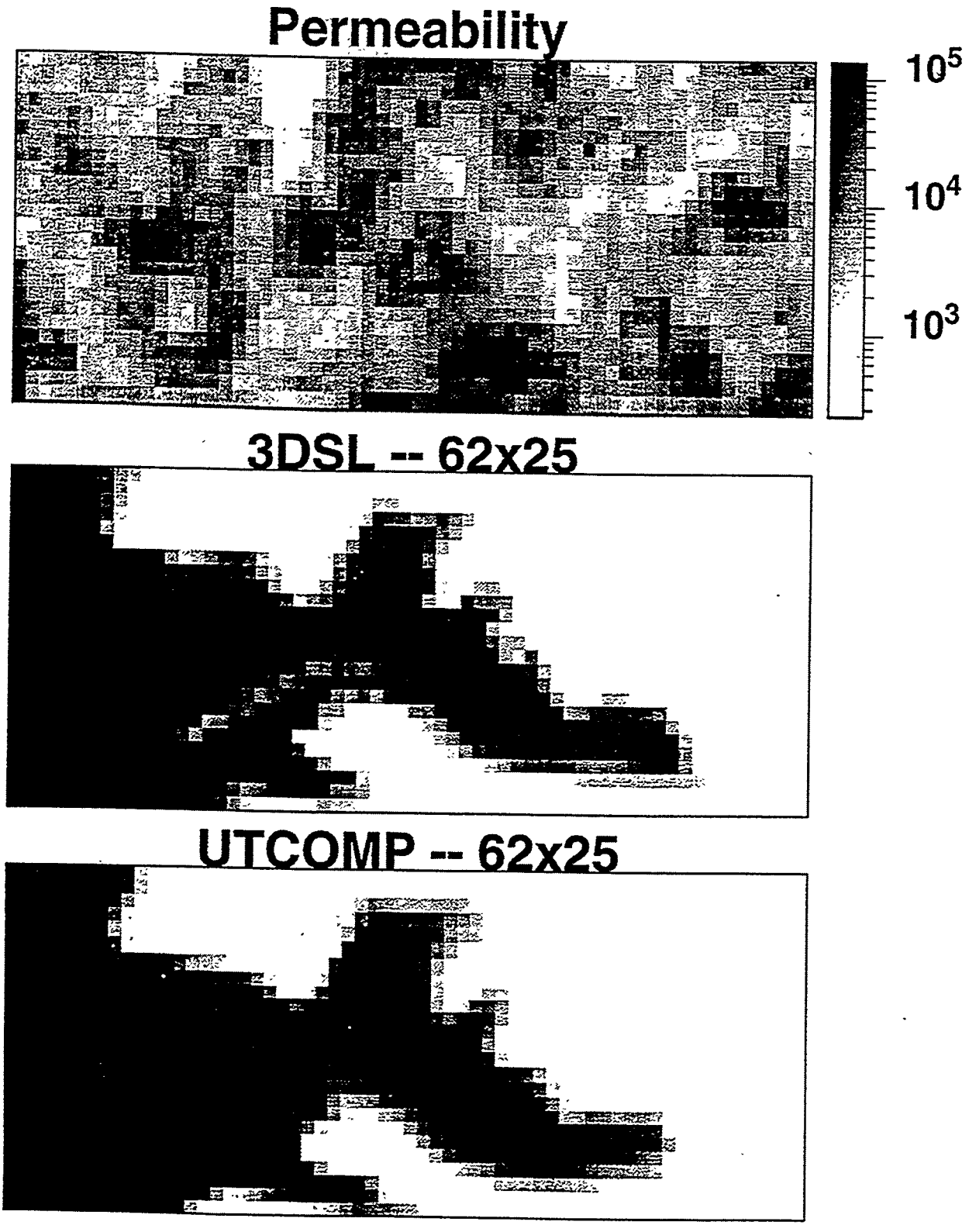

Figure 5.3: Permeability field (62×25) and spatial distribution of CO_2 for 3DSL and UTCOMP at $t_D = 0.5$.

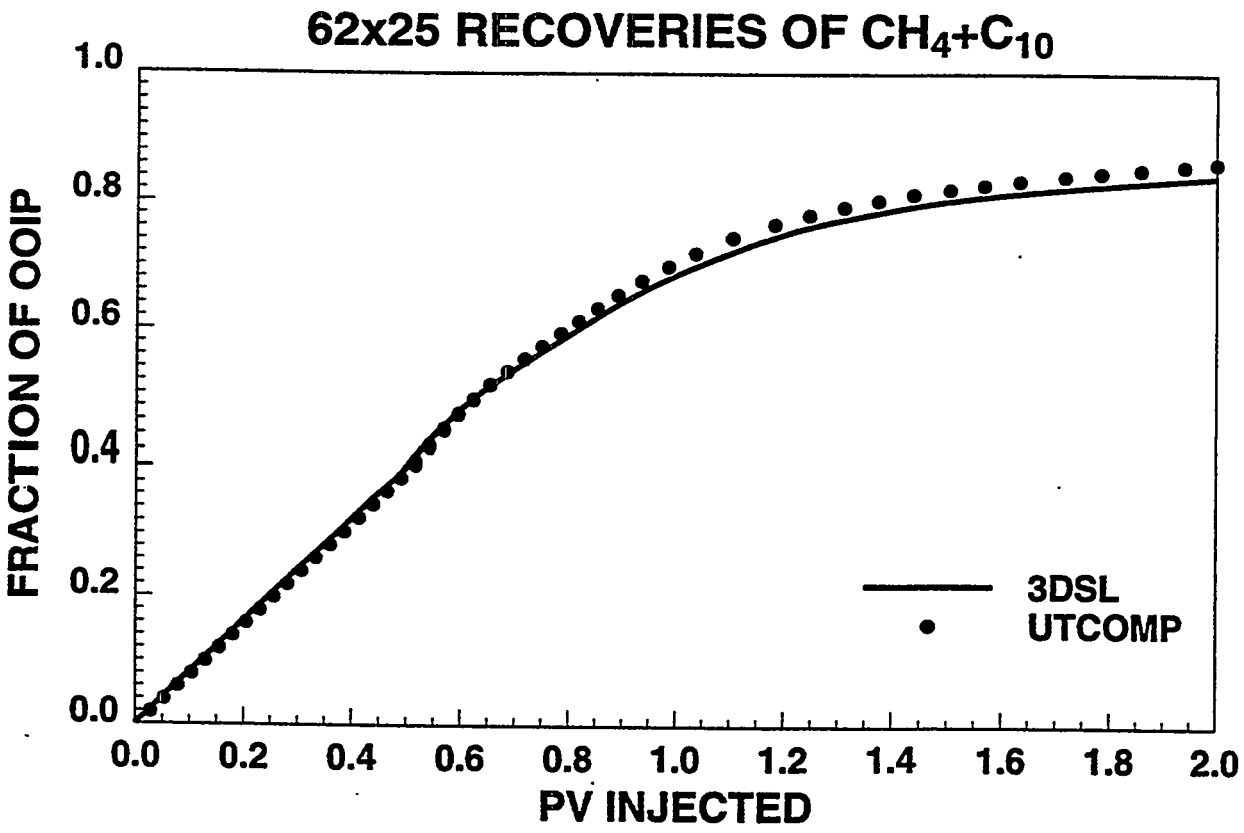

Figure 5.4: Cumulative recoveries of CH_4 plus C_{10} for 3DSL and UTCOMP.

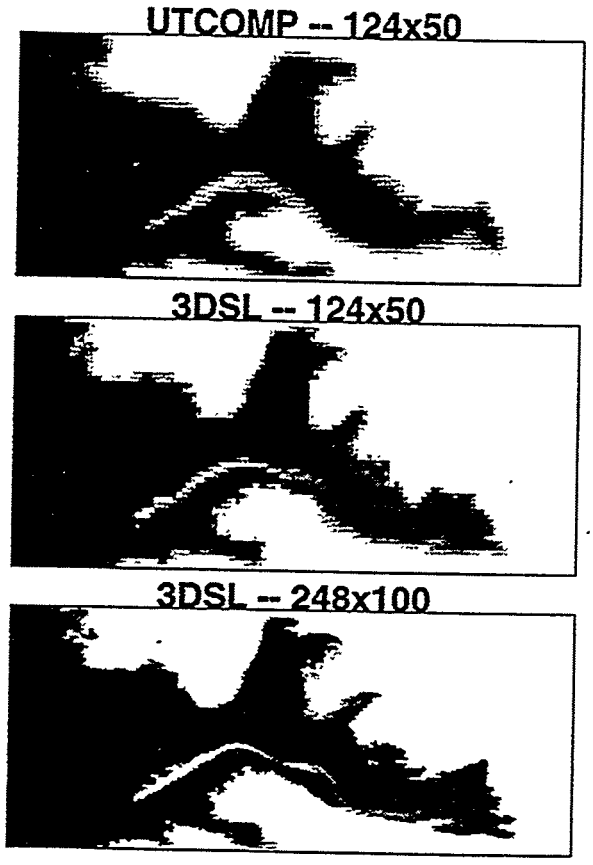

Figure 5.5: Spatial distribution of CO_2 for 3DSL at $t_D = 0.5$ for grids 124×50 and 248×100 compare to the UTCOMP solution for grid 124×50.

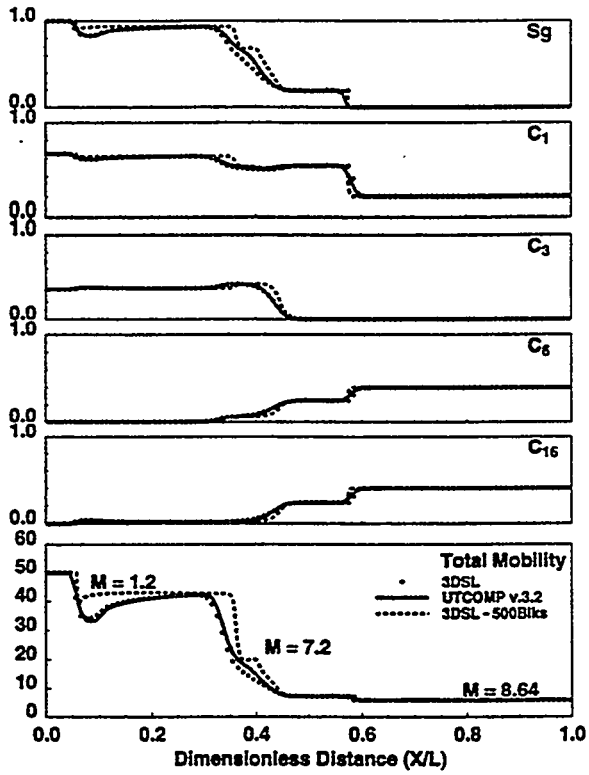

Figure 5.6: One-dimensional, TVD solution with 100 gridblocks using UTCOMP (v.3.2 w/ automatic time stepping) and TVD solutions with 100 and 500 gridblocks using 3DSL (CFL=0.25) for CH_4/C_3 (65/35) injection into a 20/40/40 mixture of $CH_4/C_6/C_{16}$ at 2000 psia and 160^{circ}F.

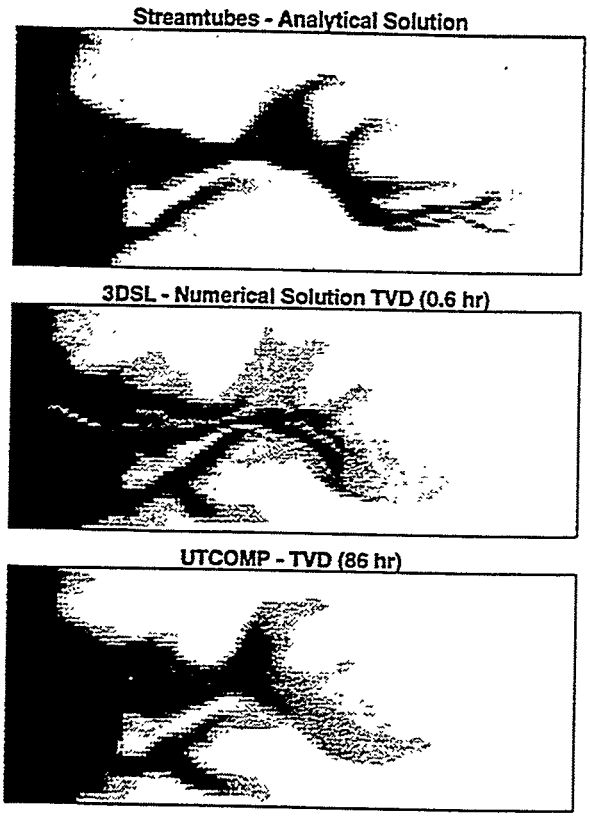

Figure 5.7: Saturations maps at $t_D = 0.4$ for the displacement of a 20/40/40 mixture of $CH_4/C_6/C_{16}$ at 2000 psia and 160°F by a 65/35 mixture of CH_4/C_3 through a heterogeneous cross-section with 125×50 gridblocks.

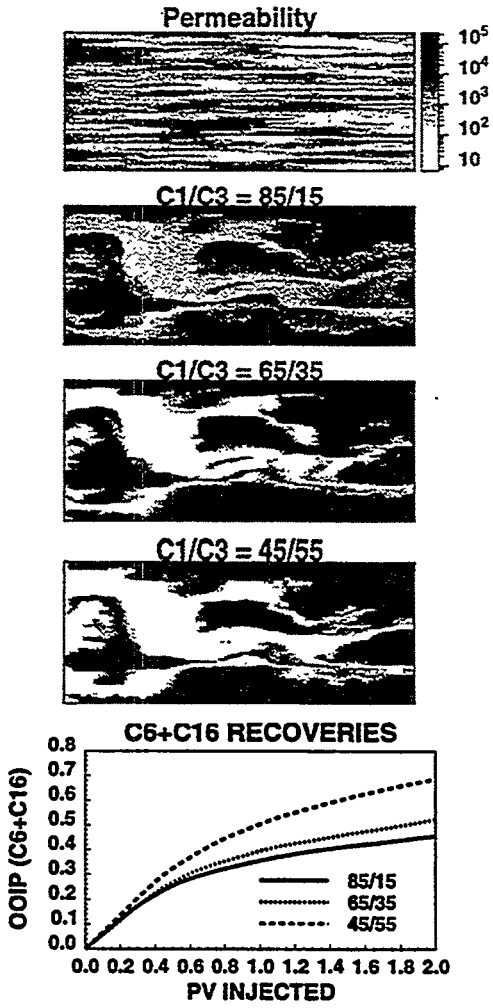

Figure 5.8: Sensitivity of the displacement of a 20/40/40 mixture of $CH_4/C_6/C_{16}$ at 2000 psia and 160^{circ}F on the enrichment level of the injected mixture of CH_4/C_3 . The permeability field has 5 orders of magnitude difference in permeability. The maps show spatial distribution of C_3 . Recoveries are for C_6 plus C_{16} .

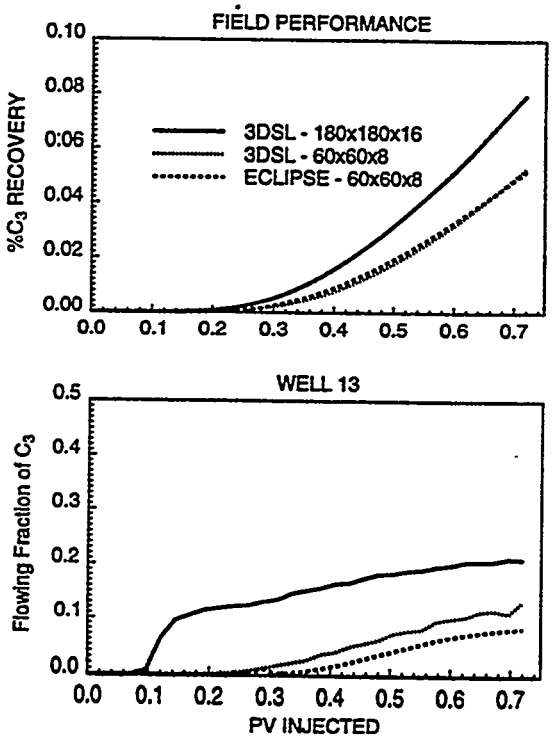

Figure 5.9: 3D solutions with $180 \times 180 \times 16 = 518,400$ gridblocks and with $60 \times 60 \times 8 = 28,800$ gridblocks for the 4C problem of Fig. 5.6.

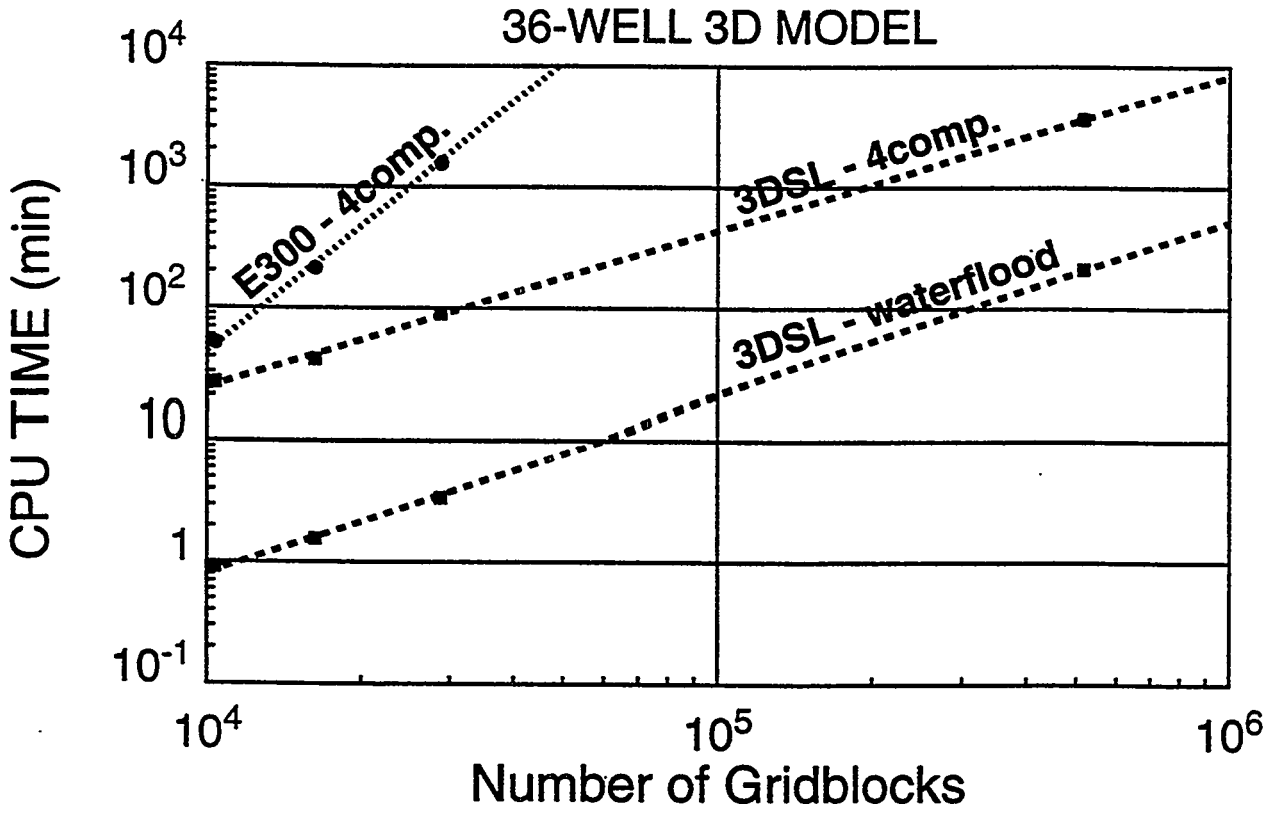

Figure 5.10: Scaling of compositional solution.

References

[1] Dumoré, J. M. and Schols, R. S.: "Drainage Capillary Functions and the Influence of Connate Water, *SPE Journal*, **14** 437-444, 1974.

[2] Kantzas, A., Chatzis, I., and Dullien, F. A. L.: "Enhanced Oil Recovery by Inert Gas Injection," paper SPE 13264 proceedings of the Sixth SPE/DOE Symposium on Enhanced Oil Recovery, Tulsa, OK, April, 1988.

[3] Kalaydjian, F. J.M., Moulu, J.C., Vizika, O., and Munkerud, P. K.: "Three Phase Flow in Water-Wet Porous Media: Determination of Gas/Oil Relative Permeabilities Under Various Spreading Conditions" paper SPE 26671 proceedings of the 68th Annual Technical Conference and Exhibition of the SPE, Houston, TX, October, 1993.

[4] Zhou, D., and Blunt, M. J.: "Effect of Spreading Coefficient on the Distribution of Light Non-Aqueous Phase Liquid in the Subsurface," *Journal of Contaminant Hydrology*, **25** 1-19, (1997).

[5] Blunt, M. J., Zhou, D., and Fenwick, D. H.: "Three Phase Flow and Gravity Drainage in Porous Media," *Transport in Porous Media*, **20** 77-103 (1995).

[6] Jerauld, G. R.: "Prudhoe Bay gas/oil relative permeability," *SPE Reservoir Engineering*, **12** 66-73, Feb 1997.

[7] Espie, A. A., Brown, C. E., Narayanan, K. R., and Wilcox, T. C.: "A Laboratory Investigation of Gravity Drainage/Waterflood Interaction in Prudhoe Bay," paper SPE 28614 proceedings of the 1989 69th Annual Technical Conference and Exhibition, New Orleans, LA.

[8] Keller, A. A., Blunt, M. J., and Roberts, P. V.: "Micromodel Observation of the Role of Oil Layers in Three Phase Flow," *Transport in Porous Media*, **20** 105-133, 1997.

[9] Soll, W. E., M. A. Celia, and J. L. Wilson.: "Micromodel studies of three-fluid porous media systems: Pore-scale processes relating to capillary pressure - saturation relationships." *Water Resources Research*, **29**(9) 2963-2974, 1993.

[10] Øren, P. E., J. Billiote and W. V. Pinczewski.: "Mobilization of waterflood residual oil by gas injection for water wet conditions." *SPE Formation Evaluation*,**7** 70-78, March 1992.

[11] Chatzis, I., A. Kantzas, and F. A. L. Dullien.: "On the investigation of gravity inert gas injection using micromodels, long berea cores, and computer assisted tomography," paper SPE 18284 proceedings of the 1988 63rd Annual Technical Conference and Exhibition of the SPE, Houston, TX, October.

[12] Øren, P. E. and W. V. Pinczewski.: "Fluid distribution and pore scale displacement mechanisms in drainage dominated three phase flow." *Transport in Porous Media*, **20** 105-133, 1995.

[13] Zhou, D., M. J. Blunt, and F. M. Orr, Jr.: "Hydrocarbon drainage along corners of noncircular capillaries." *Journal of Colloid and Interface Science*, **187** 11-21, 1997.

[14] Dong, M., F. A. L. Dullien, and I. Chatzis.: "Imbibition of oil in film form over water present in edges of capillaries with an angular cross-section." *J. Colloid and Interface Sci.*,**172** 278-288, December 1995.

[15] Fenwick, D. H., and Blunt, M. J.: "Calculating Three-Phase Relative Permeabilities Using Network Modeling", proceedings of the 5th European Conference on the Mathematics of Oil Recovery, Leoben, Austria, 3-6 Sept. 1996.

[16] Fenwick, D. H., and Blunt, M. J.: "Network Modeling of Three-Phase Flow in Porous Media," *SPE Journal*, **3**:86-97, 1998.

[17] Fenwick, D. H., and M. J. Blunt.: "Three-dimensional modeling of three phase imbibition and drainage" *Advances in Water Resources* **21** 121-144 (1998).

[18] Soll, W. E., and M. A. Celia.: "A modified percolation approach to simulating three-fluid capillary pressure-saturation relationships". *Advances in Water Resources* **16** 107-26 (1993).

[19] Mani, V. and Mohanty, K. K.: "Pore-Level Network Modeling of Three-Phase Capillary Pressure and Relative Permeability Curves," paper SPE 38883 proceedings of the SPE Annual Technical Conference and Exhibition, San Antonio, Texas, Oct. 1997.

[20] Øren, P. E., J. Billiote, and W. V. Pinczewski.: "Pore-scale network modeling of waterflood residual oil recovery by immiscible gas flooding," paper SPE 27814 proceedings of the 1994 Improved Oil Recovery Symposium, Tulsa, OK, April.

[21] Heiba, A. A., H. T. Davis, and L. E. Scriven.: "Statistical network theory of three-phase relative permeabilities," paper SPE 12690 proceedings of the 1984 4th DOE/SPE Symposium on Enhanced Oil Recovery, Tulsa, OK, April.

[22] Pereira, G. G., W. V. Pinczewski, D. V. C. Chan, L. Paterson and P. E. Øren.: "Pore-scale network model for drainage dominated three-phase flow in porous media." *Transport in Porous Media* **24** 167-201, 1996.

[23] Vizika, O., and Lombard, J. M.: "Wettability and Spreading: Two Key Parameters in Oil Recovery With Three-Phase Gravity Drainage," *SPE Reservoir Engineering* **11**, p 54-60, February 1996.

[24] Skurdal, H., Hustad O. St., and Holt, T.: "Oil Recovery by Gravity Drainage during Gas Injection," proceeding of the 8th European IOR - Symposium in Vienna, Austria, May 15-17, 1995.

[25] Naylor, P., Sargent, N. C., Crosbie, A. J., Tilsed A. P., Goodyear S. G.: "Gravity Drainage during Gas Injection," proceedings of the 8th European IOR-Symposium in Vienna, Austria, May 15-17, 1995.

[26] Skauge, A., Eleri, O. O., Graue, A., and Monstad, P.: "Influence of Connate Water on Oil Recovery by Gravity Drainage," paper SPE 27817 proceedings of the SPE/DOE Ninth Symposium on Improved Oil Recovery, Tulsa, OK, U.S.A., April 17-20, 1994.

[27] Virnovsky, G. A.: "Determination of Relative Permeabilities in Three-Phase Flow in a Porous Medium," *Izv. Akad. Nauk SSSR, Mekh. Zhidk. Gaza* (1984) **5**, 187-189.

[28] Grader, A. S., and D. J. O'Meara Jr.: "Dynamic Displacement Measurements of Three-Phase Relative Permeabilities Using Three Immiscible Liquids," paper SPE 18293 proceedings of the SPE Annual Technical Conference and Exhibition of the Society of Petroleum Engineers, Houston, TX, October 2-5, 1988.

[29] Welge, H. J.: "Displacement of Oil from Porous Media by Water and Gas," *Trans., AIME* (1950) **198**, 314-316.

[30] Johnson, E. F., Bossler, D. P., and Naumann, V. O.: "Calculation of Relative Permeability from Displacement Experiments," *Trans., AIME* (1959) **216**, 370.

[31] Siddiqui, S., Hicks, P. J., Grader, A. S.: "Verification of Buckley Leverett Three Phase Theory Using Computerized Tomography," *J. Pet. Sci. Eng.* (1996) **15**(1), pp. 1-21.

[32] Sarem, A. M.: "Three-Phase Relative Permeability Measurements by Unsteady-State Method," *Soc. Pet. Eng. J.*, (Sept. 1966) **6**, 199-205.

[33] Oak, M. J., Baker, L. E., and Thomas, D. C.: "Three Phase Relative Permeability of Berea Sandstone," *Journal of Petroleum Technology*, **42** (1990) 1057-1061.

[34] Nordtvedt, J. E., E. Ebeltoft, J. E. Iverson, A. Sylte, H, Urkedal, K. O. Vatne, and A. T. Watson.: "Determination of three-phase relative permeabilities from displacement experiments," paper SPE 36683 proceedings of the 1996 Annual Technical Conference and Exhibition, Denver, CO, October.

[35] Akin, S., Demiral, M. R. B.: "Effect of Flow Rate on Imbibition Three-Phase Relative Permeabilities and Capillary Pressure", paper SPE 38897 proceedings of the 1997 SPE Annual Technical Conference and Exhibition, San Antonio, Texas, 5-8 October 1997.

[36] Fayers, F. J.: "Extension of Stone's Method 1 and conditions for real characteristics in three phase flow," *Soc. Pet. Eng. Res. Eng.* , 4 (1989) 437-445.

[37] Parker, J. C., Lenhard, R. J., and Kuppusamy, T.: "A Parametric Model for Constitutive Properties Governing Multiphase Flow in Porous Media," *Water Resources Research*, **23** (1987) 618-624.

[38] Stone, H. L.: "Probability Model for Estimation Three-Phase Relative Permeability," *Journal of Petroleum Technology*, **20** (1970) 214-218.

[39] Stone, H. L.: "Estimation of Three-Phase Relative Permeability and Residual Data," *Journal of Canadian Petroleum Technology*, **12** (1973) 53-61.

[40] van Genuchten, M. T.: "A Closed-form Equation for Predicting the Hydraulic Conductivity of Unsaturated Soils," *Soil Science Society of American Journal*, **44** (1980) 892-898.

[41] Corey, A. T., Rajthens, C. H., Henderson, J. H., and Wyllie, M. R. J.: "Three Phase Relative Permeability Models," *Trans., AIME* (1956) **207**, 349-351.

[42] Baker, L. E.: "Three Phase Relative Permeability Correlations," paper SPE 17369 proceedings of the 1988 Sixth SPE/DOE Symposium on Enhanced Oil Recovery, Tulsa, OK, April.

[43] Delshad, M., and Pope, G. A.: "Comparison of the Three Phase Oil Relative Permeability Models," *Transport in Porous Media*, **4** (1989) 59-83.

[44] Fayers, F. J. and Matthews, J. D.: "Evaluation of Normalized Stone's Methods for Estimating Three-Phase Relative Permeabilities," *Soc. Pet. Eng. J* **24** (April 1984) 224-232.

[45] Honarpour, M. M., Cromwell, V., Hatton, D. and Satchwell, R.: "Reservoir Rock Descriptions Using Computed Tomography (CT)," paper SPE 14272 proceedings of the 60th SPE Annual Technical Conference and Exhibition of the Society of Petroleum Engineers, Las Vegas, Sept. 22-25, 1985.

[46] Wellington, S. L., and Vinegar, H. J.: "X-Ray Computerized Tomography," *Journal of Petroleum Technology* (Aug. 1987), 885-898.

[47] Hicks, P. J. Jr.: "X-Ray Computer Assisted Tomography for Laboratory Core Studies," *Journal of Petroleum Technology* (Dec. 1996), 1120-1122.

[48] MacAllister, D. J., K. C. Miller, S. K. Graham and C-T Yang.: "Application of X-Ray CT Scanning to the Determination of Gas Water Relative Permeabilities," paper SPE 18284 proceedings of the 1990 65th Annual Technical Conference and Exhibition, New Orleans, LA, September.

[49] Adamson, A. W.: *Physical Chemistry of Surfaces*, fifth edition, John Wiley and Sons, New York (1990).

[50] Goodyear, S.G., and P. I. R. Jones.: "Relative permeabilities for gravity stabilized gas injection," proceedings of the 1995 8th European Symposium on Improved Oil Recovery, Vienna, Austria, May.

[51] Buckley, J. S., Liu, Y., Xie, X., and Morrow, N. R.: "Asphaltenes and Crude Oil Wetting - The Effect of Oil Composition," *SPE Journal*, **2** 107-119, 1997.

[52] Larsen, J. A., and Skauge, A.:"Methodology for Numerical Simulation with Cycle-Dependent Relative Permeabilities," *SPE Journal*, **3**:163-173, 1998.

[53] Lombard, J. M., and Lenormand, R.: "Fractional Wettability and Petrophysical Parameters of Porous Media," in *Advances in Core Evaluation III Reservoir Management*, P. F. Worthington and C. Chardaire-Riviere Editors, Gordon and Breach Science Publishers, Amsterdam 1993.

[54] Sahni, A., Burger, J. E., and Blunt, M. J.: "Measurement of Three Phase Relative Permeability during Gravity Drainage using CT Scanning," paper SPE 39655 proceedings of the SPE/DOE Improved Oil Recovery Symposium, Tulsa, Oklahoma, April 1998.

[55] Sahni, A.: "Measurement of Three-Phase Relative Permeability During Gravity Drainage Using CT Scanning", Ph.D. Dissertation, Stanford University, 1998.

[56] Skauge, A., and Larsen, J. A.:"Three-Phase Relative Permeabilities and Trapped Gas Measurements Related to WAG Processes," proceedings of the 1994 International Symposium of The Society of The Core Analysts, Savanger, Norway, September 1994.

[57] Stone, H. L.: "Probability Model for Estimating Three-Phase Relative Permeability," *J. Pet. Tech.*:214-218,(Feb. 1970); *Trans., AIME,***249**, 1970.

[58] Zhou, D., Blunt, M. J., and Orr, Jr., F. M.: "Effect of Wettability on Three-Phase Distributions," proceedindings of The 4th International Symposium on Evaluation of Reservoir Wettability and its Effect on Oil Recovery, Montpellier, France (1996); "Wettability Effects in Three-Phase Gravity Drainage," *J. Pet. Sci. and Eng.*, **20**:203-211, 1998.

[59] Hutchinson, C.A. Jr. and Braun, P.H.: "Phase Relations of Miscible Displacement in Oil Recovery", *A.I.Ch.E. J.* (March, 1961), 64-72.

[60] Benham, A.L., Dowden, W.E. and Kunzman, W.J.: "Miscible Fluid Displacement - Prediction of Miscibility", *Trans. AIME*, (1959) **216**, 388-398.

[61] Metcalfe, R.S., Fussell, D.D., and Shelton, J.L.: "A Multicell Equilibrium Separation Model for the Study of Multiple Contact Miscibility in Rich Gas Drives", *SPEJ*, (1973) **13**, No.3, 147-155.

[62] Kuo, S.S.: "Prediction of Miscibility for the Enriched-Gas Drive Process", paper SPE 14152 presented at the 1985 SPE Annual Technical Conference and Exhibition, Las Vegas, NV.

[63] Luks, K.D., Turek, E.A. and Baker, L.E.: "Calculation of Minimum Miscibility Pressure", *SPE Res. Eng.*, (Nov. 1987), 501-506.

[64] Nouar, A., Flock, D.L.: "Prediction of the Minimum Miscibility Predictions of a Vaporizing Gas Drive", paper SPE 15075 presented at the 56th California Regional Meeting of the SPE, Oakland, CA, 1986.

[65] Whitson, C. and Michelsen, M.L.: "The Negative Flash," *Fluid Phase Equilibria*, (1989) **53**, 51-71.

[66] Wang, Y. and Orr, F.M., Jr.: "Analytical Calculation of Minimum Miscibility Pressure", *Fluid Phase Equilibria*, (1997), in press.

[67] Zick, A.A.: "A Combined Condensing/Vaporizing Mechanism in the Displacement of Oil by Enriched Gas", paper SPE 15493 presented at the 1986 SPE Annual Technical Conference and Exhibition, New Orleans, LA.

[68] Stalkup, F.I.: "Displacement Behavior of the Condensing/Vaporizing Gas Drive Process", paper SPE 16715 presented at the 1987 SPE Annual Technical Conference and Exhibition, Dallas, TX.

[69] Jensen, F. and Michelsen, M.L.: "Calculation of First Contact and Multiple Contact Minimum Miscibility Pressures", *In Situ*, (1990) **14**, No.1, 1-17.

[70] Neau, E., Avaulee, L. and Jaubert, J.N.: "A New Algorithm for Enhanced Oil Recovery Calculations", *Fluid Phase Equilibria*, (1996) **117**, 265-272.

[71] Pederson, K.S., Fjellerup, J., Thomassen, P. and Fredenslund, A.: "Studies of Gas Injection into Oil Reservoirs by a Cell-to-Cell Simulation Model", paper SPE 15599 presented at the 1986 SPE Annual Technical Conference and Exhibition, New Orleans, LA.

[72] Monroe, W.W., Silva, M.K., Larsen, L.L. and Orr, F.M., Jr.: "Composition Paths in Four-Component Systems: Effect of Dissolved Methane on 1D CO_2 Flood Performance", *SPE Res. Eng.*, (1990) **5**, 423-432.

[73] Orr, F.M., Jr. and Silva M.K.: "Effect of Oil Composition on Minimum Miscibility Pressure - Part 2: Correlation", *SPE Res. Eng.*, (1987) **2**, 479-491.

[74] Johns, R.T., Dindoruk, B. and Orr, F.M., Jr.: "Analytical Theory of Combined Condensing/Vaporizing Gas Drives", *SPE Adv. Tech. Ser.* (1993) **2**, No. 3, 7-16.

[75] Dindoruk, B., Orr, F.M., Jr. and Johns, R.T.: "Theory of Multicontact Miscible Displacement with Nitrogen", *SPEJ*, (1997) **2**, No.3, 268-279.

[76] Johns, R.T. and Orr, F.M., Jr.: "Miscible Gas Displacement of Multicomponent Oils", *SPEJ*, (1996) **1**, No.1, 39-50.

[77] Mehra, R.K., Heidemann, R.A. and Aziz, K.: "An Accelerated Successive Substitution Algorithm", *The Canadian J. of Chem. Eng.*, (Aug. 1983) **61**, 590-596.

[78] Hearn, C.L. and Whitson, C.H.: "Evaluating Miscible and Immiscible Gas Injection in the Sarah Field, Oman", paper SPE 29115 presented at the 13th SPE Symposium on Reservoir Simulation, 1995, San Antonio, TX.

[79] Jessen, K., Bleriot, L., Michelsen, M.L. and Stenby, E.: "Calculation of MMP", International Conference on Production of Reservoir Fluids in Frontier Conditions, Rueil-Malmaison, France, Dec. 4-5, 1997.

[80] Muskat, M. and Wyckoff, R.D.: "A Theoretical Analysis of Waterflooding Networks," *Trans. AIME*, **107**, 62-77, 1934.

[81] Muskat, M.: "Flow of Homogeneous Fluids," International Human Resources Development Corporation, 137 Newbury Street, Boston MA 02116, 1937, 1982.

[82] Muskat, M.: "The Theory of Potentiometric Models," *Trans. AIME*, **179**, 216-221, 1948.

[83] Fay, C.H. and Prats. M.: "The Application of Numerical Methods to Cycling and Flooding Problems," Proceedings of the 3rd World Petroleum Congress, The Hague, Sect. II, 555, 1951.

[84] Higgins R.V. and Leighton, A.J.: "A Computer Method to Calculate Two–Phase Flow in Any Irregularly Bounded Porous Medium," *Journal of Petroleum Technology*, **14(6)**, 679-683, 1962.

[85] Higgins R.V. and Leighton, A.J.: "Computer Prediction of Water Drive of Oil and Gas Mixtures Through Irregularly Bounded Pororus Media — Three-Phase Flow," *Journal of Petroleum Technology*, **14(9)**, 1048-1054, 1962.

[86] Higgins, R.V., Boley, D.W., and Leighton, A.J.: "Aids to Forecasting The Performance of Water Floods," *Journal of Petroleum Technology*, **16**, 1076-1082, 1964.

[87] Parsons, R.W.: "Directional Permeability Effects in Developed and Unconfined Five-Spots," *Journal of Petroleum Technology*, **24**, 487-494, 1972.

[88] Martin, J.C. and Wegner, R.E.: "Numerical Solution of Multiphase, Two-Dimensional Incompressible Flow Using Streamtube Relationships," *Society of Petroleum Engineers Journal*, **19**, 313-323, 1979.

[89] Bommer, M.P. and Schechter, R.S.: "Mathematical Modeling of In-Situ Uranium Leaching," *Society of Petroleum Engineers Journal*, **19**, 393-400, 1979.

[90] Lake, L.W., Johnston, J.R., and Stegemeier, G.L.: "Simulation and Performance Prediction of a Large-Scale Surfactant/Polymer Project," *Society of Petroleum Engineers Journal*, **21**, 731-739, 1981.

[91] Mathews, J.L., Emanuel, A.S., and Edwards, K.A.: "Fractal Methods Improve Mitsue Miscible Predictions," *Journal of Petroleum Technology*, **41**, 1136-1989, 1989.

[92] Emanuel, A.S., Alameda, G.K., Behrens, R.A., and Hewett, T.A.: "Reservoir Performance Prediction Methods Based on Fractal Geostatistics," *SPE Reservoir Engineering*, 4, 311-318, 1989.

[93] Emanuel, A.S., Tang, R.W., McKay, D.M., and Ellis, M.H.: "A Hybrid Simulation Study of the Windalia Sand Waterflood," SPE paper 26477, 68th Annual Fall Technical Conference and Exhibition, Houston, TX, 1993.

[94] Emanuel, A.S. and Milliken, W.J.: "The Application of Streamtube Techniques to Full Field Waterflood Simulations," SPE paper 30758, 70th Annual Fall Technical Conference and Exhibition, Dallas, TX, 1995.

[95] Renard, G.: "A 2D Reservoir Streamtube EOR Model with Periodical Automatic Regeneration of Streamlines," *In Situ*, 14, 175-200, 1990.

[96] Hewett, T.A. and Behrens, R.A.: Scaling Laws in Reservoir Simulation and Their Use in a Hybrid Finite Difference/Streamtube Approach to Simulation the Effects of Permeability Heterogeneity, in "Reservoir Characterization, II," editors Lake, L.W. and Carroll, H.B., Jr., Academic Press, Inc., London, 402-441, 1991.

[97] Bratvedt, F., Bratvedt, K., Buchholz, C.F., Holden, L., Holden, H., and Risebro, N.H.: "A New Front-Tracking Method for Reservoir Simulation," *SPE Reservoir Engineering*, 7, 107-116, 1992.

[98] Bratvedt, F., Gimse, T., and Tegnander, C.: "Streamline Computations for Porous Media Flow Including Gravity," *Transport in Porous Media*, 25, 63-78, 1996.

[99] Peddibhotla, S., Cubillos, H., Datta-Gupta, A., and Wu, C.H.: "Rapid Simulation of Multiphase Flow Through Fine-Scale Geostatistical realizations Using a New, 3D, Streamline Model: A Field Example," SPE paper 36008, Petroleum COmputer Conference, Dallas, TX, 1996.

[100] Peddibhotla, S., Datta-Gupta, A., and Xue, G.: "Multiphase Streamline Modeling in Three Dimensions: Further Generalizations and a Field Application," SPE paper 38003, 14th Reservoir Simulation Symposium, Dallas, TX, 1997.

[101] Thiele, M.R., Blunt, M.J., and Orr, F.M.: "Modeling Flow in Heterogeneous Media Using Streamtubes — I. Miscible and Immiscible Displacements," *In Situ*, bf 19, 299-339, 1995.

[102] Thiele, M.R., Blunt, M.J., and Orr, F.M.: "Modeling Flow in Heterogeneous Media Using Streamtubes — II. Compositional Displacements," *In Situ*, bf 19, 367-391, 1995.

[103] Thiele, M.R., Batycky, R.P., Blunt, M.J., and Orr, F.M.: "Simulating Flow in Heterogeneous Media Using Streamtubes and Streamlines," *SPE Reservoir Engineering*, 10, 5-12, 1996.

[104] Blunt, M.J., Liu, K., and Thiele, M.R.: "A Generalized Streamline Method to Predict Reservoir Flow," *Petroleum Geosciences*, 2, 259-269, 1996.

[105] Batycky, R.P., Thiele, M.R., and Blunt, M.J.: "A Streamline Simulator to Model Field Scale, Three-Dimensional Flow," Proc. of the 5th European Conference on the Mathematics of Oil Recovery, Leoben, Austria, 1996.

[106] Batycky, R.P., Blunt, M.J., and Thiele, M.R.: "A 3D Field Scale Streamline Simulator With Gravity and Changing Well Conditions," SPE paper 36726, SPE Annual Technical Conference and Exhibition, Denver, CO, 1996.

[107] Batycky, R.P., Blunt, M.J., and Thiele, M.R.: "A 3D Field Scale Streamline Simulator With Gravity and Changing Well Conditions," 17th International Energy Agency Project on EOR, Sydney, Australia, 1996.

[108] Batycky, R.P., Thiele, M.R., and Blunt, M.J.: "A Streamline-Based Reservoir Simulation of the House Mountain Waterflood," Stanford Center for Reservoir Forecasting (SCRF) Annual Report, Stanford University, 1997.

[109] Sato, K. and Abbaszadeh, M.: "Tracer Flow and Pressure Performance of Reservoirs Containing Distributed Thin Bodies," *SPE Formation Evaluation*, **11**, 185-193, 1996.

[110] Pollock, D.W.: "Semianalytical Computation of Path Lines for Finite-Difference Models," *Ground Water*, **26**, 743-750, 1988.

[111] Thiele, M.R., Rao, S.E., and Blunt, M.J.: "Quantifying Uncertainty in Reservoir Performance Using Streamtubes," *Mathematical Geology*, **28**, 843-856, 1996.

[112] Ehlig-Economides, C. and Spath, J.: "Waterflood Infill Well Pattern Strategies for Horizontal and Multibranch Wells," SPE paper 35209, Permian Basin Oil Recovery Conference, Midland, TX, 1996.

[113] Christie, M.A.: "Upscaling for Reservoir Simulation," *Journal of Petroleum Technology*, **48**, 1004-1010, 1996.

[114] Barker, J.W. and Thibeau, S.: "A Critical Review of the Use of Pseudorelative Permeabilities for Upscaling," *SPE Reservoir Engineering*, **12**, 138-143, 1997.

[115] Datta-Gupta, A. and King, M.J.: "A Semianalytic Approach to Tracer Flow Modeling in Heterogeneous Permeable Media," *Advances in Water Resources*, **18**, 9-24, 1995.

[116] Martin, J.C., Woo, P.T., and Wegner, R.E.: "Failure of Stream Tube Methods To Predict Waterflood Performance of an Isolated Inverted Five-Spot at Favorable Mobility Ratios," *Journal of Petroleum Technology*, **25**, 151-153, 1973.

[117] Glimm, J., Lindquist, B., McBryan, O.A., Plohr, B., and Yaniv, S.: "Front Tracking for Petroleum Simulation," SPE paper 12238, Reservoir Simulation Symposium, San Francisco, CA, 1983.

[118] Ewing, R. E.: "Finite element techniques for convective-diffusive transport in porous media," *Advances in Water Resources*, **3**, 123-126, 1988.

[119] Rame, M. and Killough, J. E., "A New Approach to Flow Simulation in Highly Heterogeneous Porous Media," *SPE Formation Evaluation*, **7**, 247-254, 1992.

[120] Hansen, R. and Espedal, M.S.: "On the Numerical Solution of Non-Linear Reservoir Flow Models with Gravity," *International Journal for Numerical Methods in Engineering*, **38**, 2017-2032, 1995.

[121] Stalkup, F.I.: "Miscible Displacement," Monograph 8, *Soc. Pet. Eng. of AIME*, New York, 1983.

[122] Tchelepi, H.A. and Orr Jr., F.M.: Title=Interaction of Viscous Fingering, Permeability Heterogeneity, and Gravity Segregation in Three Dimensions, *SPE Reservoir Engineering*, **9**, 266-271, 1994.

[123] Burger, J.E., Bhogeswara, R., and Mohanty, K.K.: "Effect of Phase Behavior on Bypassing in Enriched Gasfloods," *SPE Reservoir Engineering*, **9**, 112-118, 1994.

[124] Burger, J.E. and Mohanty, K.K.: "Mass Transfer From Bypassed Zones During Gas Injection," *SPE Reservoir Engineering*, **12**, 124-130, 1997.

[125] Shyeh-Yung, J.J. and Stadler, M.P.: "Effect of Injectant Composition and Pressure on Displacement of Oil by Enriched Hydrocarbon Gases," *SPE Reservoir Engineering*, **10**, 109-115, 1995.

[126] Fayers, F.J. and Lee, S.T.: "Crossflow Mechanisms In Oil Displacements By Gas Drive In Heterogeneous Reservoirs," *In Situ*, **18**, 1994.

[127] Christie, M.A. and Clifford, P.J.: "A Fast Procedure for Upscaling in Compositional Simulation," SPE paper 37986, 14th Symposium on Reservoir Simulation, Dallas, TX, 1997.

[128] Barker, J.W. and Fayers, F.J.: "Transport Coefficients for Compositional Simulation with Coarse Grids in Heterogeneous Media," *SPE Advanced Technology Series*, **2**, 103-113, 1994.

[129] Stalkup, F.I.: "Effect of Gas Enrichment and Numerical Dispersion on Enriched-Gas-Drive Predictions," *SPE Reservoir Engineering*, **5**, 647-655, 1990.

[130] Johns, R.T., Fayers, F.J. and Orr, F.M., Jr.: "Effect of Gas Enrichment and Dispersion on Nearly Miscible Displacements in Condensing/Vaporizing Drives," *SPE Advanced Technology Series*, **2**, 173-180, 1994.

[131] Newley, T.M.J. and Begg, S.H.: "Characterizing the Effects of Heterogeneity on Oil Recovery by Dry Gas Injection," SPE paper 24921, ATCE of the SPE, Washington, DC, 1992.

[132] Espie, A.A., Brown, C.E., Merrill, R.C., and Newley, T.M.J.: "An Evaluation of Oil Recovery by Vaporisation," SPE paper 27812, DOE/SPE Improved Oil Recovery Symposium, Tulsa, OK, 1994.

[133] Newley, T.M.J. and Merrill R.C. Jr.: "Pseudocomponent Selection for Compositional Simulation," *Soc. Pet. Eng. Res. Eng.*, **6**, 490-496, 1991.

[134] Blunt, M.J. and Rubin, B.: "Implicit Flux Limiting Schemes for Petroleum Reservoir Simulation," *Journal of Computational Physics*, **102**, 194-210, 1992.

[135] Rubin, B. and Edwards, M.: "Extension of the TVD Midpoint Scheme to Higher-Order Accuracy in Time," SPE paper 25265, SPE Symposium on Reservoir Simulation, New Orleans, LA, 1993.

[136] van Leer, B.: "Towards the Ultimate Conservative Difference Scheme, II. Monotonicity and Conservation Combined in a Second Order Scheme," *Journal of Computational Physics*, **14**, 361-370, 1974.

[137] Dindoruk, B., Johns, R.T. and Orr, F.M., Jr.: "Analytical Solution for Four Component Gas Displacements with Volume Change on Mixing," Third European Conference on the Mathematics of Oil Recovery, Delft, The Netherlands, 1992.

[138] Peng, D.Y. and Robinson, D.B.: "A New Two-Constant Equation of State," *Ind. Eng. Chem. Fund.*, **15**, 59-64, 1976.

[139] Mehra, R.K., Heidemann, R.A., and Aziz, K.: "An Accelerated Successive Substitution Algorithm," *The Canadian Journal of Chemical Engineering*, **61**, 590-596, 1983.

[140] Peneloux, A., Rauzy, E. and Freze, R.: Title=A Consistent Correction for Redlich-Kwong-Soave Volumes, *Fluid Phase Equilibria*, **8**, 7-23, 1982.

[141] Lohrenz, J., Bray, B.C. and Clark, C.R.: "The Viscosity of Pure Substances in Dense Gaseous and Liquid Phases," *Journal of Petroleum Technology*, **16**, 1171-1176, 1964.

[142] Chang, Y.-B., Lim, M.T., Pope, G.A., and Sepehrnoori, K.: "CO_2 Flow Patterns Under Multiphase Flow: Heterogeneous Field Scale Conditions," *SPE Reservoir Engineering*, **9**, 208-216, 1994.

[143] Pande, K.K. and Orr, F.M., Jr.: "Effect of Viscous Crossflow on Miscibility Development in a Two-Layer Flow System: Part I — Ternary Condensing Gas Drives," *SPE Advanced Technology Series*, **2**, 7-17, 1994.

[144] Pande, K.K. and Orr, F.M., Jr.: "Effect of Viscous Crossflow on Miscibility Development in a Two-Layer Flow System: Part II — Ternary Vaporizing Gas Drives," *SPE Advanced Technology Series*, **2**, 7-17, 1994.

[145] "Eclipse 300 Reference Manual - 96A Release," GeoQuest Reservoir Technologies, Schlumberger GeoQuest, 5599 San Felipe, Suite 1700, Houston, TX 77056, 1996.

[146] Krechel, A. and Stueben, K.: "Operator Dependent Interpolation in Algebraic Multigrid," Proceedings of the 5th European Multigrid Conference, Stuttgart (to appear in "Lecture Notes in Computational Science and Engineering, Springer"), 1996.